University of Alberta

APPLICATION OF ULTRASOUND TO GUIDE PEDICLE SCREW INSERTION DURING SCOLIOSIS SURGERY: A FEASIBILITY STUDY

by

CHAN ZHANG

A thesis submitted to the Faculty of Graduate Studies and Research
in partial fulfillment of the requirements for the degree of

MASTER OF SCIENCE

DEPARTMENT OF RADIOLOGY AND DIAGNOSTIC IMAGING

©CHAN ZHANG
SPRING, 2011
Edmonton, Alberta

DEDICATION

To my beloved Mother, Father, Sister, and Husband,

Su-fen, Guo-ping, Nan and Jiang-qin,

for your love and support

ABSTRACT

This thesis presents an experimental study of a bovine vertebra using transmission and pulse-echo methods and a preliminary investigation to guide a screw insertion into a pedicle using TomoScan phased array unit.

The results show the cancellous bone has higher attenuation than the cortical bone for 1.0-5.0 MHz. The optimal frequencies for imaging are found to be 3.5 and 5.0 MHz. When the sample is filled with water with the cancellous core removed, all reflections from the layers and screw are visible; however when the core is present, only reflections from the top cortex are identifiable.

For the preliminary study, size and placement of the transducer array are important. When the ultrasound beam is normal to the pedicle surface, echoes from the pedicle layers and the steel bit are strong; otherwise, signals are weak and not even identifiable. Larger aperture size will enhance the signal-to-noise ratio but deteriorate lateral resolution.

ACKNOWLEDGMENTS

TABLE of CONTENTS

Chapter 1: Introduction

Chapter 2: Literature Review

Chapter 3: In-Vitro Vertebral Bone Characterization and Imaging

Chapter 4: Application of a Phased Array Technique in Vertebral Bone Imaging

Chapter 5: Conclusion

LIST OF TABLES

LIST OF FIGURES

LIST OF ABBRIVIATION

2D	Two-dimensional
3D	Three-dimensional
AGC	Adaptive gain compensation
AIS	Adolescent idiopathic scoliosis
BUA	Broadband ultrasonic attenuation
CD	Cotrel Dubousset
CT	Computed tomography
DDF	Dynamic depth focusing
FV	Forward-viewing
FWHM	Full-width-half-maximum
IS	Idiopathic scoliosis
IIS	Infantile idiopathic scoliosis
JIS	Juvenile idiopathic scoliosis
nBUA	Normalized broadband ultrasound attenuation
PA	Posterior-anterior
QUS	Quantitative ultrasound
ROI	Region of interest

SOS	The speed of sound
SRS	Scoliosis Research Society
Std	Standard deviation
SNR	Signal-to-noise-ratio
SV	Side-viewing
TGC	Time gain compensation
TOF	Time of flight
US	Ultrasound

Chapter 1

Introduction

1.1 Purpose

This thesis describes a feasibility study to investigate an innovative ultrasound imaging guidance method for pedicle screw insertion during scoliosis surgery. Based on the principle of ultrasonic pulse-echo theory, the method utilizes an ultrasound transducer to emit focused ultrasonic signals to the vertebral pedicle bone, receive reflected echoes from the boundaries of pedicle bone and the inserted screw, and finally form the bone images by giving the boundaries. The ultrasound method has the following desirable advantages: (1) radiation free, (2) real-time imaging, (3) portability, and (4) cost effectiveness.

This thesis presents the background of scoliosis and surgery, describes the acoustic properties of vertebral cortical and cancellous bones, demonstrates the in-vitro application of ultrasonic pulse-echo method to image the vertebral bone and screw, and describes the potential application and limitations of a commercial ultrasound system ― TomoScan scanner in vertebral bone imaging.

1.2 Motivation

The most effective and common method to correct severe scoliotic spine is through surgical approaches where pedicle screws are inserted into the spinal

vertebrae at multiple levels. Mechanical forces and moments are applied by orthopaedic surgeons to straighten a three-dimensional (3D) spinal deformity. The safety issue in the insertion of pedicle screws related to the closeness to the surrounding neural tissue and limited visibility of the vertebral structure during the operation, due to the small incision and continuous bleeding. Misalignment of pedicle screws with respect to the spinal cord or nerve root can result in damage of neurological tissue causing pain, loss of sensation, permanent disability, or even death if a large vascular structure is injured.

To optimize screw placement, many imaging assisted techniques have been developed. Fluoroscopy- and CT-assisted techniques have been widely used to localize pedicle screw positions for intra-operative imaging and both the applications have effectively reduced misplacement rates. However, the radiation exposure and the dose delivered to the surgeons and patients involved in this method can be significant. Other limitations of the CT-assisted technique are high cost and operating complexity. Another approach, involving a robot-assisted technique was suggested to help surgeons during pedicle screw insertion. However, the deficiencies of this system are bulky and sensitive to multiple factors including the reliability of registration algorithms, accuracy of the tracking device, and measurement noise of the navigation system and robot. Thus, better guidance alternatives should be developed for assisting screw insertion.

1.2.1 Thesis Hypothesis

Ultrasound (US) guided screw insertion into vertebral pedicles during scoliosis surgery is an alternative and safe alternative to current x-ray imaging guidance techniques.

1.3 Objectives of Thesis

The objectives of the thesis are three-fold.

(1) To apply ultrasonic immersion transmission to investigate the acoustic properties (velocity and attenuation) of vertebral cortical and cancellous bone. This requires preparing suitable animal bone models that are suitable analogues of human vertebral bone. Four pairs of single-element transducers with various frequencies (1.0 – 5.0 MHz) will be selected to study the relationship between the two acoustic parameters and frequency.

(2) To apply ultrasonic immersion pulse-echo to investigate the appropriate ultrasonic frequencies that are able to provide good penetration ability and sufficient resolution for vertebral bone/screw imaging. The ultrasound method should be applicable to the resolution requirement of guiding the screw insertion during scoliosis surgery. This will be validated by comparing the thicknesses of bone layers from ultrasound bone images with those from μ-CT bone images.

(3) To test the feasibility of the proposed ultrasound imaging method by applying the TomoScan scanner to image the vertebral pedicle bone and the inserted screw. This will require making use of the linear scanning mode to

test the effects of transducer location, active aperture, total element number
and incidence beam steering angle.

1.4 Outline of Thesis

This thesis consists of five chapters. These chapters encompass an extensive
literature review relevant to the project, experimental studies of the fundamental
acoustic properties of vertebral bone, preliminary feasibility studies of ultrasound
accuracy in vertebral bone imaging using single-element transducers, and the
applicability of ultrasound in vertebral pedicle bone imaging. Chapter 1 contains
the introduction of this work. Chapter 2 reviews literature relevant to this thesis
and highlights the need for a new image guidance method during surgery. Chapter
3 presents data on the acoustic study of vertebral bone, selection of appropriate
frequencies, and validation of the ultrasound bone imaging method. Chapter 4
discusses the applicability and limitations of vertebral pedicle bone imaging using
TomoScan scanner. Chapter 5 provides the results, the conclusions, and suggests
future work.

Chapter 2 presents a literature review of topics relevant to this thesis. An
overview of human bone and spinal structure, idiopathic scoliosis, scoliosis
surgery, and existing imaging guidance methods are presented. The human spine
is composed of a set of irregular-shaped vertebral bones that possess a cortical
outershell and a cancellous core (section 2.1). The background of idiopathic
scoliosis is described in detail, including the definition, prevalence, natural history,
and various classification and diagnosis methods (section 2.2). Both conservative

and surgical treatments are explained with their benefits and risks, especially the complications of surgical treatment (section 2.3). Various existing imaging guidance methods are presented and discussed (section 2.4). The history of the ultrasound approach is presented and the most up-to date studies of ultrasound in vertebra imaging are reviewed (section 2.5).

Chapter 3 presents the acoustic property characterization (velocity and attenuation) of vertebral cortical bone and cancellous bone and ultrasound B-mode images of vertebral bones by applying ultrasonic transmission and pulse-echo methods, respectively. The tested bone materials and the experimental set-up are described. The acoustic properties of vertebral bones, together with their response to frequency are presented and discussed. Using the knowledge of bone acoustic properties, the bone signals on the generated ultrasound bone/screw images are identified quantitatively. In addition, the measurement accuracy of the ultrasound imaging method is studied by comparing the thickness of a bone layer with μ-CT image. The effects of infilled cancellous bone between the cortical boundaries are discussed. This chapter provides the fundamental framework for ultrasound in bone imaging and sheds insight into the application of linear phased array imaging.

Chapter 4 presents the results of the bone/screw imaging using the TomoScan scanner. The chapter is comprised of: (1) validation of the locations of the transducer with respect to the vertebral bone that are able to image the pedicle bone and the inserted screw; (2) assessment of the effects of the transducer aperture on the ultrasound bone images; (3) analysis of the effects of the

5

transducer total element number on the ultrasound bone images; (4) evaluation of the ultrasound bone image response to the beam steering angle. The ultrasonic TomoScan system and the 5.0-MHz 64-element immersion linear phased array are utilized to perform the tests on a vertebral specimen of porcine spine. This chapter only presents some very preliminary results of an investigation using one bone sample.

Chapter 5 presents the conclusions as well as some perspectives of ultrasound guidance applications in scoliosis surgery.

Chapter 2

Literature Review

The chapter provides an overview of the bone and spinal structure, the background of idiopathic scoliosis which includes the definition, prevalence, natural history, various classification, and diagnosis methods. Both conservative and surgical treatments are explained with their benefits and risks, especially the complications of surgical treatment. Various existing imaging guidance methods are presented and discussed. The historical background and related work of the ultrasound approach are presented and the most up-to date studies of the ultrasound in vertebra imaging are reviewed.

2.1 Classification of Bone and Structure of Spine

Bone tissue forms the human skeleton system supporting the body and protecting the internal organs from mechanical injuries. Although bone tissue is commonly considered as hard and rigid material, it is not completely solid and contains many small spaces between the solid layers to accommodate blood vessels. Two basic types of bone are characterized: one is called cortical bone, also known as compact bone and the second is cancellous bone, also known as spongy bone or trabecular bone. These two types of bone are classified on the basis of porosity and microstructure. Cortical bone is much denser with porosity less than 30%;

while cancellous bone is much more porous with porosity ranging from 30% to 95% (Gibson and Ashby, 1999). In contrast to the structure of cortical bone, cancellous bone consists of an irregular lattice of trabeculae, forming a system of interspaces that are filled with red marrow (Tortora and Grabowski, 2003). Figure 2-1 illustrates the structure of cortical and cancellous bones.
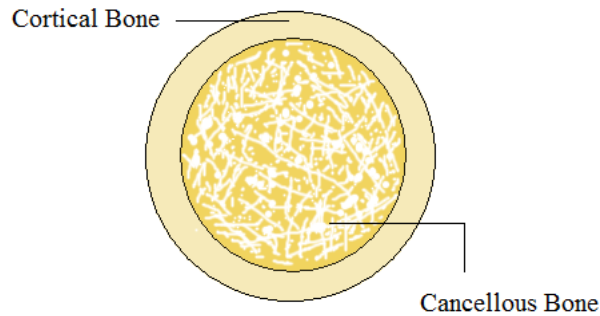
Figure 2-1: An example of cortical and cancellous bones.

Bone is classified according to shapes and sizes into long, short, flat, and irregular bones. The vertebrae make up the spinal column and fall into the group of irregular bones which contain considerable cancellous bone covered with an external layer of cortical bone (Scanlon and Sanders, 2007). The spine column is composed of 33 vertebrae stacked on top of each other, extending from the pelvis to the bottom of the skull. The spine gives body structure support, and allows a person to stand and bend with flexibility. The spine is also designed to protect the spinal cord and the major internal organs. Therefore, the health of the spine is vital to a human being. The normal spine has an S-shape from the lateral view (Figure 2-2a) and looks straight from the posterior-anterior (PA) view (Figure 2-2b). Depending on the location, the spine is divided into five regions, named from

superior to inferior as cervical (C1-C7), thoracic (T1-T12), lumbar (L1-L5), sacrum (S1-S5) and coccyx, as shown in Figure 2-2. Each vertebra is mainly composed of (1) vertebral body, (2) spinous processes, (3) transverse process, (4) pedicles, (5) foramen, and (6) lamina (Figure 2-3). The vertebral body is the main part of the vertebra. It supports about 80% of the load and provides spinal disc attachment between adjacent vertebrae. The disk serves to cushion the vertebra and allows vertebral movement. The spinous process is a bony projection perpendicular to the midline of the lamina and can be felt by hand-touching the back. Pedicles have a cylindrical shape that connect the front and back parts of the vertebra. Each vertebra has two pedicles which can provide side protections for the spinal cord. The foramens of the vertebral column are comprised of a bony tunnel where the spinal cord, containing millions of nerve fibers, passes through. The nerves carry messages from the brain to the rest of body and vice versa. Damage to the spinal cord can cause pain, loss of sensation, paralysis and even death. The lamina is the roof of the vertebral arch and provides support and protection for the backside of the spinal cord.

2.2 Background of Scoliosis

Idiopathic scoliosis (IS) is the most common structural spinal deformity, developing during childhood and adolescence. It has no known cause (Goethem and Campenhout, 2007; Haefeli and Min, 2008), and is defined as a spinal curvature of at least 10^0 Cobb angle with vertebral rotation (Cobb, 1948; Working

Group Classification, 2000). Figure 2-4 displays the normal spine compared with the scoliotic spine. The Cobb angle is the angle (Figure 2-5) between the upper vertebra most severely tilted into the curve and the lower most tilted vertebra. It is the "gold standard" to assess the severity of deformity (Cobb, 1948).

(a)   (b)
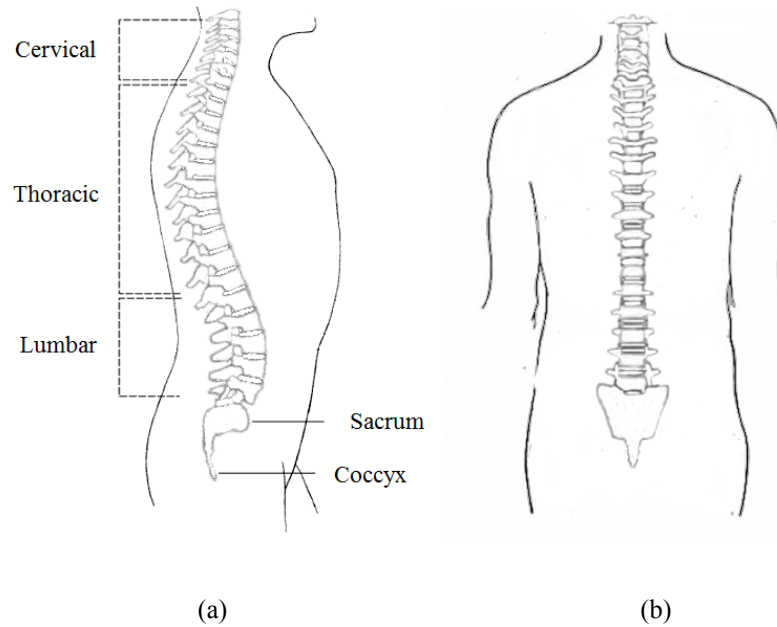
Figure 2-2: Vertebral column description: (a) lateral view, (b) posterior-anterior (PA) view.
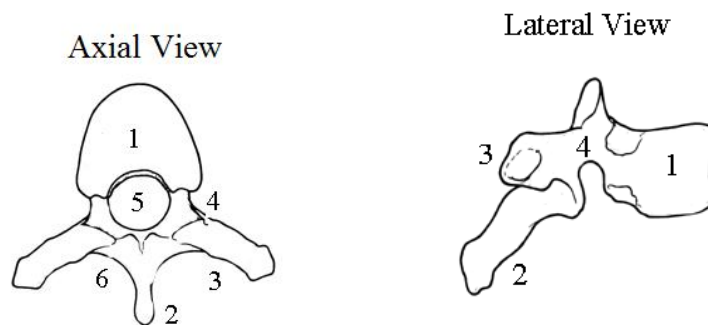
Figure 2-3: Axial and lateral views of thoracic vertebrae: 1-vertebral body, 2-spinous process, 3-transverse process, 4-pedicles, 5-foramen, and 6-lamina.

PA View   Lateral View

Figure 2-4: Scoliotic spine: PA view (Left) and lateral view (right).
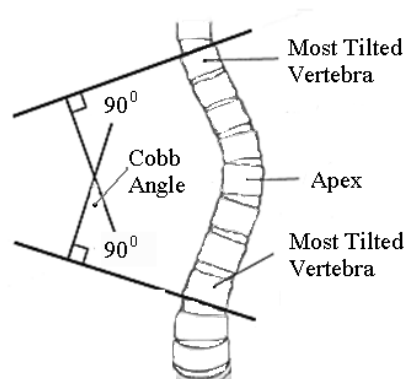
Figure 2-5: Cobb angle measurement.

Almost 80-90% of all IS cases develop during adolescence (Goethem and Campenhout, 2007; Haefeli and Min, 2008), and 2-3% of the adolescent population are affected by IS (Stirling, 1996). Scoliosis in females is more progressive than males. Approximately 5-8 times as many females as males require treatment for scoliosis. Although scoliosis has been studied for a long time, the causes of this deformity are still under investigation (Goldberg *et al*., 2008). One report suggested that an asymmetrical vertebral growth might lead to the

11

deformity (Guo *et al.* 2003)*,* and several other studies suggested that there might be a major gene controlling scoliosis (Axenovich *et al.*, 1999; Gao *et al.*, 2007). Up to now, the causes of scoliosis generally remain unknown.

2.2.1 Classification

Idiopathic scoliosis can be classified according to age of onset, or curve location, and curve type.

For age related classification, the Scoliosis Research Society (SRS) suggests classifying IS into four subcategories as infantile (0-3: IIS), juvenile (3-10; JIS), adolescent (10-18; AIS) and adult (>18 years of age).

Curve location is defined by the apex of a curve (Figure 2-5). The apical vertebra is the vertebra with the greatest distance from the midline. It typically has the most rotation and is not tilted. The SRS defines scoliosis as cervical (apex between C2-C6), cervico-thoracic (C7-T1), thoracic (T2-T11), thoraco-lumbar (T12-L1), lumbar (L2-L4) and lumbo-sacral (L5 and below).

There are also different classifications for curve type, either based on the primary and secondary curve or the severity of the curvature (Goethem and Campenhout, 2007). For example, primary curves develop at first and secondary curves may occur afterwards. The development of secondary curves appears to balance the head and upper trunk. Regarding the severity of scoliosis, mild scoliosis is defined when the Cobb angle is between 10^0 and 25^0, moderate scoliosis between $25^0 - 45^0$ and severe scoliosis when greater than 45^0.

The use of classifications is important in clinical work. The risk of progression can be estimated. Different types of treatment can be recommended against symptoms the patient will likely have. Moreover, medical doctors can communicate the condition with other health care providers. Currently, King's and Lenke's classifications of curve type are most commonly used (King *et al*., 1983; Lenke *et al*., 2001).

2.2.2 Diagnosis

Clinical assessment of spinal deformity includes the extent of rib hump, flexibility, and convexity of the curve (Goethem and Campenhout, 2007; Haefeli and Min, 2008; Goldberg *et al*., 2008). A rib hump can be observed when a patient bends forward, even for mild scoliosis. The extent of rib hump can be estimated with a scoliometer by bending forward. The flexibility and convexity of the curve will be assessed using a side bending method.

Standing PA and lateral views of whole spine radiographs are usually used to further confirm the severity of scoliosis. Cobb angle is measured on the PA radiograph. Since scoliosis is a three dimensional structural deformity, the correction and measurement of vertebral rotation has aroused interests and become important (Kuklo *et al*., 2005; Lam *et al*., 2008). Computer tomography (CT) has been proposed to perform the measurement. However, the radiation and high cost has limited its routine use. Therefore, Nash/Moe (Nash and Moe, 1969) and Perdriolle methods (Perdriolle and Vidal, 1981) remain the standard

measurements to quantify vertebral rotation.

2.3 Treatments

It is estimated that 10% of AIS cases will require specialist treatment (Lonstein, 1994). The long-term results of untreated scoliosis are still controversial, but patient with non-affected controls will have a high chance of back pain and restrictive respiratory disease in large spinal curvature (Weinstein *et al.*, 2003). Basically, the treatments are classified into two categories: conservative and surgical treatments. The most popular conservative treatment is bracing, while surgical treatment is the final option for larger progressive spinal curvature. Orthopedic surgeons determine the most effective treatment for patients based on consideration of the risk of progression, related cosmetic appearance, reduced life quality and serious pulmonary disease.

2.3.1 Brace Treatment

The objective of bracing is to stop curve progression. It is usually prescribed to AIS patients who have growth left and with moderate curves (Lonstein, 2006; Goethem and Campenhout, 2007; Maruyama and Takeshita, 2008). The highest risk of curve progression occurs during the growth spurt of adolescence. Patients have to wear brace for at least 23 hours daily and for years which highly limits their physical activities. Figure 2-6 shows a patient wearing a brace. The effectiveness of this treatment is evaluated by the final curvature compared to the

initial curve. Even though bracing has been used for 50 years, the effectiveness of bracing is still debated (Noonan *et al*., 1996; Lenssinck *et al*., 2005; Dolan *et al*., 2007). Surgical treatment will be suggested to patients if brace treatment fails.

Figure 2-6: A subject wears a custom brace for the treatment of scoliosis.

2.3.2 Surgical Treatments

Large curves will continue to worsen even after the spine growth is finished, resulting in loss of function, pain and reduced quality of life. Scoliosis surgery is the most effective method to prevent further progression of spine deformity and to diminish existing spinal deformity. The surgical rate after observation in patients with AIS is 22% compared with 23% after bracing (Dolan and Weinstein, 2007). Spinal surgery is a complicated procedure. The operation time depends on the experiences of the surgeon and the number of vertebrae involved in the surgery.

The average operation lasts for 6 hours (Karatoprak *et al*., 2008). It has risks, such as bleeding, infection and pain. The complications of this spinal surgery can be very serious. Since it is performed near the spinal cord, there is a risk of injuring the spinal cord leading to nerve damage. These kinds of damage can cause paralysis in certain areas. However, despite the complications of the surgery, long recovery time and restricted activity for 6-9 months, the immediate visual correction is persuasive. Surgeons usually discuss the pros and cons of this invasive operation with patients and their families to help them make the final decision. The surgery needs to be planned in advance and requires a team to take care of the patient.

2.3.2.1 Indications of Surgery

As indicated in 2.2.1, there are different types of scoliosis. The surgical approach may be different for each type. Fusion and fusionless surgeries are the most common types of surgery (Maruyama and Takeshita, 2008). Fusion means uniting one or more of the vertebrae together so that motion no longer occurs between them. This surgery may involve the use of metal instrumentation such as pedicle screws. Spinal instrumentation surgery without vertebra fusion is suggested for IIS and JIS so that the spine is still allowed to grow. Progressing deformity with curvature greater than 45^0 in AIS group is considered for fusion surgery even if the spine is skeletally immature.

There are three surgical approaches to instrument the spine: posterior, anterior, or combined anterior and posterior. A combined anterior and posterior approach

only happens in a very few cases.

2.3.2.2   Posterior Approach

The posterior approach is the most common method to correct deformity. Harrington introduced the first instrumentation for this type of surgery in the 1960s (Harrington, 1962). The instrumentation is designed to exert a primary corrective force on the curve by applying distraction on the concave side (using a distraction bar) and compression on the convex side of the scoliotic spine (using threaded rod with hooks). The focus of the Harrington method is for two dimensional corrections. A report from Niemeyer *et al*. (2005) based on a long term follow up of patients who had Harrington operations found a high degree of satisfaction with the quality of life (Niemeyer *et al*., 2005). In 1980s, a better metal implant system called Cotrel Dubousset (CD system) was developed which allowed for segmental instrumentation. The focus of the CD system is for three-dimensional correction. The instrumentation system of the CD system was more frequently used and allowed for more correction of lower lumbar segment motion than the Harrington method (Lenke *et al*., 1993). Initially, the correction and instrumentation was performed using hooks and rods. Later pedicle screws were introduced and combined with hooks and rods by Roy-Camille in the late 1970s to study the stabilization of lumbar spine (Roy-Camille *et al*., 1986). Recently, more clinical studies use pedicle screws and show better correction (70-72%) than the hook instrumentation (42-60%) (Barr *et al*., 1997; Liljenqvist *et al*., 1997; Kim *et al*., 2005). Figure 2-7 displays the radiographic reviews of patients after posterior

17

surgery with the pedicle screws only.

(a)   (b)
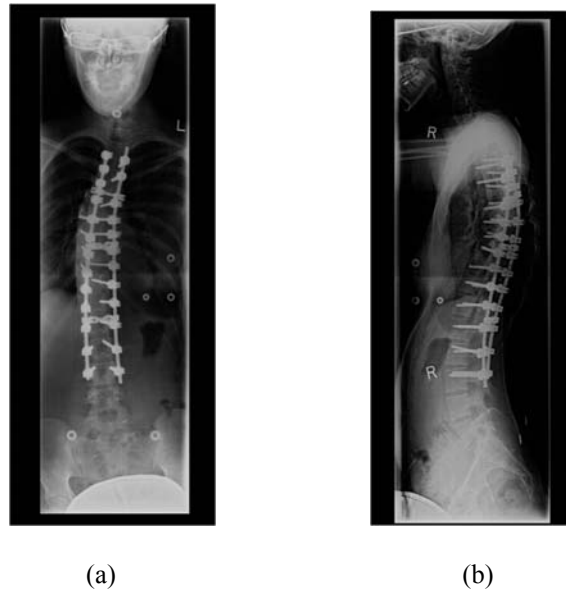
Figure 2-7: Radiographs of patient after posterior spinal surgery: (a) poster-anterior view, and (b) lateral View.

2.3.2.3   Anterior Approach

Anterior spinal instrumentation is a technique primarily used for thoracolumbar and lumbar scoliosis correction. It involves insertion of vertebral screws from the anterior of the spine into the vertebral body, with a rod applied to connect to the screws placed at the different spinal levels. Zielke and Berthet (1978) reported this technique required shorter fusion lengths compared to posterior procedures. However, the possibility of disrupting the chest cage during surgery may affect the pulmonary function of patients, whereas posterior instrumentation surgery can correct curvature without this unpleasant affection (Kim *et al.*, 2005). Besides, better curve corrections (62-69%) were reported with posterior than anterior surgery (52-56%) (Asher *et al.*, 2004; Potter *et al.*, 2005; Suk *et al.*, 2005; Newton

et al., 2008). However, the superiority of anterior surgery has been lost due to unsatisfactory postoperative pain and operative scar (Maruyama and Takeshita, 2008).

2.3.2.4   Complications of Surgery

Current research focuses on posterior spinal fusion surgery using pedicle screws. During surgery, a pedicle screw will be inserted through the pedicle into the vertebral body. Figure 2-8 (a) and (b) show the ideal insertion of a pedicle screw and an example of pedicle misplacement, respectively. The width of pedicles varies for different vertebrae. For Thoracic spine, the average pedicle width ranges from 4.5 to 9.8 mm (Vaccaro *et al*., 1995; Laporte *et al*., 2000). The available dimensions of pedicle screws range from 3.5 to 6.5 mm and Figure 2-9 shows a photo of a pedicle screw. To achieve the best curvature correction effects, pedicle screws should be inserted into the center of the pedicles as precisely as possible (Geerling *et al*., 2007). Usually, the margin between the pedicle screw and pedicle outer boundaries is approximately 1-2 mm. Due to the closeness to the surrounding neural tissue and limited visibility of the vertebral structure during the operation because of the small incision and continuous bleeding, the safety issue in the insertion of pedicle screws is a concern. Misalignment of pedicle screws into the spinal cord or nerve root can result in local tissue damage or permanent disability, or potentially even death ($\leq$1%) if a large vascular structure is injured (Bradford *et al.*, 1999). Therefore, a miniature cannulation probe is regularly used to advance free hand through the pedicle into the vertebral

body to create guiding holes for screw insertion. However, multiple holes might be created to check all the boney borders of pedicles which replace the intrapedicular cancellous bone (Kim *et al.*, 2004) and hence reduce the strength of the screw fixation with bone. Nevertheless, the misplacement of the screw can still occur even with guiding holes and the penetration rate into the thoracic levels has been reported ranging from 6.2% to 54.7% (Vaccaro *et al.*, 1995; Liljenqvist *et al.*, 1997; Xu *et al.*, 1998; Belmont *et al.*, 2001; Kim *et al.*, 2004).

(a)   (b)
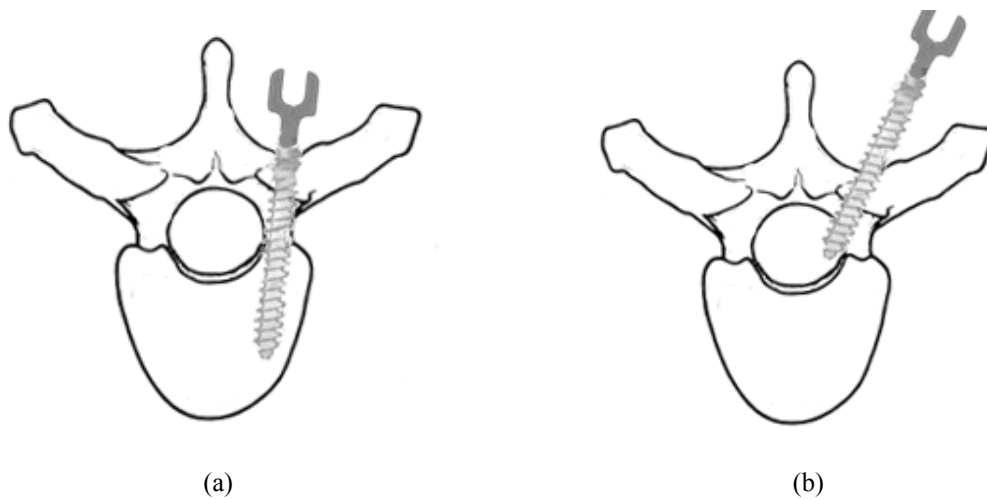
Figure 2-8: Illustration of pedicle screw insertion into vertebral bone: (a) Ideal insertion into the vertebra body without any pedicle perforation, and (b) one example of screw malposition (medial penetration).
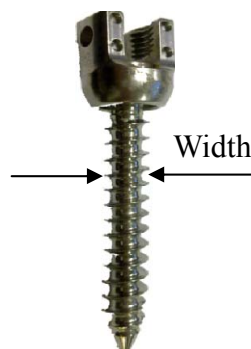
Width

Figure 2-9: A photo of a 6.5 mm (width) pedicle screw.

2.4 Existing Imaging Guidance Techniques

To optimize the placement and confirm the screw position, various imaging assisted navigation systems using fluoroscopy, CT, robot and ultrasound techniques have been developed or proposed to guide screw insertion.

2.4.1 Fluoroscopy Technique

Fluoroscopy-assisted techniques have been widely used to localize pedicle screw positions for intra-operative imaging because of real time imaging and are commonly used by physicians. However, the disadvantage of fluoroscopy is the radiation exposure to both the surgeon and patient in the operating room.

Foley *et al*. (2001) proposed a virtual fluoroscopy technology. This system combined a C-arm fluoroscopy and a computer navigation system. Posterior-anterior and lateral views of the vertebrae are taken with a fluoroscope. With small rotation of the fluoroscope, it is possible to obtain different views of the vertebra. The images are then transferred from the fluoroscope into the library of a navigation system. A position sensor attached to an insertion tool is captured by an optical tracking system to measure its relative position to the vertebra. This technique can provide surgeons with continuous updated fluoroscopic images. By taking two or more calibrated fluoroscopic images from various views and tracking their spatial location using an optical tracking system, the surgical tool is overlaid onto these images in real time. Thus, the surgeons can manipulate the tracking insertion tool and view an updated image of the position of the screw

relative to the vertebra.

This virtual fluoroscopy had several advantages over traditional fluoroscopy, such as multi-planar guidance and less radiation exposure. Mirza *et al*. (2003) compared these techniques and reported the misplacement rate and radiation to the surgeon's hand of virtual fluoroscopy were 14% and 0.31±0.38 mSv/procedure respectively, compared with 26% and 3.1±2.27 mSv/procedure of conventional fluoroscopy. Choi *et al*. (2000) performed experiments on cadaver specimens using this virtual fluoroscopy technique and reported 17.9% misplacement. However, this technique still has radiation exposure and the dose delivered to surgeons was up to 231.7±48.2 mSv/specimen compared with 12.1±2.0 mSv/specimen for standard fluoroscopy (Mirza *et al*., 2003).

A three-dimensional (3D) fluoroscopy assisted device (Iso-D-3D, Siemens, Germany) was developed to provide intro-operative 3D images for surgical navigation. The images were constructed by obtaining multiple images during an automatically guided rotation around the patient. Holly and Foley (2003) performed the evaluation of this device in their laboratory using three cadaveric specimens. A total of 102 pedicle screws were inserted into 30 lumbar vertebrae and 72 thoracic. Only 5.4% misplacement was observed. Hott *et al*. (2004) then evaluated the system clinically in 86 placements from cervical to lumbar vertebrae. There was 4% misplacement at the cervical vertebrae, 6% in thoracic and none in lumbar vertebrae. Ito *et al*. (2008) recently performed a clinical study using this 3D system. They inserted a total of 176 cervical pedicle screws into 50 cases.

Only 2.8% misplacement rate was found. The small misplacement rate of pedicle screw suggested this new technology has great potential in spinal surgery.

2.4.2 CT Technique

Amiot *et al.* (1995) described the application of the CT-assisted technique in spinal surgery. A 3D model of the vertebrae specimen was acquired by using a CT scan. This 3D model would be displayed on a computer workstation with visualization in axial, sagittal, and coronal planes. A position sensor attached to a pointing tool was used to point on the vertebra and register the contour of the vertebra. Registration methods were utilized to match the patient's anatomy and pre-acquired CT data. The advantages of the CT-assisted technique is the three dimensional visualization of the pedicles. This allows precise observation of their positions relative to the anatomic structures and a preoperative planning of the pedicle screw insertion. Several studies reported the misplacement rate using a CT-assisted technique was 4.5-10% (Merloz *et al.*, 1998; Laine *et al.*, 2000; Arand *et al.*, 2001).

However, the disadvantage of this approach is the pre-operative CT scan. Furthermore, the lying position may reduce the Cobb angle and affect the vertebral rotation. Vertebral position and orientation may be slightly different when the patient is at different lying postures. Errors may exist between the pre-scanned CT images and the real vertebra during the operation. Furthermore, the registration methods might not be accurate due to artefacts, leading to wrong

positioning of pedicle screws. The other limitations of this CT-assisted technique are the high cost and radiation dose.

2.4.3 Robot Technique

A robot-assisted method was proposed to help surgeons during pedicle screw insertion by Ortmaier *et al*. (2006). The system was composed of a robotic arm, a linear guide with marker arrays, and a navigation system (VectorVision from BrainLAB). The robot is connected to the navigation system via TCP/IP. The navigation system has a graphic user interface and an optical tracking system. With the tracking system and the marker arrays on a linear guide, the position and orientation of the linear guide can be calculated and related to the drill axis of the pre-acquired vertebral model. The position data are sent to the robot continuously. The linear guide is driven to drill the hole by the robot and held by an operator. A precise guidance of insertion can be achieved. At the same time, the operator can receive full haptic feedback during the insertion.

Experiments on both artificial bone (SawBone) and a 9-week bovine spine (similar structure with real human spine) were studied to investigate the position accuracies of the robot-assisted method during the spinal surgery. After identifying the optimal machining parameters such as speed and force by the artificial model experiments; best performance parameters were applied to the bovine bone to study position accuracy. Two criteria were defined to evaluate the accuracy of the system. One was position error which was the distance between

real entry point of the screw and its ideal entry point on the vertebra; another criterion was orientation error, which represented the angle between the real and ideal drill axis. The results indicated the average position error was 0.6 mm and the maximum position error was 2.6 mm. The maximum orientation error was 0.5 degree. Although the error results indicate this robot assisted technique might provide guidance for the pedicle insertion, the accuracy of this system depends on the following factors: (1) bone registration with preoperative CT, (2) the accuracy of the tracking system, (3) spatial resolution of preoperative imaging, (4) segmentation accuracy, and (5) measurement noise of the navigation system and robot. These factors may limit its application.

2.4.4 Ultrasound Technique

2.4.4.1   Background and Related Work

Ultrasound (US) is mechanical waves propagating through a medium with frequency over 20 KHz. The ultrasound wavelength is inversely proportional to its frequency. The spatial resolution is determined by the wavelength of a pulse. The resolution and the penetration ability of ultrasonic beam have a trade-off relationship, which indicates the higher the frequency used, the greater the spatial resolution but the shallower the depth of tissue that can be reached. The propagation of ultrasonic waves depends on the acoustic properties of the medium, such as density, elasticity and acoustic impedance. An interface is presented between two media with different acoustic impedances causing ultrasonic

reflection and refraction: a portion of incident ultrasonic energy is reflected from the interface (pulse-echo) and portion of energy transmit further (transmission). These reflected and transmitted waves carry the information of the medium. By measuring the amplitude, travel time, frequency and phase changes of these waves, the properties of the medium can be determined. The principle of ultrasonic reflection forms the basis of modern medical ultrasonic imaging and contributes to the image formation by providing the boundaries of organs (Njeh *et al.*, 1999).

With specific targeting and navigation ability, ultrasound technology has rapidly evolved and is widely used in soft tissue imaging for diagnosis, therapeutic and interventional guiding purposes. However, the potential of ultrasound has not been fully exploited and has long been ignored in the field of bone characterization and imaging due to the complex hierarchical structure and complicated interaction of bone with ultrasonic wave (Laugier *et al.*, 2008). Nevertheless, there are two ultrasonic variables related to bone quality: the speed of sound (SOS) and broadband ultrasonic attenuation (BUA) (Cobbold, 2008). The transmission method and pulse echo method are the most popular techniques to characterize and image bones. Langton *et al.* (1984) first utilized the immersion ultrasonic transmission method to measure the BUA of human heels to evaluate bone quality and showed that healthy females had higher BUA values than osteoporotic females. Following Langton's work, intensive studies have been conducted to investigate the efficacy of ultrasound by comparison with ionizing radiation techniques; it has been demonstrated that quantitative ultrasound (QUS)

predicts risk of future fracture as well as DXA (Bauer *et al.*, 1997; Hans *et al.*, 1993, 1995; Njeh *et al.*, 1997). Meanwhile, attention has also been given to ultrasonic bone imaging. In 1994, Laugier *et al.* first obtained BUA images of Os Calcis. The reproducibility of the BUA imaging method and the feasibility in osteoporosis diagnosis were later demonstrated by Roux *et al.* (1996). The group of Lasaygues has since 1997 dedicated efforts to construct cross sectional images of cylindrical bone using ultrasonic reflection and transmission tomography methods. They have so far successfully derived the speed of sound to construct images of cortical bone (Ouedraogo *et al.*, 2002) and human femur (Lasaygues *et al.*, 2005), and assessed the cortical thickness of long bone (Lasaygues *et al.*, 2006). Zheng *et al.* (2009) confirmed the potential of ultrasound to reconstruct the long bone's internal structure using contact pulse-echo technique and addressed the accuracy of ultrasound imaging by comparing with CT image. These studies suggest that ultrasound might offer a radiation-free alternative method to assist orthopedic surgeons to perform surgical procedures in real-time.

2.4.4.2 Overview of the Recent Studies in Vertebra Bone Imaging

Up to now, there are a limited number of studies about ultrasound guidance methods during spinal surgery. A system using ultrasound-assisted intra-operative navigation was proposed in spinal surgery by Weber *et al*. (2001). The system was composed of an intra-operative ultrasound machine and a robot system. An ultrasound probe was implemented to scan the vertebra intra-operatively. Real time ultrasound images of the vertebra were acquired. Then registration was

applied to match the ultrasonic vertebral contours with preoperative CT images. An operator-held robot was used to insert pedicle screws under the guidance of matched images. In-vitro experiments were performed in water on a pig lumbar vertebra sample and a phantom to study image resolution and precision of the robot using a 3.5-MHz linear array transducer. The resolution of the US system was 1.5 mm for the bone sample. The preliminary experiments indicated this system had potential to be used in spinal surgery. However, the accuracy of this system was governed by the following: (1) the resolution of the imaging modality, (2) sensitivity to image artifacts, (3) the accuracy of the registration method, and (4) the accuracy of the positioning the robot before operation. Surgeons need to be familiar with all the procedures before they use the system. The complexity of the system and additional CT radiation to the patients may limit its future application in clinical use.

Barratt *et al.*, (2006) reported a freehand 3D ultrasound method combined with CT and tracking equipment. Their system was similar to Weber. To increase the registration accuracy, they developed a self-calibrating approach. Experiments were performed on 6 femurs and 3 pelvises of human cadavers. The average registration error was 1.5 mm compared to the standard registration methods (0.5-5 mm). Winter *et al.* (2008) also used a similar system and applied various registration algorithms to the CT/Ultrasound combination system. They found that a covariance matrix adaption evolution algorithm had the best performance and the correct registration rate was 99.96%. These studies focused on developing and

improving registration algorithms to increase accuracy. Their studies demonstrated the potential application of this type of system during spinal surgery. However, the whole system is bulky and the operation procedure is complicated.

Mujagic *et al*. (2008) proposed a new concept of an intra-operative ultrasound imaging guidance system. They performed an experimental study to quantify the acoustic properties of human vertebral cancellous bone and explored the feasibility of using ultrasound for A-mode bone imaging. They used ultrasound pulse echo technique to determine the thickness of cancellous bone. Because of different acoustic impedances between different interfaces of bone and water, different amplitudes and arrival times were recorded. An A-mode image of vertebral cancellous bone was generated according to the characterized acoustic velocities. Two transducers with 1.0 MHz and 3.5 MHz were used in the experiments. An aluminum block was used as a reflector to help identify the interfaces between bone and water. The distance between cancellous bone and the block was set to 35 mm to ensure there would be no interference between the echoes. The thickness error related to the actual sample thickness was about 0.9 mm and 1.1 mm for 3.5 MHz and 1.0 MHz transducers, respectively. This preliminary ultrasound study proved the boundary of cancellous bone could be imaged. Higher frequency could improve image resolution, but the penetration depth was then limited. Therefore, the choice of frequency in ultrasound imaging should be considered based on the trade-off between resolution and penetration depth. They also reported that thicknesses of cancellous bone samples used in this

study (10-19 mm) were larger than the pedicle width (4.5-9.8 mm), and the cortical layers were ignored.

A novel technique called Intraosseous Ultrasonography (IOUS) was applied to determine the accuracy of pedicle screw placement (Kantelhardt *et al.*, 2009). The system was comprised of an In-Vision Gold Intravascular Ultrasound system with an Eagle Eye Gold Single-use Intravascular Ultrasound Imaging Catheter (Volcano Therapeutics Inc., Rancho Cordova, CA). The center frequency and the diameter of the catheter were 20 MHz and 1.2 mm, respectively. In-vitro experiments were performed on 2 human lumbar spine specimens and 24 pedicle screw holes were produced. Each pedicle was examined with IOUS by inserting the catheter to the end of each hole and then retracting slowly. Real time US images of the hole can be acquired. The postoperative CT scans were used to investigate the position of each of the holes. The CT results indicated the screw holes were placed correctly in 15 cases, but 5 medial and 3 lateral perforations occurred. One case appeared to be traversed fracture lines within the vertebral body. About 99% of the US images of these holes were interpreted correctly compared with CT results, except for the traversed case. Intra-operative evaluations were performed on 3 patients and there were 20 lumbar pedicles in total. The CT results indicated no perforation, and IOUS examination showed 100% correct interpretations. Most recently, Raphael *et al.* (2010) utilized A-mode ultrasound to study the association of ultrasound echoes with the position of the transducer through the pedicle and ultimately towards the distal ventral cortex and

complications like the perforations of distal ventral cortex and inner pedicle wall. In-vitro ultrasonic immersion experiments on ten bovine vertebral bodies were performed by using two 2.5-MHz single-element focused immersion transducers. These two transducers were designed with a forward-viewing (FV) and a side-viewing (SV) face to obtain the forward and side-viewing A-mode ultrasound reflection signals from bones. The FV transducer was first advanced into each vertebral body with a flat-bottom drill in successive 5-mm increments and the SV transducer was inserted into the drilling pathway immediately after each measurement made by the FV transducer. After the final measurement, deliberate distal ventral cortex perforations and a complete perforation of an inner pedicle wall were made individually at six samples to test the relationship between echo signal and complications using the FV transducer. The evident A-mode patterns of the measured echoes at each point indicated that (1) the peak amplitude of the last three echoes in the FV profile kept increasing when the FV transducer approached the ventral cortex layer; (2) the peak amplitude could reach maximum in the SV profile when the SV transducer was close to the pedicle wall. Furthermore, a significant drop in the amplitudes of echoes indicated a cortex perforation. These two studies have demonstrated the possible application of ultrasound method in screw fixation surgery.

2.4.5 Conclusion

To decrease these complications, various imaging guidance methods have been developed. The principles of these existing imaging guidance methods for surgery

were reviewed. Although fluoroscopy- and CT-assisted methods have been found to reduce pedicle violations, the ionizing radiation involved in these two methods might limit their popularity. CT or Robot systems are complex and sensitive to difficulties in registration, tracking and software instability. Ultrasound techniques have been suggested for scoliosis surgery. Currently, there are no US systems that can guide screw insertion in real-time. Orthopaedic surgeons still rely on their experience and tactile sense to insert pedicle screws. Better guidance methods should be developed to help screw insertion during surgery.

Chapter 3

In-Vitro Vertebral Bone Characterization and Imaging[§]

In this chapter, we first consider the problem of quantifying the acoustic properties (velocity and attenuation) of vertebral cortical and cancellous bones and find the appropriate frequencies to resolve the echoes from closely-spaced bone layers. A piece of bovine vertebral cortical bone and a cancellous bone were prepared and tested in water by using an ultrasound transmission method. Four identical pairs of immersion unfocused transducers of frequencies 1.0, 2.25, 3.5, 5.0 MHz were utilized to measure their acoustic properties. Secondly, we applied immersion focused transducers with pre-determined ultrasonic frequencies to scan two bovine vertebral specimens with and without screw inserted into the cores to investigate the feasibility and limitations in vertebral bone imaging. To verify the effects of cancellous bone, one of the two vertebral samples had the cancellous core removed. Ultrasound pulse-echo method was employed. Ultrasound B-mode bone images of vertebral bone samples prior to and after the screw insertion were produced for identifying reflections from the bone/screw interfaces with pre-

---

[§] Parts of this chapter have been published. Lou, E., Zhang, C., Le, L. H., Hill, D. L., Raso, J. V., Moreau, M. J., Mahood, J. K., and Hedden, D. M. (2010). "Using ultrasound to guide the insertion of pedicle screws during scoliosis surgery," Research into Spinal Deformities 7, Studies in Health Technology and Informatics (IOS press, USA), pp. 44-48. Le, L. H., Zhang, C., and Lou, E. (2010). "Resolution Study of Ultrasound Reflections in Bovine Vertebral Bone *In-Vitro*," *3rd international conference on the Development of Biomedical Engineering. Proceedings. Vietnam*, pp.129-132.

characterized acoustic properties. The accuracy of ultrasound imaging was evaluated by comparing the bone layer thicknesses with corresponding μ-CT images.

3.1 Acoustic Properties Measurement

The speed of sound (SOS) and broadband ultrasonic attenuation (BUA) are two ultrasonic variables related to bone quality (Cobbold, 2008) and have been applied clinically to assess mechanical and structural properties of bone (Laugier, 2008). There are three main methods to measure these two variables of bone at different locations (Njeh *et al.*, 1999): (1) contact method: the transducers are in contact with the sample; (2) immersion transmission method: one transducer acts as a transmitter and another as a receiver; the sample is positioned between the transducers and the experimental setup is immersed in water; (3) axial method: the transmitter and receiver transducers are put in contact with the bone on the same side. In this study, we applied the immersion transmission method to characterize the vertebral cortical and cancellous bones.

3.1.1 Velocity

Measurement of ultrasonic velocity includes group velocity (velocity of the center of a pulse) and phase velocity (velocity of each frequency component composed of the ultrasonic pulses). The group velocity is measured in the time domain by measuring the time differences between the input reference signal and transmitted signal through the sample at several reference points. However, the time method

may be unreliable due to pulse shape changes caused by frequency-dependant attenuation. Therefore, phase spectrum analysis has been suggested to examine the phase velocities (Sachse and Pao, 1977).

3.1.1.1 Time-Domain Method

For the time transmission technique, two signals are recorded without and with the sample in the beam path. The former is a reference signal through water (water pulse) and the latter is a sample pulse. The propagating group velocity v_{bone} was simply measured by the substitution method (Rossman *et al.*, 1989):

$$v_{bone} = \frac{L}{L/c_{water} - \Delta t} \tag{3-1}$$

where Δt is the time difference between the reference points of the sample pulse and the water pulse, L is the thickness of the bone sample. Several reference points were used for comparison: first motion (first detectable deviation from zero), first-zero crossing, and signal envelope.

3.1.1.2 Phase Spectrum Method

For the transmission technique, phase velocities c_{bone} were calculated by the phase spectral method (Sachse and Pao, 1977):

$$c_{bone}(\omega) = \frac{\omega L}{\omega L/c_{water} - \Delta\varphi(\omega)} \tag{3-2}$$

where ω is angular frequency, L thickness of the foam, c_{water} acoustic wave speed in water (1480 m/s) and $\Delta\varphi(\omega)$ is the unwrapped phase difference between the

water reference pulse and the sample pulse. To improve the accuracy of phase velocity estimation, we followed Verhoef *et al.* (1985) to determine $\varphi(0)$, the phase at zero frequency, which was defined as the multiple of 2π nearest to the zero crossing of the fitted line with the coordinate and minus the amount from the unwrapped phase difference $\Delta\varphi(\omega)$. The phase velocities are then calculated by substituting the adjusted difference $\Delta\varphi^*(\omega)$ into equation (3-2), which is given by:

$$\Delta\varphi^*(\omega) = \Delta\varphi(\omega) - \varphi(0) \tag{3-3}$$

3.1.2 Attenuation

Total ultrasonic energy loss due to scattering, absorption, and transmission is quantified by the attenuation coefficient (α_{total} in dB/cm):

$$\alpha_{total}(\omega)(\text{dB/cm}) = 20 \times \frac{1}{L} \log_{10} \frac{R(\omega)}{S(\omega)} \tag{3-4}$$

where $R(w)$ and $S(w)$ are the amplitude spectra of the water pulse and the specimen and L is the thickness of the sample. The attenuation defined by equation (3-4) includes the energy loss due to the bone/water interfaces. The attenuation with the transmission effect removed is

$$\alpha_{corrected}(\text{dB/cm}) = \alpha_{total} + 20 \times \frac{1}{L} \log_{10}(T_1 T_2) \tag{3-5}$$

and

$$T_1 T_2 = \frac{4 z_1 z_2}{(z_1 + z_2)^2} = \frac{4 \rho_{water} c_{water} \rho_{bone} c_{bone}}{(\rho_{water} c_{water} + \rho_{bone} c_{bone})^2}, \tag{3-6}$$

where T_i are the transmission coefficients, z_i the acoustic impedances and ρ_{water}

and ρ_{bone} are the densities of water (1000 Kg/m^3) and bone sample.

The normalized broadband ultrasound attenuation (nBUA) in dB/MHz/cm was obtained by normalizing the attenuation within the relevant frequency band.

3.2 Study Design

Two experimental sets (I and II) were designed in this chapter for purposes of bone characterization and vertebral bone imaging, respectively. Section 3.2.1 introduces experimental set I including the preparation of vertebral cortical and cancellous bones, and the immersion transmission experimental setup for their acoustic properties measurement. Section 3.2.2 presents the two vertebral specimens, pedicle screw and the immersion pulse-echo experimental setup involved in Experimental set II.

3.2.1 Experimental Set I: Bone Characterization

3.2.1.1 Spine Specimens

Two spinous processes obtained from a bovine cervical segment were used in this study. All attached soft tissues including muscle, tendon, ligament, and connecting tissue were removed from the sample. The processes were then individually cut into smaller pieces. A piece of cortical plate was dissected from the specimen along the cortical-cancellous interface using a sagittal saw (Sample 2), as Figure 3-1 (a) and (b) show. Its dimension was measured with a ruler as 25

mm × 29 mm and the thickness within the scanning region was 2.33 ± 0.13 mm which was measured by a caliper. Cancellous bone was exposed by grinding off the cortex outershell of another sample using a belt and disc sander, as displayed in Figure 3-1 (c) and (d). It had dimensions of 25 mm × 12 mm. The thickness was measured as 4.64 ± 0.22 mm. Since the spaces between the trabeculae of the cancellous bone were filled with red marrow, the cancellous bone sample was defatted using a water jet. Before the experiments, the cancellous bone sample was immersed in water to ensure its pores were fully saturated with water and all air bubbles eliminated. A few drops of detergent were added to the water to reduce the surface tension of water.
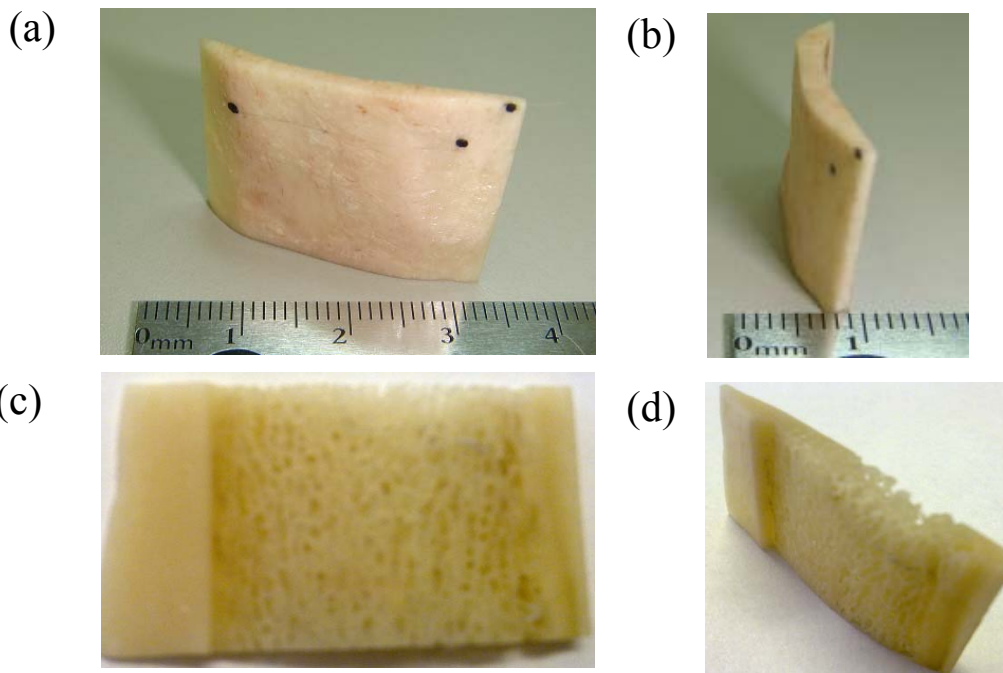
Figure 3-1: Bovine cortical and cancellous specimens: (a) and (b) The front view and lateral view of the cortical bone, respectively, (c) and (d) the front view and lateral view of the cancellous bone.

3.2.1.2   Experimental Set-Up

Figure 3-2 shows the ultrasonic immersion experimental setup using a pulse transmission technique to measure the velocity and attenuation of bone samples. A pair of identical transducers was coaxially mounted on the holder with the bone samples placed between the two transducers: one to act as a source and the other to act as a receiver. The distance d between the transducers was set to approximately 54.6 mm. A Panametrics broadband pulse/receiver 5800PR unit (Panametrics-NDT, Waltham, MA) was used to excite the source transducer. The transmitted bone signal and water reference signal were recorded with and without bone sample interposed between the transducers. The signals were then digitized to 8 bits by a LeCroy wavesurfer 422 oscilloscope (LeCroy, Chestnut Ridge, NY). Each signal was averaged over 256 times to increase the signal-to-noise-ratio and decimated with a time interval of 0.02 μs for off-line spectrum analysis with zero-padding. The whole setup was immersed in water. All the measurements were made in water at room temperature. According to the relationship of the temperature-dependent speed of sound in water with temperature (Kaye and Laby, 1973):

$$V_{water} = 1402.9 + 4.835T - 0.047016T^2 + 0.00012725T^3 \qquad (3\text{-}7)$$

where T is the temperature in Celsius. Since the temperature of the water was approximately 19.5^{o}C, V_{water} was 1480 m/s.

Four identical pairs of non-focused 12.7-mm-diameter transducers: 1.0, 2.25, 3.5, and 5.0 MHz (V303, C306, C382, and C309 respectively, Panametrics-NDT, Waltham, MA) were used. Six measurements were made for each frequency by translating the sample with a step size of 1 mm parallel to the transducers' faces

(Z-direction) while keeping the main beam of the ultrasound wave within the boundaries of samples.
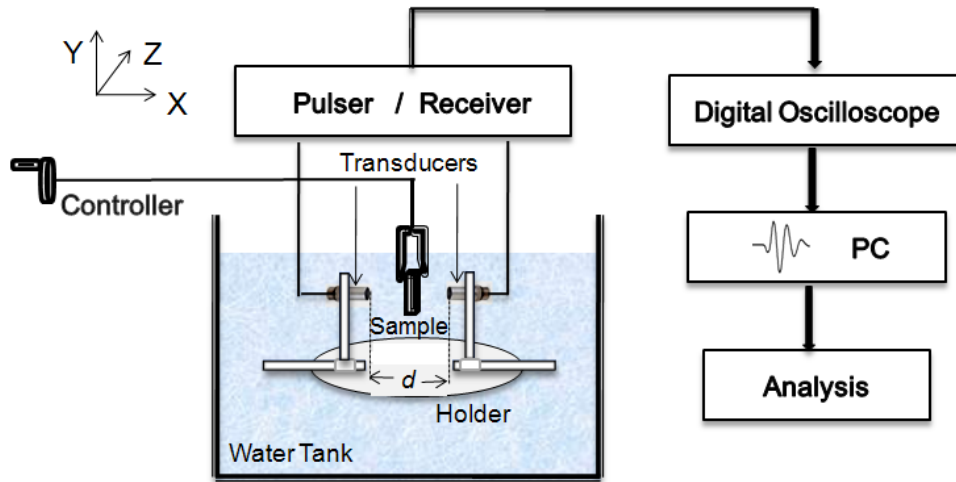
Figure 3-2: Setup for the transmission experiment to characterize bone sample.

3.2.2 Experimental Set II: Vertebral Bone Imaging

3.2.2.1 Spine Specimens and Pedicle Screw

As with previous bone preparation procedures discussed in Section 3.2.1.1, two additional spinous processes were also obtained from the bovine cervical segment. All attached soft tissues including muscle, tendon, ligament, and connecting tissue were removed from the samples. The processes consisted of two cortex plates and a cancellous core. One of the process samples was randomly selected and the inside cancellous core was scratched off with the assistance of a surgical curette and labeled as #1. Figure 3-3 (a) and (b) display the #1 bone sample and its cross section. The sample with the cancellous core was labeled as #2 and was defatted. Figure 3-3 (c) and (d) present the #2 bone sample and its cross section. For both

the samples, the core thickness varied from 5 mm to 7 mm along the y-direction and the thickness of cortical layers was about 3 mm. These two samples had a larger dimension (38 mm × 30 mm) than the vertebral pedicle bone but the maximum thickness of core layers were similar to that of the pedicle. These two samples were scanned with and without a titanium-alloyed pedicle screw (Figure 3-4) fixed in position. The dimension of the screw was 6.5 mm (W) × 45 mm (L). For the vertebral sample #2 (containing the cancellous bone), the drill was advanced to perforate the core immediately after the measurement without the screw. The screw was then advanced into the cavity to a certain depth after positioning the perforated vertebral sample on the set-up. All samples were well preserved in methanol solution. The degassing procedures were same as introduced in Section3.2.1.1.

3.2.2.2   Experimental Set-Up

A transducer holder was custom designed to hold transducers in position and control the movements in 3 dimensions (front/back, up/down, and left/right directions). Figure 3-5 shows the experimental setup. The bone sample was positioned on a holder and the bone face was parallel to the transducer surface initially in a normal incidence configuration to ensure maximum penetration of the ultrasonic beam into the bone layers. The screw was fixed on one arm of the device and adjusted to be inserted into the bone samples. A focused immersion transducer with an active diameter of 6.4 mm was used as both a source and receiver. Two frequencies were considered for the process sample without cancellous core based on the experimental observations of experimental set I: 3.5

41
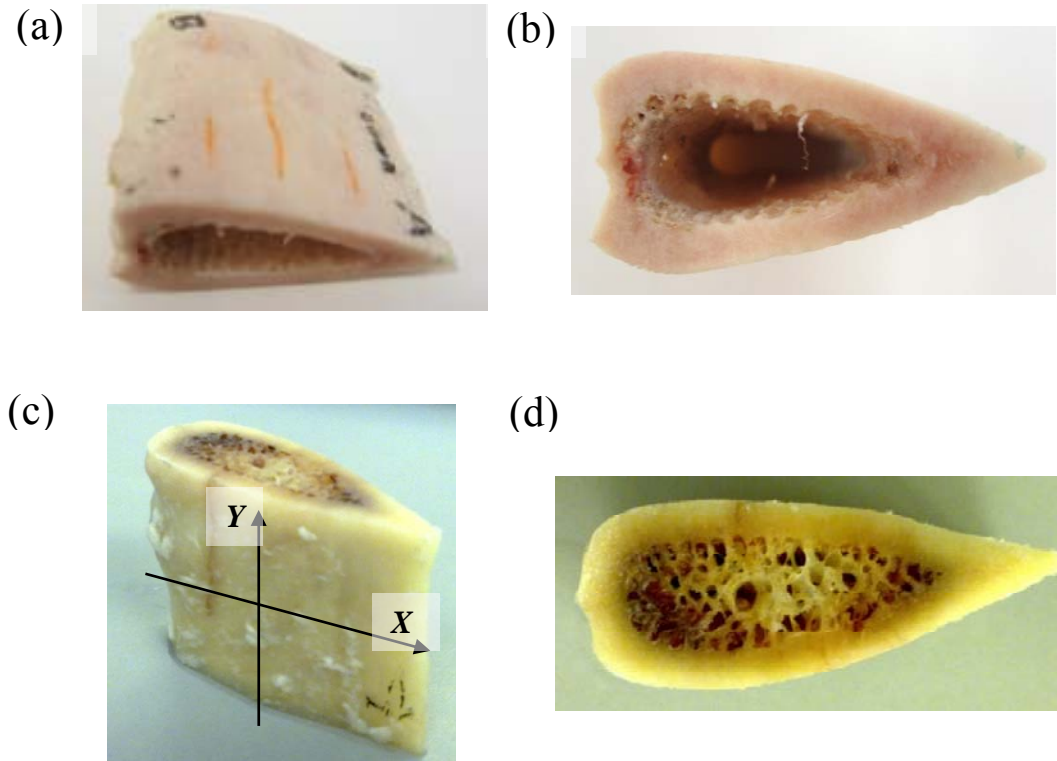
Figure 3-3: Bovine vertebral samples: (a) The bovine process sample without cancellous core (sample #1), (b) the cross-section of sample #1, (c) the bovine process specimen with cancellous core (sample #2), the two perpendicular lines X and Y are the scanning directions for the reflection experiment, and (d) the cross-section sample #2.

Figure 3-4: A photo of the titanium-alloyed pedicle screw.

and 5.0 MHz (V384-N-SU and V310-N-SU, Panametrics-NDT, Waltham, MA) and the frequency of 3.5 MHz was applied for the sample with cancellous bone. The transducer was translated along two scanning directions: X and Y respectively at a discrete spatial interval of 0.5 mm. All the experiments were performed in water. All the other experimental components and acquisition procedures were the

same as those of the transmission set-up. The off-line analysis included noise-filtering and time-gain compensation (TGC).
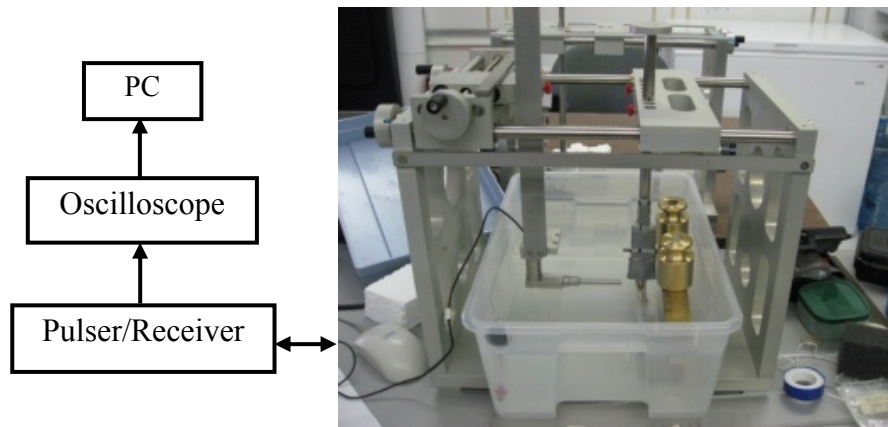
Figure 3-5: Setup for the pulse-echo experiment for bone imaging.

3.3 Results and Discussions

The experimental results of the two experimental sets I and II are presented in this section. Section 3.3.1 presents and discusses characterization results of the cortical and cancellous bones for four frequencies including their ultrasonic waveforms and acoustic property (velocity and attenuation) response to the varying frequency. Section 3.3.2 illustrates the generated B-mode bone images with and without a screw inside for the two vertebral samples (#1: no cancellous core; #2: with cancellous core). The accuracy of the ultrasound imaging method is compared with μ-CT image and discussed. The effect of cancellous core on the ultrasound bone images is verified.

3.3.1 Experimental Set I: Bone Characterization

3.3.1.1 Ultrasonic Waveforms

The ultrasonic water reference pulses of the four frequencies are shown in Figure 3-6, and their corresponding amplitude spectra in Figure 3-7, respectively. The travel times are 36.80 μs for 1.0 MHz, 36.45 μs for 2.25 MHz, 36.37 μs for 3.5 MHz, and 36.18 μs for 5.0 MHz. The time differences of the signals among these transducer pairs attributed to the experimental measuring errors were 0.9 mm. Nevertheless, the results of acoustic characterization of bone were not affected since the acoustic parameters were determined by the thickness of bone samples instead of the transducer distance, as shown in equation (3-1).

Figure 3-8 presents the pulse signal of ultrasound through the cortical bone sample for four frequencies and Figure 3-9 shows the corresponding amplitude spectra. There were no observable distortions or dispersion on the wave shapes. Only the primary transmitted pulse was observed at 1.0 MHz, while the multiple reflections within the cortex layer were invisible because the reflection was overlapped by the primary transmission signal. The frequency of 2.25 MHz was able to separate the primary and multiple reflections. The resolvability of multiple reflections from the transmission signal improved with increasing frequency. The 5.0 MHz transducer had the superior resolution.

Figure 3-10 shows examples of cancellous bone pulses for the four frequencies. Compared with the cortical bone signals, there are perceptible distortions on the wave shapes at higher frequencies over 1.0 MHz. The primary transmitted signals are composed of two signals dominated by a comparatively lower frequency and a higher frequency respectively, as the amplitude spectra

shown in Figure 3-11. Furthermore, the high frequency component is gradually compressed with increasing frequency.

3.3.1.2 Acoustic Properties of Cortical Bone and Cancellous Bone

Table 3-1 presents the statistics of the acoustic properties of the cortical specimen, for the 1.0 MHz, 2.25 MHz, 3.5 MHz, 5.0 MHz measurements, respectively. The average and standard deviation (std) are provided for group velocities, phase velocities, attenuation at the center frequencies, and nBUA. For the group velocity, the values by the first motion point and first zero crossing methods from 1.0 MHz are 2934 m/s, 2769 m/s versus 3094 m/s, 2873 m/s from 5.0 MHz, respectively. The envelop method (le, 1998) obtains a smallest value of 2553 m/s at 1.0 MHz, while the velocities at the remaining three frequencies are 2750 m/s, 2722 m/s and 2711 m/s respectively. Similar to the envelope method, the phase velocity at 1.0 MHz (2634 m/s) is smaller than the values of the other three frequencies: 2750 m/s at 2.25 MHz, 2722 m/s at 3.5 MHz, and 2738 m/s at 5.0 MHz. The measurement variation among the four frequencies for each of the three methods and phase spectra method is determined by finding the difference between the maximum and minimum values of the averaged velocities. The first motion point method has the largest variation which is up to 215 m/s. This is because the first motion point is sensitive to noise (even if it exists in small amounts) which would affect the determination of the accurate beginning point of the pulse and generate unwanted error (Nicholson *et al.,* 1996). The error among the velocities at the four frequencies by the first zero crossing method is less than 119 m/s. The unusual smaller values at 1.0 MHz by the envelope and phase spectra methods are due to

the pulse shape modification which is caused by the mixture of the primary transmission signal and the multiple. Nevertheless, the values of the phase velocities at the dominant frequency are found to agree well with those of group velocities calculated by the first zero crossing point, as reported by Nicholson *et al.* (1996). Hence, based on another experimental observation reported by Nicholson *et al.* (1996), that the first zero crossing method was optimal in the reproducibility for velocity measurement, the velocities obtained by the first zero crossing method were chosen to be averaged at the four frequencies as 2770 ± 44 m/s and utilized in this thesis as the speed of sound of cortical bone. The uncertainty involved in the averaging calculation was computed according to the uncertainty analysis equations listed in Appendix A. The total attenuation coefficient (including the transmission loss) of the cortical bone was initially computed by the amplitude spectra approach and the values from 1.0 MHz to 5.0 MHz are 24 dB/cm, 34.2 dB/cm, 59.9 dB/cm, and 87.1 dB/cm, respectively. To exclude the loss at the bone/water interfaces, the transmission loss was calculated as 13.2 ± 0.80 dB/cm by substituting the averaged bone velocity (2770 ± 44 m/s) into equation 3-6 and adding the total attenuation for correction according to equation 3-5. The corrected attenuations of cortical bone at four frequencies are 10.8 dB/cm, 21 dB/cm, 46.7 dB/cm, and 73.9 dB/cm respectively. Generally speaking, attenuation increases with increasing frequency. To gain an insight into the normalized BUA (nBUA), the slope of the best-fitted line was obtained according to the full-width-half-maximum (FWHM) of the frequency spectra where the linear portion of the curve lies. The FWHM were selected as 0.6-1.5

46

MHz for 1.0 MHz, 1.5-2.7 MHz for 2.25 MHz, 2.5-4 for 3.5 MHz, 4-5.5 MHz for 5.0 MHz. The estimated nBUAs for the four frequencies are 33.5 dB/cm/MHz for 1.0 MHz, 14.8 dB/cm/MHz for 2.25 MHz, 17.8 dB/cm/MHz for 3.5 MHz, 31 dB/cm/MHz for 5.0 MHz. Because of the unsatisfactory resolving ability of 1.0 MHz, the primary transmitted wave is mixed with the reflection wave from the cortical layer. As a result, the nBUA of 1.0 MHz is not accurate.

Table 3-2 present the statistics of the acoustic properties of the cancellous bone specimen, for the 1.0 MHz, 2.25 MHz, 3.5 MHz, 5.0 MHz measurements, respectively. The average and standard deviation are provided for phase velocities, attenuation at the center frequencies, and nBUA. The reason we do not consider the calculation of group velocities is because the porous structure of cancellous bone will generate multiple scatter signals thus affecting the accurate determination of the reference points required for the time-domain method. The phase velocities at the four frequencies are 1572 m/s, 1495 m/s, 1512 m/s, and 1543 m/s which are close to the speed of sound of water (1480 m/s). The attenuation including the loss at the interfaces is determined to be 42.6 dB/cm, 63.3 dB/cm, 75.06 dB/cm, 130.2 dB/cm. The attenuation was not modified because the transmission loss at the cancellous bone/water interface was estimated experimentally as -0.4±0.17 dB/cm (refer to Appendix B) and thus could be neglected since it is very small. Unexpectedly, the attenuation is even greater than that of cortical bone and the averaged difference at 5.0 MHz between the cortical and cancellous bones is approximately 43.1 dB/cm. The multiple scattering processes among the trabecular-water interfaces give rise to

the high attenuation. Nevertheless, the attenuation behavior of cancellous bone with frequency is similar to that of cortical bone and increases with frequency. The slope of the best-fitted line was calculated within a limited frequency window corresponding to the linear portion of the curve: 0.6-1.5 MHz for 1.0 MHz, 1.5-2.7 MHz for 2.25 MHz, 2.5-4 for 3.5 MHz, 3.5-4.5 MHz for 5.0 MHz.

Furthermore, to explore the responses of dispersion and attenuation of cortical and cancellous bones to frequency, the dispersion curves examining the travelling speeds of the frequency components and the attenuation curves are plotted in Figure 3-12 (a) and (b) respectively. Except for the inaccurate values within the main frequency band of 1.0 MHz (0.6 MHz - 1.5 MHz), the dispersions for cortical bone from 1.5 MHz to 5.5 MHz are minor. This observation suggests that cortical bone is a non-dispersive material. The dispersions of the cancellous bone within the selected frequency bands are also minor. The attenuation responses for both the cortical and cancellous bone increase quasi-linearly with frequency, similar to the previous reports in most bone studies (Langton *et al.*, 1984, 1996; Tavakoli and Evans, 1991; Wear, 2001).
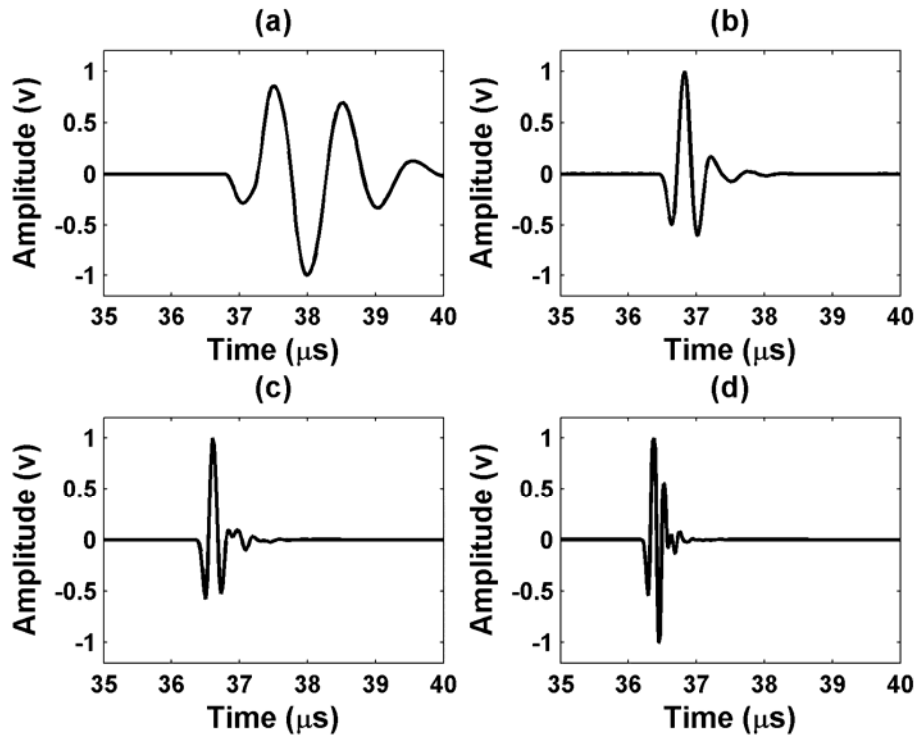
Figure 3-6: The normalized ultrasonic reference signals of four frequencies: (a) 1.0 MHz, (b) 2.25 MHz, (c) 3.5 MHz, and (d) 5.0 MHz.
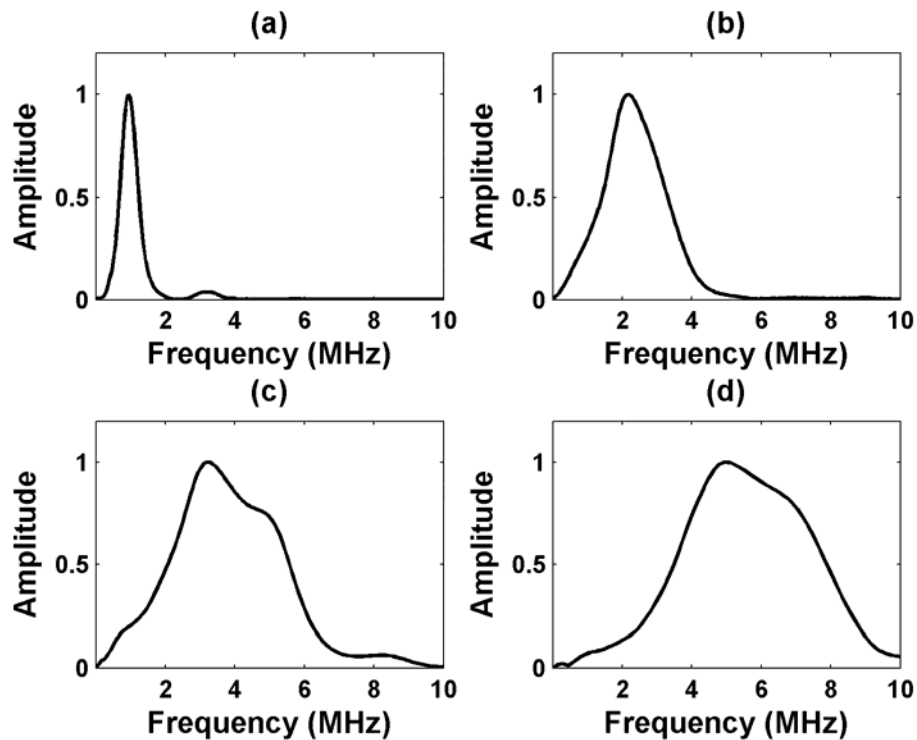
Figure 3-7: The normalized amplitude spectra of ultrasonic reference signals of four frequencies: (1) 1.0 MHz, (2) 2.25 MHz, (3) 3.5 MHz, and (4) 5.0 MHz.

49
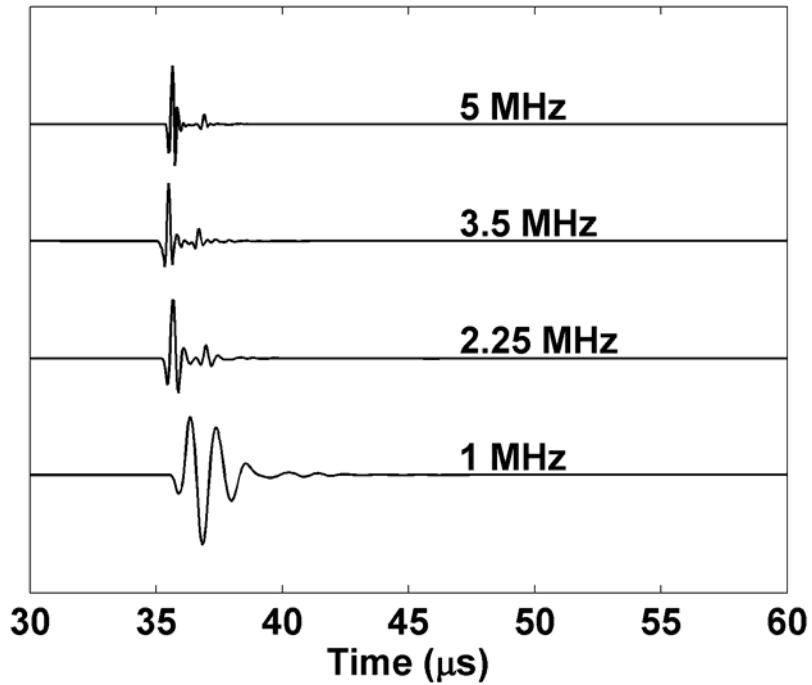
Figure 3-8: Examples of the transmitted signals through cortical bone sample for the four frequencies.
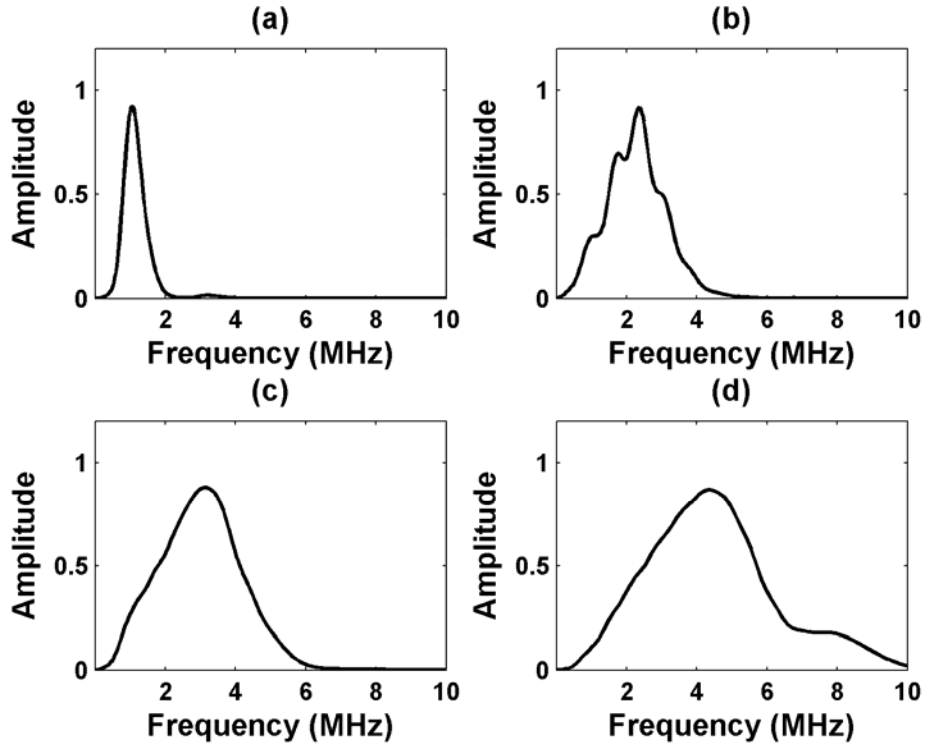
Figure 3-9: Examples of the amplitude spectra of the transmitted signals through cortical bone sample for the four frequencies: (a) 1.0 MHz, (b) 2.25 MHz, (c) 3.5 MHz, and (d) 5.0 MHz.

50
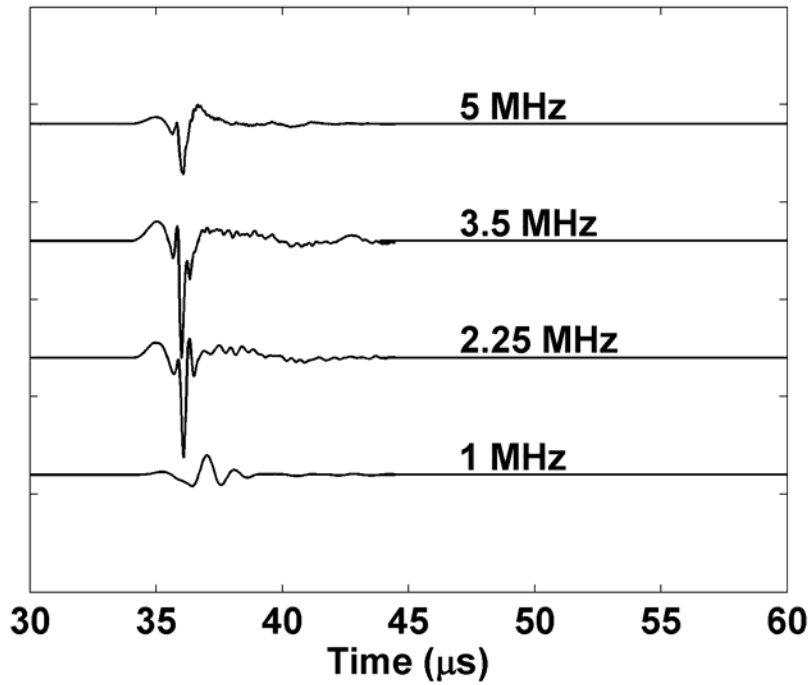
Figure 3-10: Examples of the transmitted signals through the cancellous bone sample for the four frequencies.
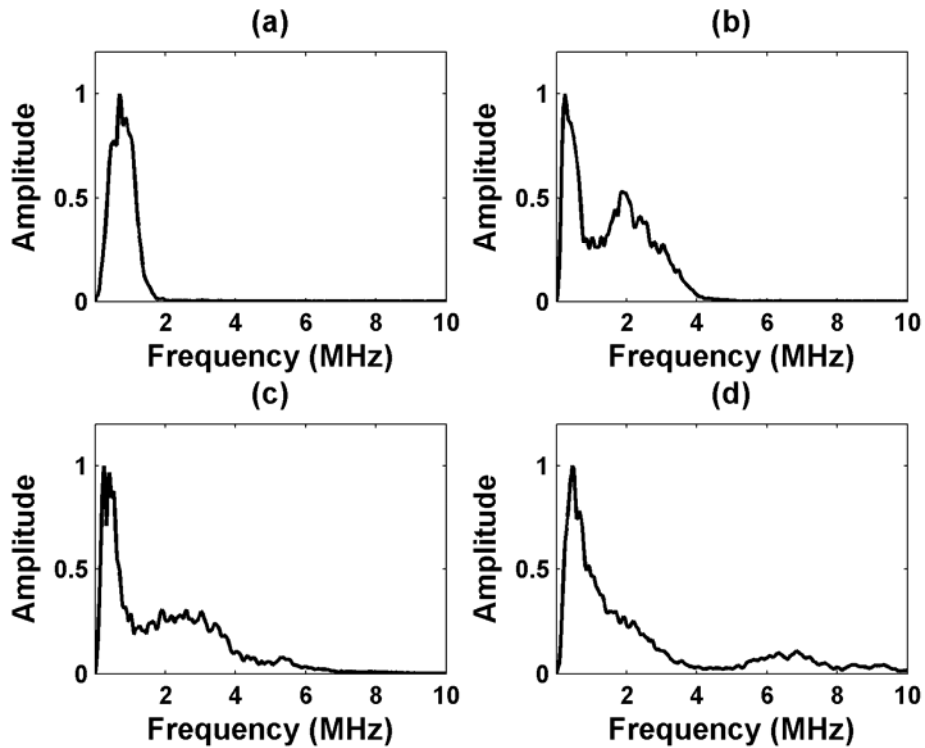
Figure 3-11: Examples of the amplitude spectra of the transmitted signals through the cancellous bone sample for the four frequencies: (a) 1.0 MHz, (b) 2.25 MHz, (c) 3.5 MHz, and (d) 5.0 MHz.

Table 3-1: Acoustic properties of vertebral cortical bone.

Acoustic property	Frequency (MHz)			
	1.0	2.25	3.5	5.0
Group Velocity (m/s)				
1st motion	2934±54	2996±63	3149±190	3094±139
1st zero crossing	2769±44	2783±57	2754±25	2873±82
envelope	2553±35	2750±73	2722±52	2721±50
Phase Velocity[1] (m/s)	2634±47	2737±55	2755±39	2738±55
Attenuation[2] (dB/cm)	24.0±2.4	34.2±3.9	59.9±5.3	87.1±10.6
Attenuation[3] (dB/cm)	10.8±2.5	21.0±3.9	46.7±5.4	73.9±10.6
nBUA[4] (dB/cm/MHz)	33.5±2.0	14.8±0.9	17.8±1.1	31.0±1.8

[1] Measured phase velocity at the dominant frequencies 1.0, 2.25, 3.5 and 5.0 MHz.

[2]Total attenuation coefficient including transmission loss at the interfaces.

[3]Attenuation excluding transmission loss at the interfaces.

[4]Frequency ranges are based on the -6 dB cutoff: 0.6-1.5 MHz for 1.0 MHz, 1.5-2.7 MHz for 2.25 MHz, 2.5-4 for 3.5 MHz, 4-5.5 MHz for 5.0 MHz.

Table 3-2: Acoustic properties of vertebral cancellous bone.

Acoustic property	Frequency (MHz)			
	1.0	2.25	3.5	5.0
Phase Velocity[1] (m/s)	1572±10	1495±4	1512±5	1543±53
Attenuation[2] (dB/cm)	42.6±0.9	63.3±1.2	75.0±1.2	130.2±5.1
nBUA[3] (dB/cm/MHz)	25.7±0.0	18.1±0.0	17.2±0.0	25.5±0.0

[1] Measured phase velocity at frequencies (1.0, 2.25, 3.5 and 5.0 MHz).

[2]Total attenuation coefficient including transmission loss at the interfaces.

[3]Frequency ranges are visually selected corresponding to the linear portion of the curve: 0.6-1.5 MHz for 1.0 MHz, 1.5-2.7 MHz for 2.25 MHz, 2.5-4 for 3.5 MHz, 3.5-4.5 MHz for 5.0 MHz.
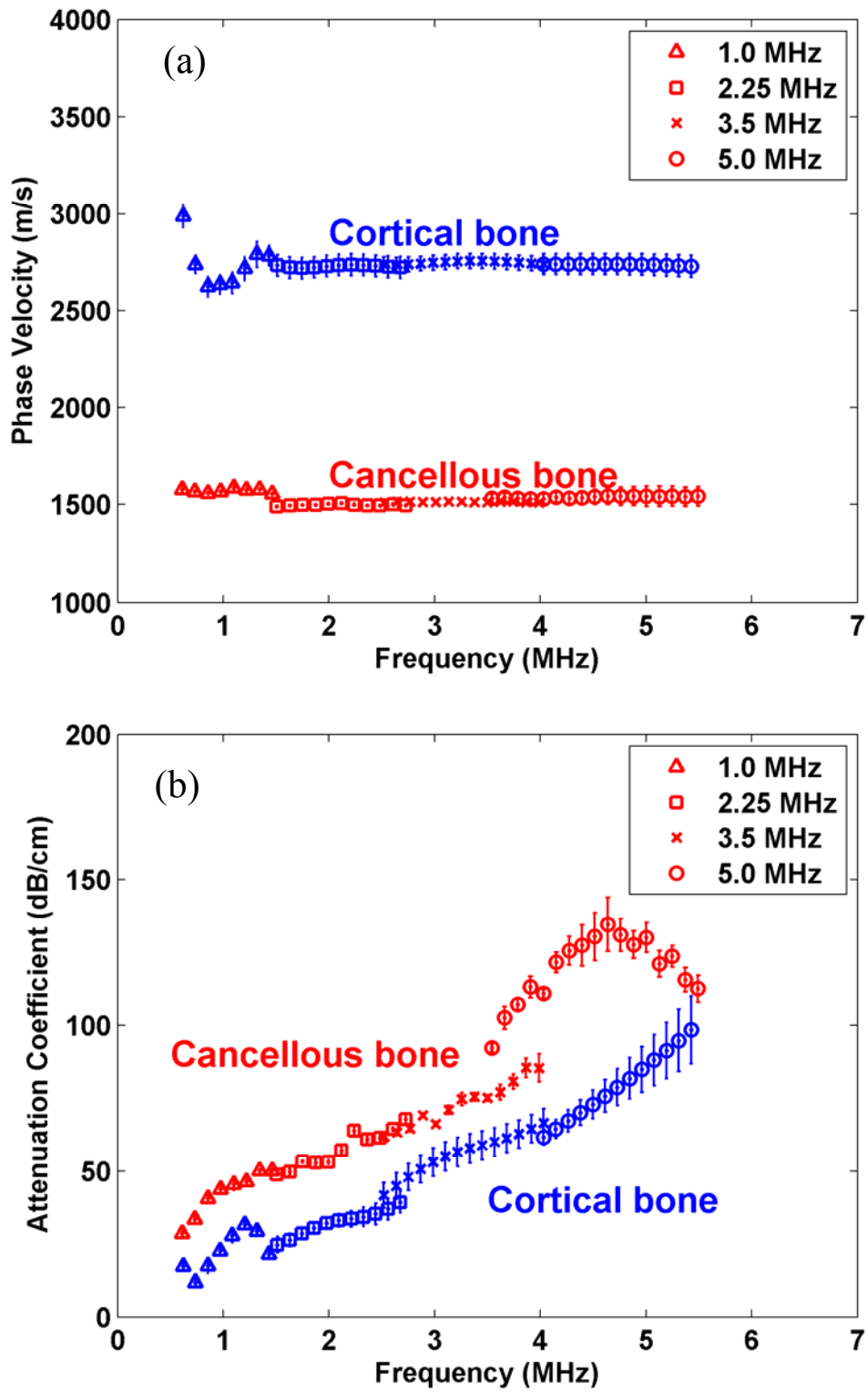
Figure 3-12: Phase velocity and attenuation versus frequency curves for the cortical and cancellous bone samples: (a) phase velocity, and (b) total attenuation.

3.3.2 Experimental Set II: Vertebral Bone Imaging

3.3.2.1   The Sample Without Cancellous Core

3.3.2.1.1   Ultrasonic Waveforms

Two transducers of 3.5 MHz and 5.0 MHz were chosen to scan the bone samples based on the experimental results in Section 3.3.1.1. The reason we select the focused transducer is to acquire a strong detectable signal with good resolution. The typical waveforms and corresponding amplitude spectra generated by the two focused transducers are illustrated in Figure 3-13. The 5.0 MHz signal has a shorter time duration and smaller cycle than the 3.5 MHz indicating comparatively higher resolving ability. Figure 3-14 displays an example of vertebral bone signals before and after appropriate time gain compensation (TGC) for each transducer. The time differences of the echoes between the two scanning frequencies relates to the transducers' position at their corresponding focal distances from the sample. Before the TGC, two early arrival echoes (R1 and R2) are strong and clearly visible; and only one late arrival signal (R3) is visually seen. Nevertheless, the amplitude of R3 is enhanced and R4 is detectable after the TGC.

3.3.2.1.2   Ultrasound Bone Images

To produce high quality ultrasound bone images, various signal processing methods were employed. Figure 3-15 illustrates the detailed procedures for data processing and analysis. To remove the high and low frequency components and improve the signal-to-noise-ratio, a trapezoidal band-pass filter was applied to the
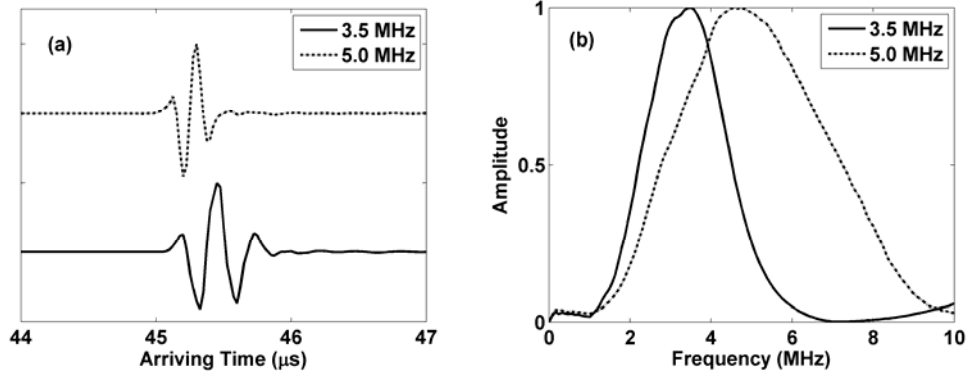
Figure 3-13: The typical waveforms (left) and corresponding amplitude spectra (right) for the 3.5 MHz and 5.0 MHz frequencies.
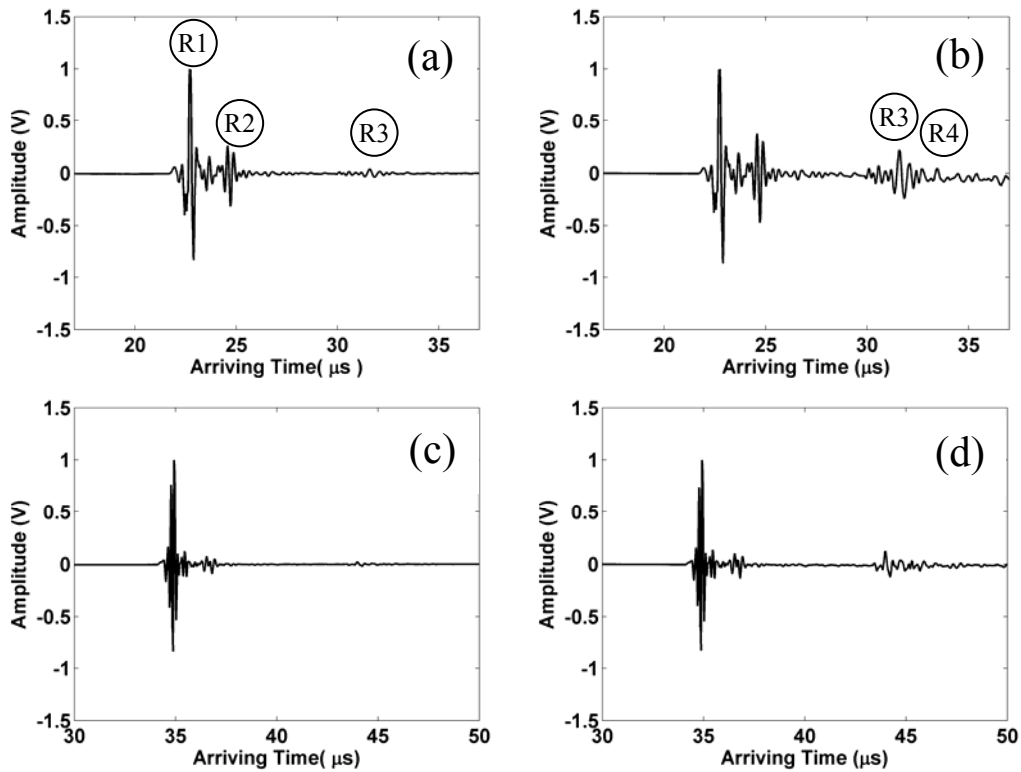
Figure 3-14: Examples of vertebral bone signals of (a) and (b) 3.5 MHz, and (c) and (d) 5.0 MHz transducers. The left column displays the normalized raw bone data and the right column is the data after appropriate TGC. R1, R2, R3 and R4 are the echo signals from the vertebral bone.

group of traces: the frequency gates are 0.4/0.5/5.0/6.0 MHz for 3.5 MHz and 0.4/0.5/8.0/9.0 MHz for 5.0 MHz. Due to high acoustic impedance contrast between the cortical bone and water and the absorptive property of the cortex, a considerable portion of the energy are attenuated during the two-way trip. As a consequence, the strength of the bone signals needs to be amplified and a regular TGC approach was applied to compensate for the attenuation. However, a drawback of the regular TGC method is that it will intensify the undesired noise signals as well as the bone signals. In order to amplify the desired echo signals only, an adaptive gain compensation (AGC) method was utilized and applied to the adaptive time-gated traces. The center of the gate window was determined as the peak point of the signal envelope.

```
          ┌─────────────────────┐
          │   Import raw data    │
          └─────────────────────┘
                     │
                     ▼
          ┌─────────────────────┐
          │  Band-pass Filtering │
          └─────────────────────┘
                     │
                     ▼
      ┌─────────────────────────────────┐
      │ Apply time gain compensation (TGC) │
      └─────────────────────────────────┘
                     │
                     ▼
          ┌─────────────────────┐
          │  Envelope detection  │
          └─────────────────────┘
                     │
                     ▼
      ┌─────────────────────────────────┐
      │  Select time gates of main pulses │
      └─────────────────────────────────┘
                     │
                     ▼
  ┌──────────────────────────────────────────────┐
  │ Apply adaptive Gain Compensation (AGC) on the gated signals │
  └──────────────────────────────────────────────┘
                     │
                     ▼
             ┌───────────┐
             │  Display   │
             └───────────┘
```
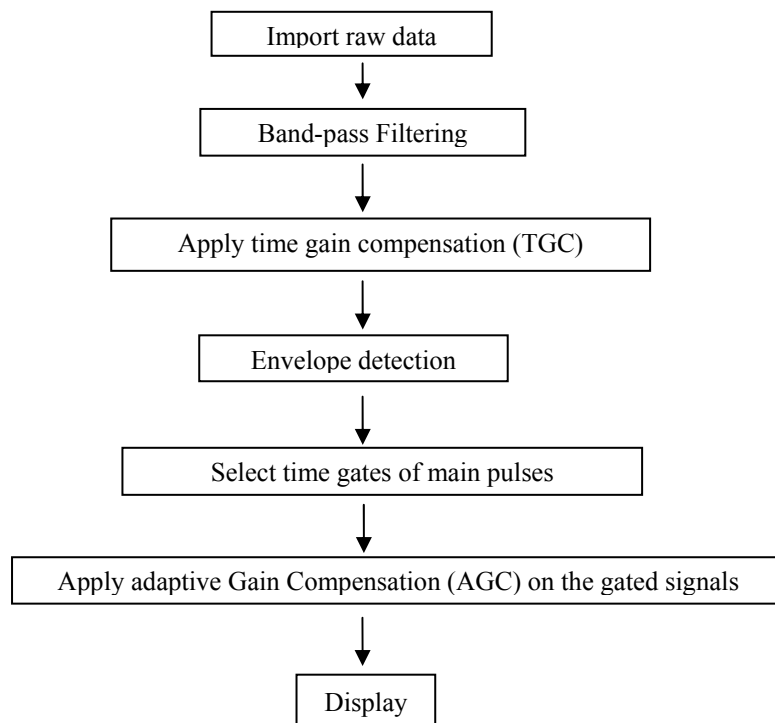
Figure 3-15: A flowchart of data processing procedure.

Figure 3-16 (a) and (b) displays the US images along the scanning X-direction for the raw bone data and the corresponding TGC data without a screw in place. The late arriving signals are visible and strong after applying TGC. Figure 3-16 (c) and (d) show the raw bone data and TGC data when the screw is in place, respectively. Due to the strong scattering caused by the inserted screw, the late arrival signals within the 20th and 30th scanning channels are still weak even after TGC application. Figure 3-16 (e) shows the time-gated AGC bone/screw data. The late arrival signals from the 20th channels to 30th are discernible. Moreover, the AGC method discloses valuable signal information hidden within the traces (as a box delineated in the Figure 3-16 (e)) which are discussed in the following section.

The colored B-mode ultrasound images or (x-t) echograms of the bone specimen for the two scanning frequencies along the X-direction are illustrated in Figure 3-17. The box delineates our region of interest (ROI). Due to the fact that the cortex and the in-filled distilled water have different acoustic impedances, four interfaces defined by the cortex and water were identified for both frequencies using the TOF method with the pre-characterized velocities of cortex (2770 m/s), water (1480 m/s), and screw (~6400 m/s). Prior to the screw insertion into the cancellous bone (Figure 3-17a and b), the first reflection (R1) is from the water/cortex interface. The signals are strong and continuous. The second reflection (R2) from the cortex/water interface is obvious and its intensity has been enhanced by appropriate TGC. Both the third (R3) and fourth reflections (R4) from the second cortical layer are visible but lack continuity. The images outside

57

and on the right of the ROI are complicated and less identifiable because the bone surface curved further away from normal incidence of the ultrasound beam; the cancellous core was getting narrower, and eventually the two cortical layers merged into a single layer as the scanning position was getting closer to the edge
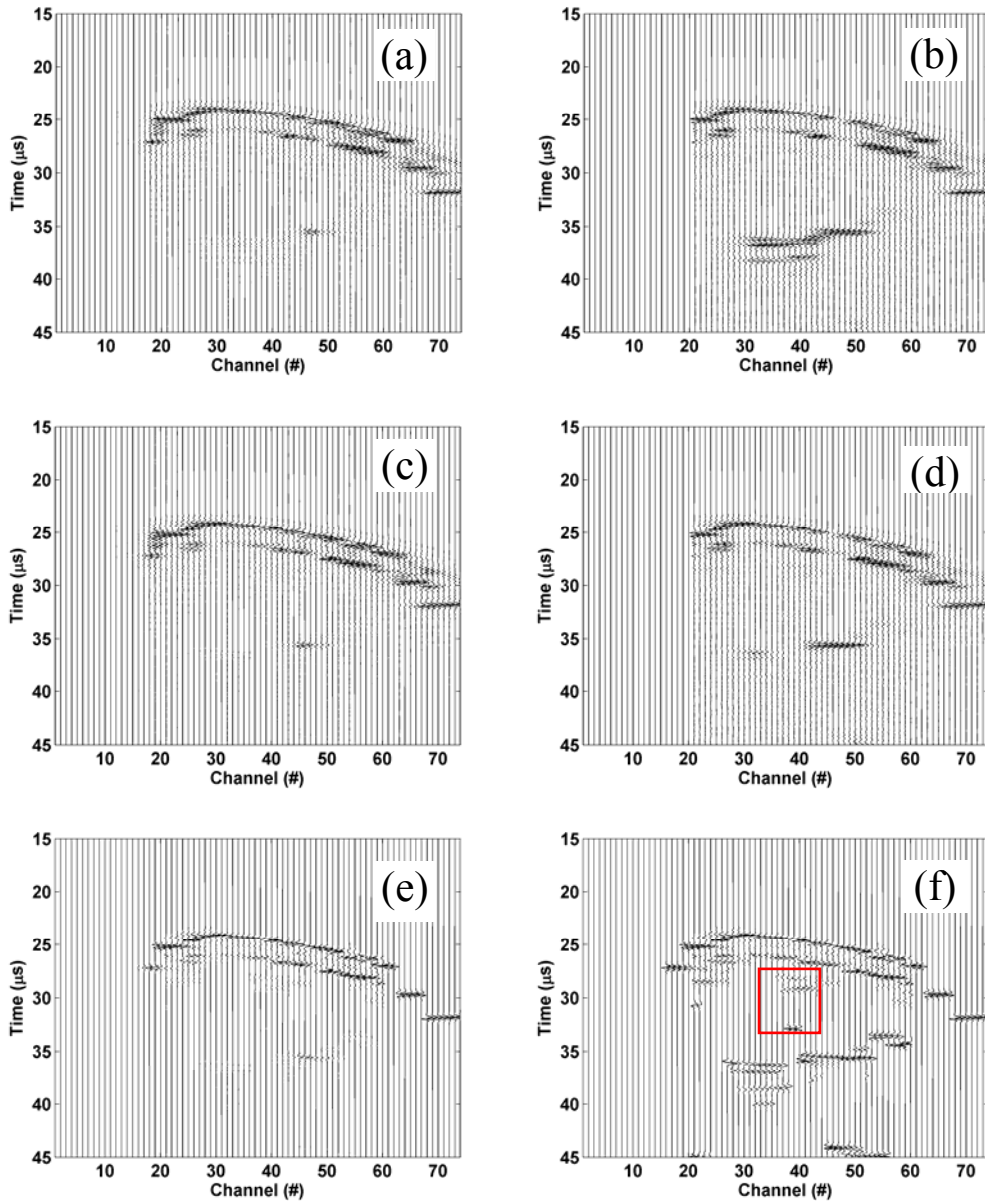
Figure 3-16: US images of vertebral sample #1 along the scanning *X*-direction for 3.5 MHz: (a) and (b) are the normalized raw bone data without screw in place and corresponding TGC data, respectively; (c)-(f) are the raw bone data with screw in place after normalization, TGC, time-gating, and AGC, respectively. The red box is the ultrasonic signals amplified by AGC.

of the bone sample (see Figure 3-1b and h). The complication was compounded by the finite size of the transducer's active element, resulting in an overlap or superposition of the echoes from closely-spaced interfaces. Finer details can be observed by the 5.0 MHz and generally, the corresponding images show less continuous or segmented reflections because the high frequency had better sensitivity than the low frequency to locate small discontinuities in the sample. When the screw was in place (Figure 3-17c and d), the R1, R2 and R3 can be identified while R4 is weak or nonexistent. S1 shows the distinct reflection from the part of the screw outside the process core. S2 is a reflection from the part of the screw inside the process core and arrives 2 μs earlier than S1 because of the higher velocity in the cortex than in water. Figure 3-17 (e) and (f) display the subtracted images between Figure 3-17 (a) and (b) (without screw) and Figure 3-17 (c) and (d) (with screw). Both S1 and S2 are clearly seen.

Figure 3-18 shows the images of two frequencies along the scanning *Y*-direction. All the interfaces (R1, R2, R3, and R4) are all visible and identified quantitatively as discussed above prior to screw insertion (Figure 3-18a and b) and after screw insertion (Figure 3-18c and d). The scanning direction was roughly parallel to the interfaces, which were approximately spaced at constant thickness. This was reflected as parallel lines in the images. S2 are the reflections from the screw as shown in Figure 3-18 (c) and (d) as well as in the subtracted images (Figure 3-18e and f).

Prior to Screw Insertion
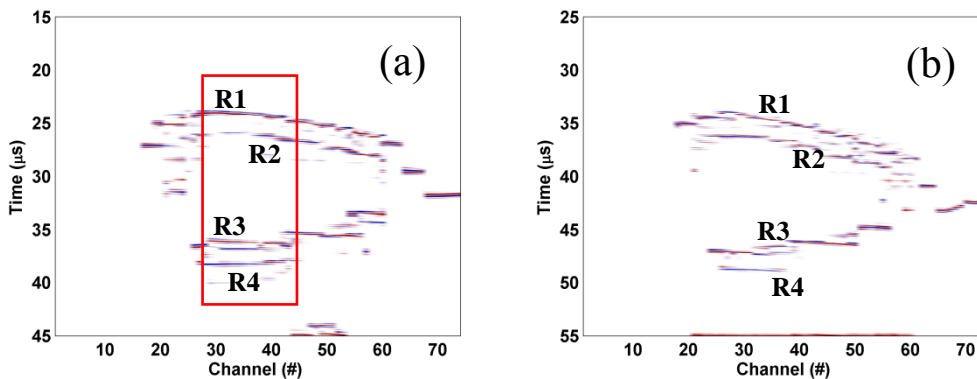
With Screw in Place
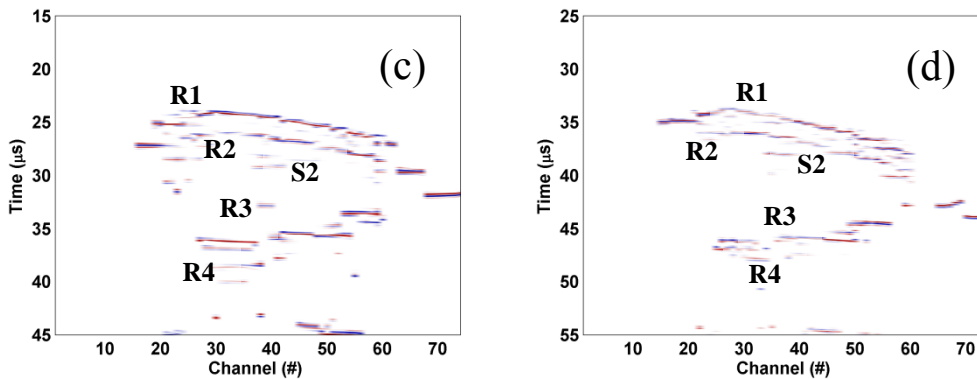
Subtracted Images
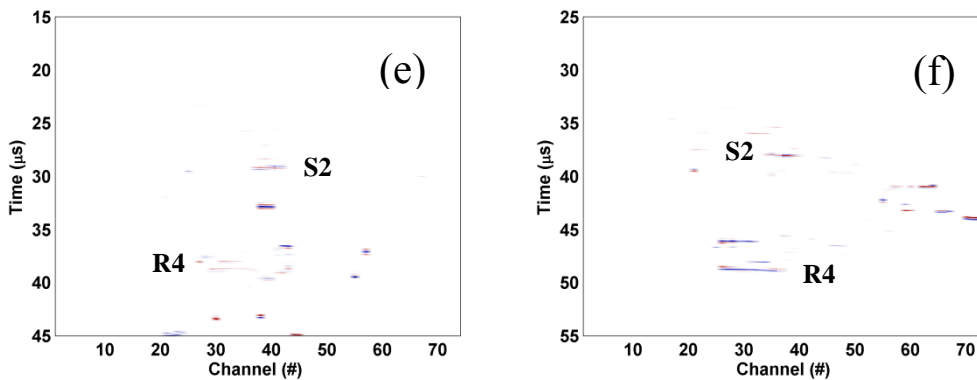
Figure 3-17: US images of vertebral sample #1 along the scanning *X*-direction for the two freuqencies: 3.5 MHz (left panel) and 5.0 MHz (right panel). The box delineates the region of interest (ROI).

Prior to Screw Insertion

(a)

(b)

With Screw in Place

(c)

(d)

Subtracted Images

(e)

(f)
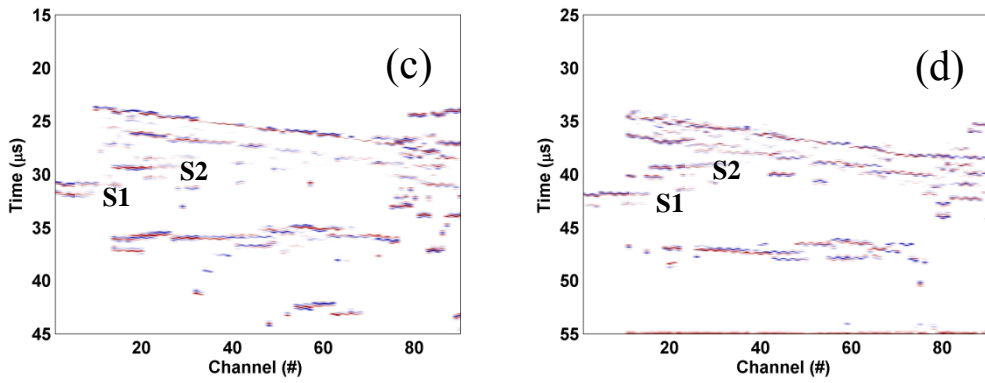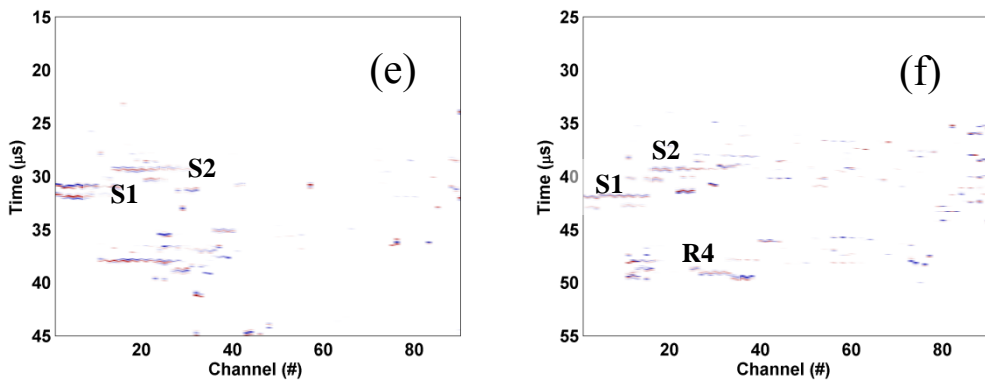
Figure 3-18: US images of vertebral sample #1 along the scanning *Y*-direction for the two frequencies: 3.5 MHz (left panel) and 5.0 MHz (right panel).

3.3.2.1.3 Comparison with μ-CT Image

In order to further verify the accuracy of the ultrasound method, we compared the thickness of the cancellous core layer measured by the two methods: US and μ-CT (skyscan 1076, SKYSCAN, Belgium). Figure 3-19 depicts the μ-CT cross-sectional image of the vertebral process. The μ-CT scans of the specimen were implemented using 35 μm thick slices. The resulting 1280×724 μ-CT digital images corresponded to a 43.94 mm × 34.85 mm field of view. The pixel size was 34.33 μm. The region bounded by the two vertical lines corresponds to the ROI in Figure 3-18 (a) and is appoximately 10 mm wide. The measurements on the μ-CT were performed within this region. The ultrasound beam of finite thickness insonifies an area of the sample instead of a point. By assuming the insonified area is 6.4 mm wide (the diameter of the transducer's element), approximately 186 pixels centred at the scanning location were averaged to provide a μ-CT-thickness. Figure 3-20 displays the thickness measurement of the twenty channels within the ROI obtained by the two methods. The US-thicknesses agree well for the two frequencies. For the first fifteen channels, the thickness differences between the ultrasound and μ-CT images are appoximately 0.31±0.23 mm for 3.5 MHz, and 0.31±0.16 mm for 5.0 MHz, respectively. However, the difference increases up to 1.0 mm for the remaining channels. The agreement deteriorates due to the surface curvature resulting in bigger ultrasonic measurement errors.
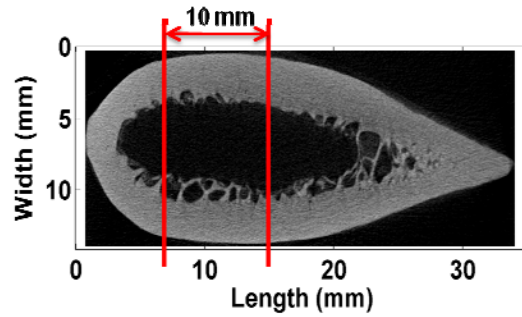
Figure 3-19: The μ-CT cross-sectional image of the bone sample #1. The region between the red vertical lines corresponds to the ROI delineated in Figure 3-15 (a).
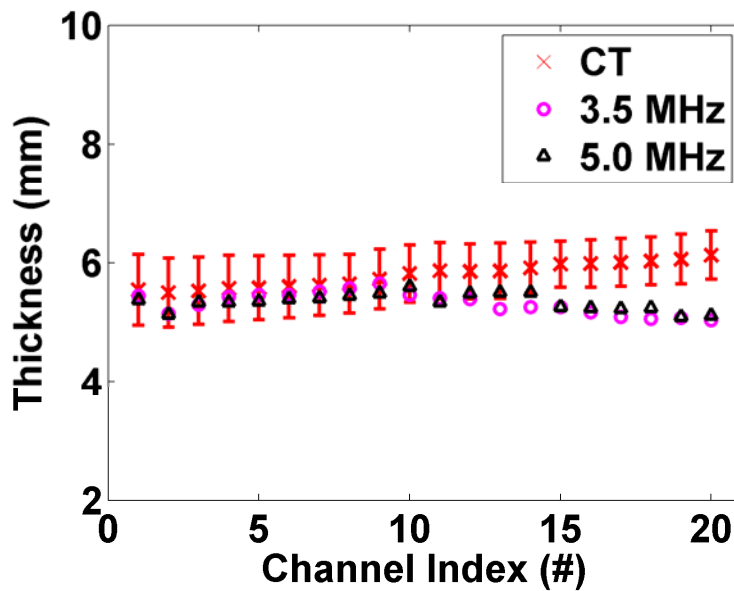
Figure 3-20: Thickness comparison between the μ-CT and ultrasound methods for the cancellous core layer within the ROI.

3.3.2.2   The Sample Filled With Cancellous Core

The same processing procedures as in section 3.3.2.1.1 were applied to the bone data. Figure 3-21 displays the raw and processed bone data without and with the screw in place along the scanning X-direction. The TGC enhances the greatly-attenuated weak late-arrival signals (Figure 3-21a-d) and the AGC method

improves the amplifications and reveals the weak signals reflected from the screw (Figure 3-21d and f).
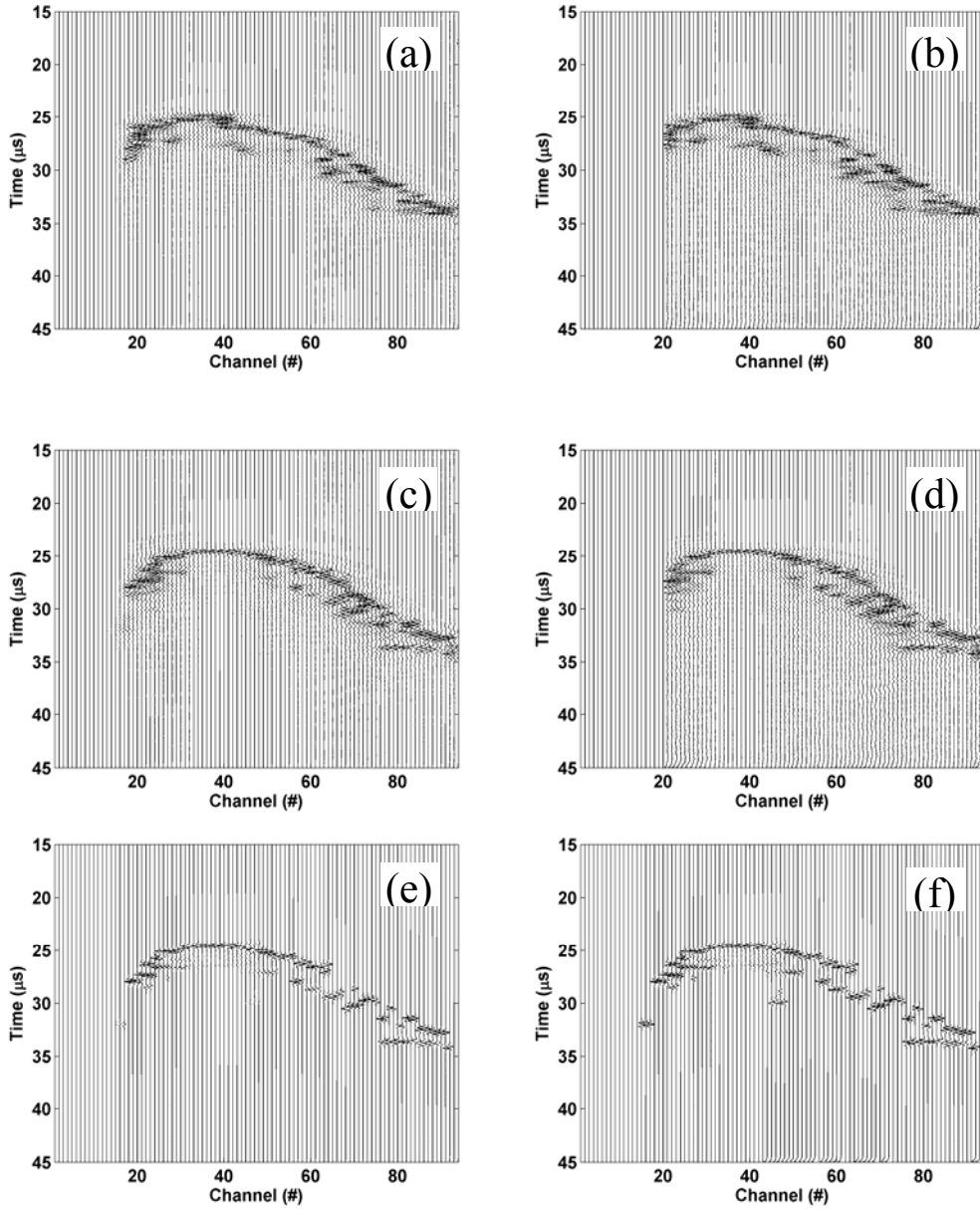
Figure 3-21: US images of vertebral sample #2 along the scanning X-direction for 3.5 MHz: (a) and (b) are the normalized raw bone data without screw in place and corresponding TGC data, respectively; (c)-(f) are the raw bone data with screw in place after normalization, TGC, envelope, and AGC, respectively.

The colored B-mode ultrasound images of the bone specimen for 3.5 MHz along the two directions are illustrated in Figure 3-22. The interfaces were identified using the velocities of cortical bone, cancellous bone and screw. Prior to the screw insertion into the cancellous bone (Figure 3-22a and c), the first reflection (R1) from the water/cortex interface and the second (R2) from the cortex/water interface are observable and continuous. However, both the third (R3) and fourth reflections (R4) from the second cortical layer can't be detected. This undesired phenomenon could be explained by a great ultrasonic energy loss occurring within the cancellous core. Considering the total attenuation during the round-trip travel through the first cortex layer (59.9 dB/cm@3.5MHz) and cancellous core (75 dB/cm@3.5MHz), the amplitude of the echo from the late cortex layer was estimated to be approximately 10^{-7} times weaker than the emitted signal. When the screw was in place (Figure 3-22b), the R1, R2, and R3 can be identified while R4 is weak or nonexistent. The reason that R3 is also detectable is because the cancellous core has been previously perforated and the portion of core without the screw was filled with water instead. S1 shows the distinct reflection from the part of the screw outside the core. S1' is a reflection from the screw inside the core and arrives earlier than S1 because of higher velocity in cortex than in water. In Figure 3-22 (d), S1' was seen without R3.

According to ultrasound theory, the frequency and penetration ability of an ultrasonic beam have a trade-off relationship, which states that the higher the frequency used, the shallower the depth of tissue that can be reached. Hence, conclusions can be deduced that the 5.0 MHz frequency can't acquire the echo

65

signals from the 2nd cortical layer when the vertebral bone is filled with cancellous bone since the lower frequency 3.5 MHz beam can't penetrate through the vertebral sample.
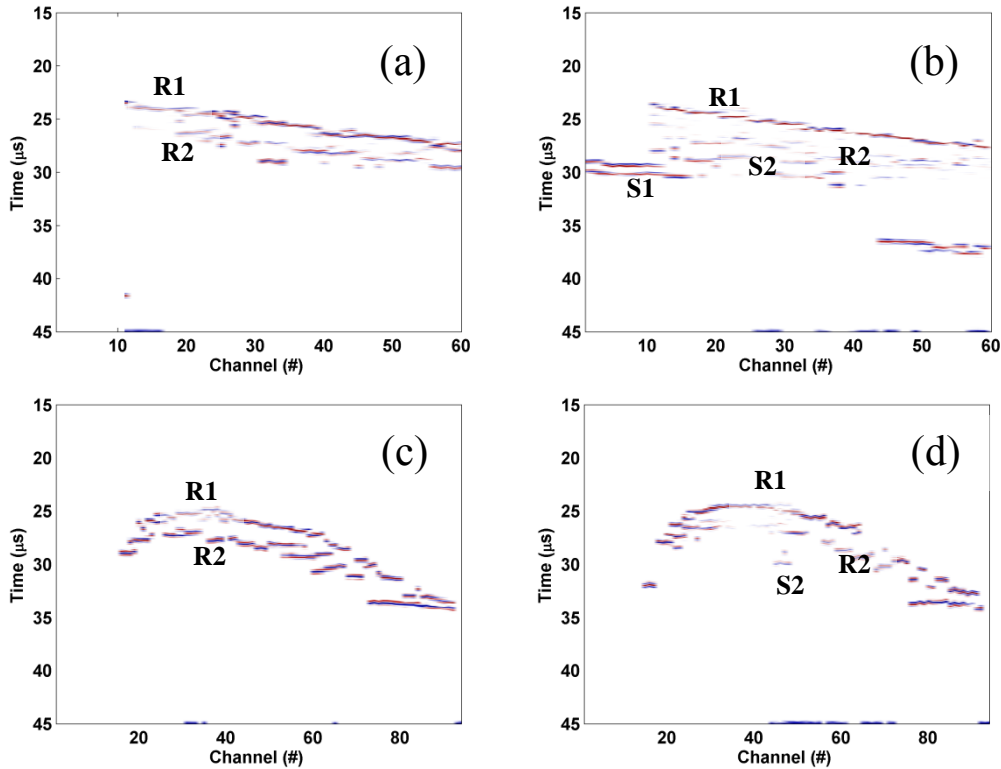
Figure 3-22: US images of vertebral sample #2 for 3.5 MHz along the two scanning directions before (left panel) and after (right panel) the screw drilled into the cancellous core.

3.4 Conclusions

In this chapter, we quantified the acoustic properties (velocity and attenuation) of vertebral cortical and cancellous bones to track the echoes from different vertebral bone layers and determine the appropriate frequencies that are able to resolve the echoes from closely-spaced bone layers, and then applied pre-determined ultrasonic frequencies (3.5 MHz and 5.0 MHz) to investigate the feasibility of the ultrasound imaging method by scanning vertebral specimens with and without a

screw inserted into the cores respectively. The results of this preliminary study are very promising. When there is no cancellous bone filled the cortical shell, all bone/water interfaces are clearly identified for both frequencies using the quantitative bone velocities. Strong reflection signals are obtained when the beam is normal to the interface but the echoes are weak or nonexistent with increased bone curvature. The thickness agreement decreases when the bone curvature increases, with the inaccuracy ranging from 6% to 20%. The acoustic property characterization experiments demonstrate that the vertebral cancellous core has a greater attenuation than the cortical shell indicating that significant ultrasonic energy loss will occur when penetrating through it due to absorption and scattering. Considering attenuation coefficients during the round-trip travel through the first cortex layer and cancellous core, the echo from the later cortex layer will be greatly attenuated. Correspondingly, only the reflection signals from the first cortex layer and the screw are quantitatively identified in the color US bone images for the bone sample with cancellous bone. Nevertheless, the screw signals are still detectable since the insertion process will destroy part of the cancellous core.

The preliminary results provide us insight about the acoustic properties of vertebral bone and demonstrate that ultrasound is able to penetrate into the vertebral bone and detect echoes from the first cortical layer and the inserted screw with satisfying resolution in a normal incidence configuration. However, the irregular surface and size of spinal vertebra bone make the current placement and size of transducer inappropriate in the clinical application. To solve the issue,

a specially-designed miniature phased array transducer consisting of at least 8 elements (6×6 mm^2) might be able to satisfy the needs when placed between the superior articular processes. To investigate this, a commercial ultrasound device - TomoScan Focus LT (Olympus, Canada) was utilized to control the transducer and generate ultrasonic beams with controlled directions, focal length, pulse width, and energy.

Chapter 4

Application of a Phased Array Technique in Vertebral Bone Imaging

This chapter presents an *in-vitro* investigation to image a vertebral bone and an inserted drill bit using the TomoScan equipment (refer to Appendix C for detailed description of the equipment). The experimental procedure consists of four steps: (1) validation of the locations of the transducer array relative to the vertebral bone sample; (2) assessment of the effect of aperture size of the array on the ultrasound bone images; (3) analysis of the effect of total element number of array on the ultrasound bone images; (4) evaluation of the ultrasound bone images response to various beam-steering angles. This chapter also attempts to justify the efficacy of this ultrasound imaging method when the drill bit is inserted into or perforates the pedicle of the vertebral bone. The equipment used was the TomoScan with a 5.0-MHz 64-element immersion linear phased array transducer. The configurations of the transducer aperture, total element number and beam-steering angles could be adjusted through the Tomoview software. The bone sample used was a porcine spine vertebra.

4.1 Materials and Methods

4.1.1 Bone Sample

A porcine spinal vertebra was prepared by disarticulating it from a pig thoracic spinal segment. All the attached soft tissues were removed. As shown in Figure 4-1 (a), the structure of the porcine vertebra is similar to that of human's and is composed of (1) spinous process, (2) transverse process, (3) lamina, (4) vertebral body and (5) pedicle. Due to the fact that the dimension of the transducer array at hand is much greater than the proposed transducer's placement location (shown by an arrow in Figure 4-1a), the placement of the transducer on the bone sample was an issue. In order to place the transducer properly, the spinous process, laminas and right-sided pedicle of the vertebral specimen were mechanically removed by a hand saw. The outer width of the left-sided pedicle bone was measured to be 8.73 mm using a digital caliper. Figure 4-1 (b) and (c) show the front and side views of the truncated specimen. A hole was drilled through the left-sided pedicle and further into the vertebral body by means of a hand drill (Figure 4-1d and e). The hole was 4.56 mm wide in diameter. The estimated distance from the outer wall of the ventral pedicle to the lateral wall of the water-infilled hole was 6.65 mm assuming the hole was precisely drilled at the centre of the pedicle bone. The specimen was then defatted using a water jet and well preserved in the methanol solution before the experiment.

In this experiment, a 50 mm (L) × 2.7 mm (W) steel drill bit (Figure 4-2) was used as the inserting metal into the pedicle bone through the pre-drilled hole.
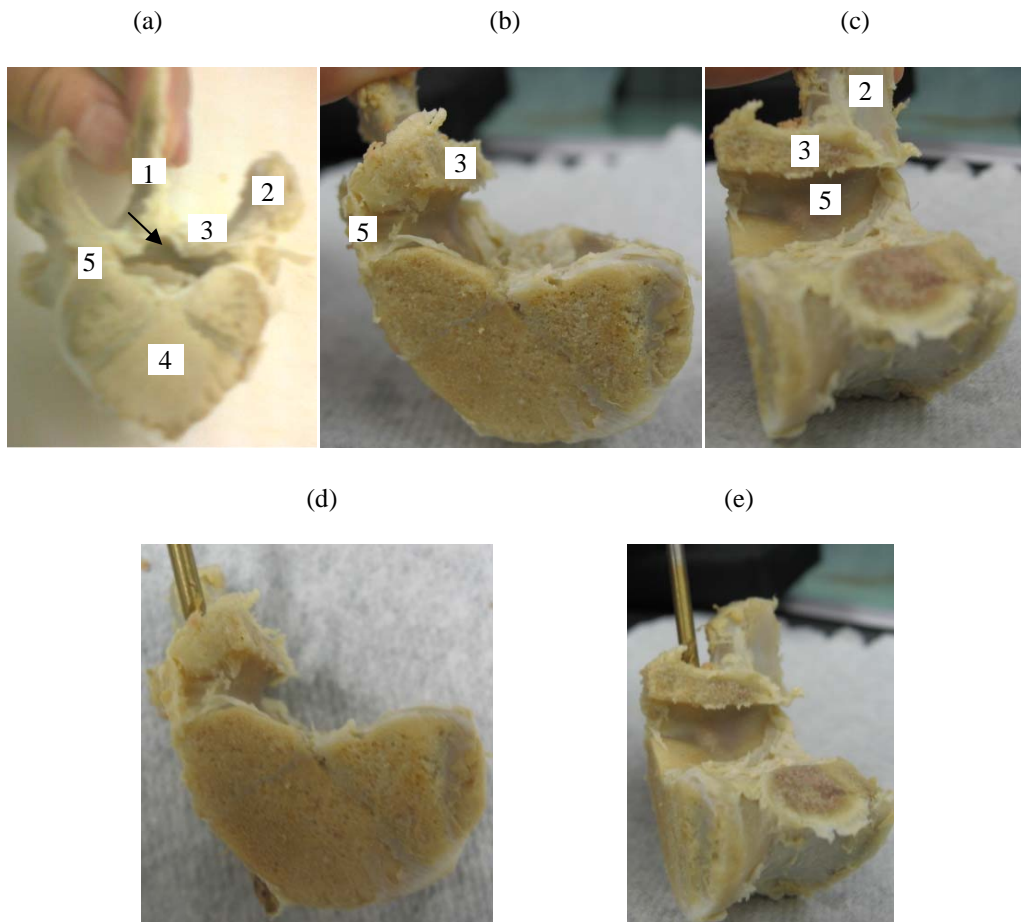
Figure 4-1: The porcine vertebral specimen. (a) The front view of the porcine vertebral specimen before cutting. The arrow indicates the space for positioning the transducer; (b) the front view of the specimen after the cut; (c) the side view of specimen. The numbers denote 1- spinous process, 2-transverse process, 3- lamina, 4- vertebral body, and 5- pedicle; (d) penetration of a metal drill bit along the pedicle bone into the vertebral body, (e) the side view of (d).

Figure 4-2: The photos of a steel drill bit (left) and its width (right).

4.1.2 The Experimental Set-up

Figure 4-3 shows the experimental setup including a holder, a water tank, and the TomoScan scanner Equipment. The holder fixed the transducer in position and allowed horizontal and vertical translations by manually adjusting its two arms. Both the transducer and the sample were immersed in water. The scanner (Olympus, Canada) was used to pulse the transducer, record, process and display the signals. The 5.0-MHz 64-element linear phased array transducer (5L64-I1) was used in this study (refer to Appendix C).

Figure 4-4 illustrates the three relative orientations of the transducer and specimen. The first orientation had the pedicle surface parallel to the transducer (Figure 4-4a). For the second orientation, the bone sample was rotated 90° horizontally and clockwise (Figure 4-4b). For the third orientation, the transducer was tilted at 45° clockwise. Among the three orientations, only the first orientation is a normal incidence case. The first, second, and third orientations are hereby denoted as *parallel*, *perpendicular* and *45°* positions respectively. The sample was located within the focal length of the transducer. The experiments were performed at room temperature. A small amount of detergent was added to the water to reduce the surface tension of water to eliminate the air bubble.
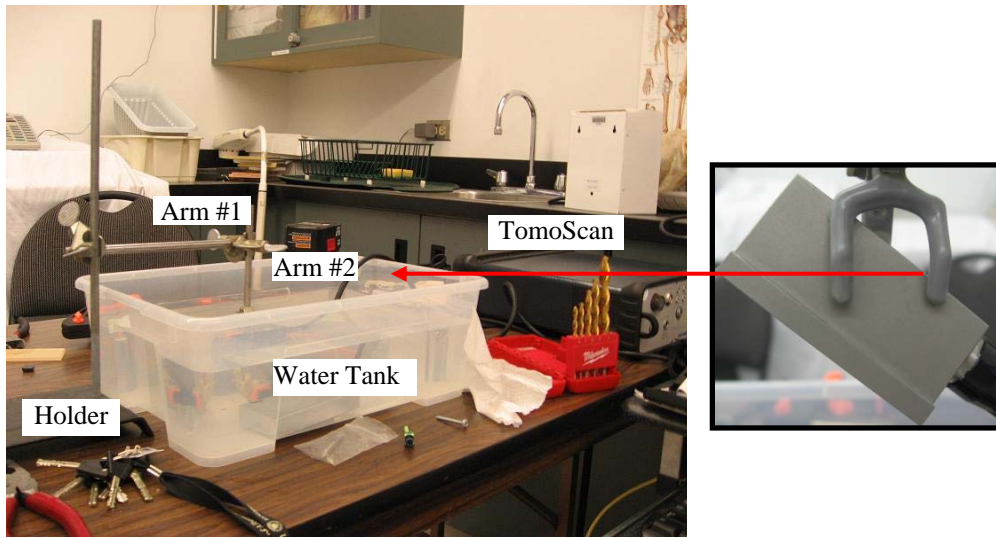
<div align="center">(a)   (b)</div>

Figure 4-3: The phased array experiment set-up. (a) The experimental set-up includes a holder, a water tank, and the scanner; (b) The transducer was held tightly by the arm #2.

<div align="center">(a)   (b)   (c)</div>

Figure 4-4: Illustration of the three relative orientations of the transducer with respect to the bone specimen. (a) The image shows the parallel orientation where the pedicle face is parallel to the transducer surface. (b) The image can be obtained from (a) by rotating the bone sample horizontally 90^0 clockwise. (c) The image displays the transducer at 45^0 with respect to the pedicle surface.

4.1.3 The Experimental Procedures

Scanning was performed with various aperture sizes, total element number, and steering angles. The focal length of the transducer was set between 5 mm and 25 mm to ensure focusing. The transducer was excited by a 35 ns pulse of 40 V. A

<div align="center">73</div>

water speed of 1480 m/s was used to determine depth or distance. All the digitized waveforms were continuously averaged 16 times and filtered by a low-pass filter (2.25 MHz) and a high-pass filter (7.0 MHz) respectively. The images were then exported for off-line analysis without further image processing.

For the parallel position, a group of 4 elements was used to produce a scan line. Since the active aperture is equal to the multiplication of the element number in an active group with pitch size, aperture size was 2.4 mm (4×0.6 mm) in our case. The firing started from the 15th transducer element to the last 64th element with a total of 50 elements to provide a broader coverage or scan field of view. The first 14th elements were not used because they were outside the target range due to the fact that the transducer is longer than the bone sample The functionality of 'improved resolution' provided by the software was also utilized to obtain bonus scanning lines to improve the image resolution. Consequently, there were ninety two scanning lines in total for this scanning configuration. The relevant parameters for the three experimental configurations are summarized in Table 4-1, where we considered a 0^{0} steering angle.

In order to identify the sources of the ultrasound signals displayed on the ultrasound bone images, the metal bit was placed on different parts of the vertebral specimen to produce different bone images. Four bit placements were considered: (1) on the top of the lamina and transverse process (Figure 4-5a), (2) over the center of the vertebral body (Figure 4-5b), (3) into the pre-drilled hole of the pedicle bone (Figure 4-5c), and (4) in external contact to the ventral cortex of the pedicle bone to mimic a medial perforation (Figure 4-5d).

74

Table 4-1: Scanning parameters for the three experimental configurations.

Configuration #	Positions of the transducer's surface with Pedicle bone	Total Number of Elements	Firing Starts from	Firing Stops at	Aperture (Number of Elements)	Number of Scan Lines	Steering Beam Angle
I	Parallel	50	15			92	
II	Perpendicular	10	55	64	4	12	0^0
III	~45^0	10	55			12	

(a)   (b)

(c)   (d)

Figure 4-5: Illustrations of four drill bit placements: (a) the drill bit was put on top of the lamina and transverse process. The drill bit was along the length of the transducer array; (b) the drill bit was put over the vertebral body. The drill bit was along the length of a transducer element; (c) the drill bit was inserted into the pre-drilled hole into the pedicle bone and further into the vertebral body; (d) the drill bit was positioned externally in contact to ventral cortex of the pedicle bone.

For the other two positions (perpendicular and 45^0), scanning parameters were the same except that the total element number was reduced from 50 to 10 with the

55th element as the firing element. Consequently, the scan field of view was reduced to twelve scan lines.

4.1.3.1 Selection of Aperture Sizes

The configuration I (Table 4-1) was used to study the effect of aperture sizes on the ultrasound images. The chosen configuration had the merit that it would produce more scan lines, providing better image quality to visualize the bone/drill bit interfaces. While all parameters are held the same, the aperture size was varied from 1.2 mm (2 active elements) to 4.8 mm (8 active elements). Table 4-2 summarizes the scanning parameters for the experiments

Table 4-2: Scanning parameters used to study the effect of aperture size.

Configuration #	Positions of the transducer's surface with Pedicle bone	Total Number of Elements	Firing Starts from	Firing Stops at	Aperture (Number of Elements)	Number of Scan Lines	Steering Beam Angle
I	Parallel	50	15	64	2	96	0^0
					4	92	
					8	84	

4.1.3.2 Selection of Total Element Numbers

Configuration I was also chosen to study the effect of total element numbers. In this case, all parameters are held constant with the exception of the first firing element and ending element. The firing element started at 15 and 25 while the ending elements stopped at 64 and 44 accordingly. The resultant total elements for the three firing/ending element (15/64, 25/64, and 25/44) combinations used were

50, 40, and 20 respectively. Correspondingly, the numbers of scan lines were 92,

72, and 32. Table 4-3 summarizes the scanning parameters and combinations for

the experiments.

Table 4-3: Scanning parameters used to study the effect of total element numbers.

Configuration #	Positions of the transducer's surface with Pedicle bone	Total Number of Elements	Firing Starts from	Firing Stops at	Aperture (Number of Elements)	Number of Scan Lines	Steering Beam Angle
I	Parallel	50	15	64	4	92	0^0
		40	25	64		72	
		20	25	44		32	

4.1.3.3 Selection of Steering Beams

All three configurations listed in Table 4-1 were tested for various steering beam

angles. For configurations I and III, the ultrasonic beams were steered from 0° to

30^0, 60^0, -30^0, and -60^0, respectively. Regarding the perpendicular position, only

the beam angles towards the left-sided pedicle bone (30^0 and 60^0) were considered.

Table 4-4 displays the transducer configurations for the beam angle experiments.

Table 4-4: Transducer configurations for experiments using different beam steering angles.

Configuration #	Positions of the transducer's surface with Pedicle bone	Total Number of Elements	Firing Starts from	Firing Stops at	Aperture (Number of Elements)	Number of Scan Lines	Steering Beam Angle
I	Parallel	50	15	64	4	92	0^0, 30^0, 60^0, -30^0, -60^0
II	Perpendicular	10	55			12	0^0, 30^0, 60^0,
III	$\sim 45^0$	10	55			12	0^0, 30^0, 60^0, -30^0, -60^0

4.2 Results and Discussions

4.2.1 The Effects of Transducer Orientations

Figure 4-6 shows a series of B-mode color ultrasound (US) images for the parallel orientation. The images show the various placements of the drill bit with respect to the bone sample (Figure 4-5). The horizontal axis of the two-dimensional (2D) images corresponds to the index axis of the transducer array and the vertical axis to the scanning depth. The origin of the horizontal axis refers to the location of the first scan line, which corresponds to the location of the 15th element in this case. Since the scan started from the 15th element and ended at the 64th element, the horizontal axis ranges approximately from 9.5 mm and 36.5 mm.

Figure 4-6 (a) is the US image without drill bit intervention. Strong reflection signals from the vertebral bone can be observed. The distinguished echoes from the ventral pedicle layer are strong and continuous, while the echoes from the lamina and vertebral body are comparatively weaker and less continuous. This is because in this orientation, the US beam was normal to the bone surface ensuring a maximum penetration of the ultrasonic beam into the pedicle bone. However for lamina and other parts, the beam was not normal to the interfaces, thus reducing their reflection signal intensities. In addition, a signal cluster was clearly detected right below the ventral pedicle signal and were quantitatively identified as the echoes from the lateral layer of pedicle bone (the lateral wall of the water-infilled hole) since the distance between the two signal clusters (6.8 mm) agrees with the pre-estimated distance of 6.65 mm (refer to section 4.1).

78

Using the US images without drill bit (Figure 4-6a) as the reference, we compared the other images (Figure 4-6b-e). Based on the fact that the difference among these five acquisitions are caused by the different placements of the steel bit, the echoes from the drill bit, lamina, transverse process, pedicle and vertebral body are identified. Figure 4-6 (b) shows the bone images with the bit placed on the lamina. Because the beam was normal to the bit and the strong acoustic contrast of the bit with water, strong echoes from the bit were detected as expected. The reflections from the drill bit are discontinuous and step-like, conforming to the helical ridge shape of the metal bit. Figure 4-6 (c) displays the bone images with drill bit positioned on the vertebral body. Similar to Figure 4-6 (b), strong signals from the bit are seen next to the vertebral body and multiple reflections between the bit ridges were recorded. Figure 4-6 (d) presents the US images with the bit inserted into the pre-drilled pathway inside the pedicle, and Figure 4-6 (e) the US images with the bit in external contact with the ventral pedicle layer. The signals reflected from the bit are identified right below and above the ventral layer of pedicle bone. Both of them are strong and obvious. However, due to the high acoustic contrast of the bit with water, only a small amount of US energy was transmitted. As a result, the signals from the lateral pedicle layer were too weak to be detected when the bit was inserted into the hole and the signals from the ventral pedicle layer became discontinuous when the drill bit was in contact to the pedicle.

Figure 4-7 shows the US images for the perpendicular orientation. Since the number of total elements was reduced to 10, the number of scan lines decreased

accordingly. Since the beam coverage was smaller, the images had poor resolution. The index axis of these ultrasound images begins and stops approximately at 32.7 mm and 36.5 mm, respectively. The images do not show the pedicle bone and the inserted bit. Nevertheless, the signal from the bit could be clearly detected when it was positioned in external contact to the pedicle bone, indicating that a medial drill bit penetration could be monitored. The same observation was obtained from the images for the 45^0 orientation (Figure 4-8).

4.2.2 The Effect of Aperture Sizes

We chose Configuration I to study the effect of aperture size on the US image due to its broader coverage of the sample. As we increase the aperture size, more active elements will be used. As expected, the echo strength will be stronger as more incident energy will be available due to more elements are activated; more averaging effect will occur as some of the closely spaced energy clusters will become continuous. Also, lateral resolution of the beam will deteriorate. These can be observed in the following US images.   Figure 4-9 (a)-(c) displays the bone images without drill bit using an aperture size of 2, 4 and 8 elements respectively. The bone signals in Figure 4-9 (a) are comparatively weaker and less continuous than those in Figure 4-9 (b) and (c). The US image with an aperture size of 8 elements has the highest signal intensity (Figure 4-9c). Figure 4-10 (a)-(c) display the bone images with the drill bit inside the pedicle using the three apertures. Like the previous observations, 8 element aperture records the strongest bone/drill bit signals than the other two apertures. However, increasing the aperture size within
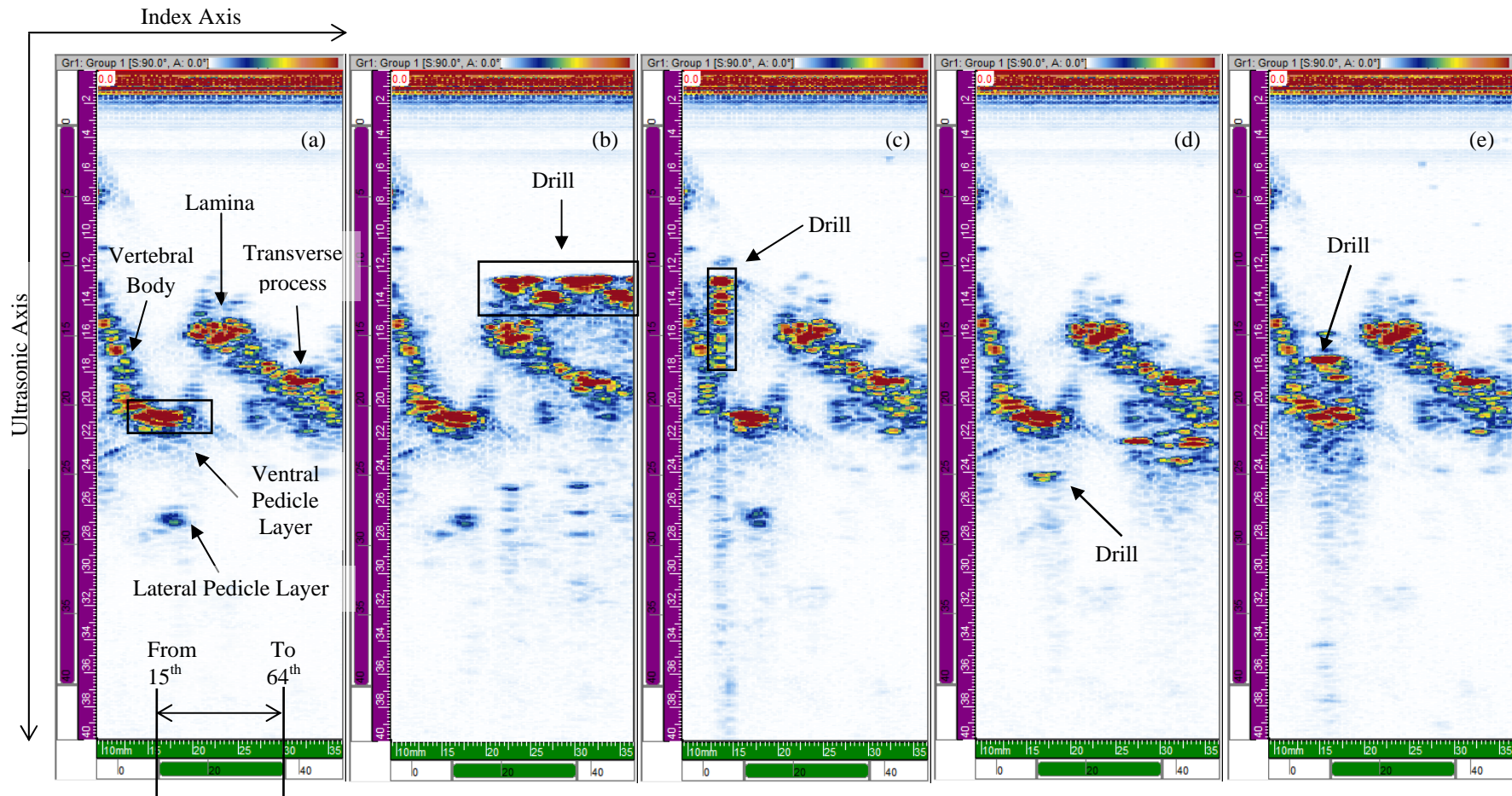
Figure 4-6: B-mode ultrasound images of the vertebral bone for parallel orientation: (a) no drill bit, (b) drill bit on the lamina and transverse process, (c) drill bit over the vertebral body, (d) drill bit inside the pedicle, and (e) drill bit contact to the ventral cortex of the pedicle to mimic a medial penetration.

Index Axis →

(a) Gr1: Group 1 [S:90.0°, A: 0.0°] - Sector (S

Ultrasonic Axis

Vertebral
Body

From
55th

To
64th

(b) Gr1: Group 1 [S:90.0°, A: 0.0°] - Sector (S

(c) Gr1: Group 1 [S:90.0°, A: 0.0°

0.07
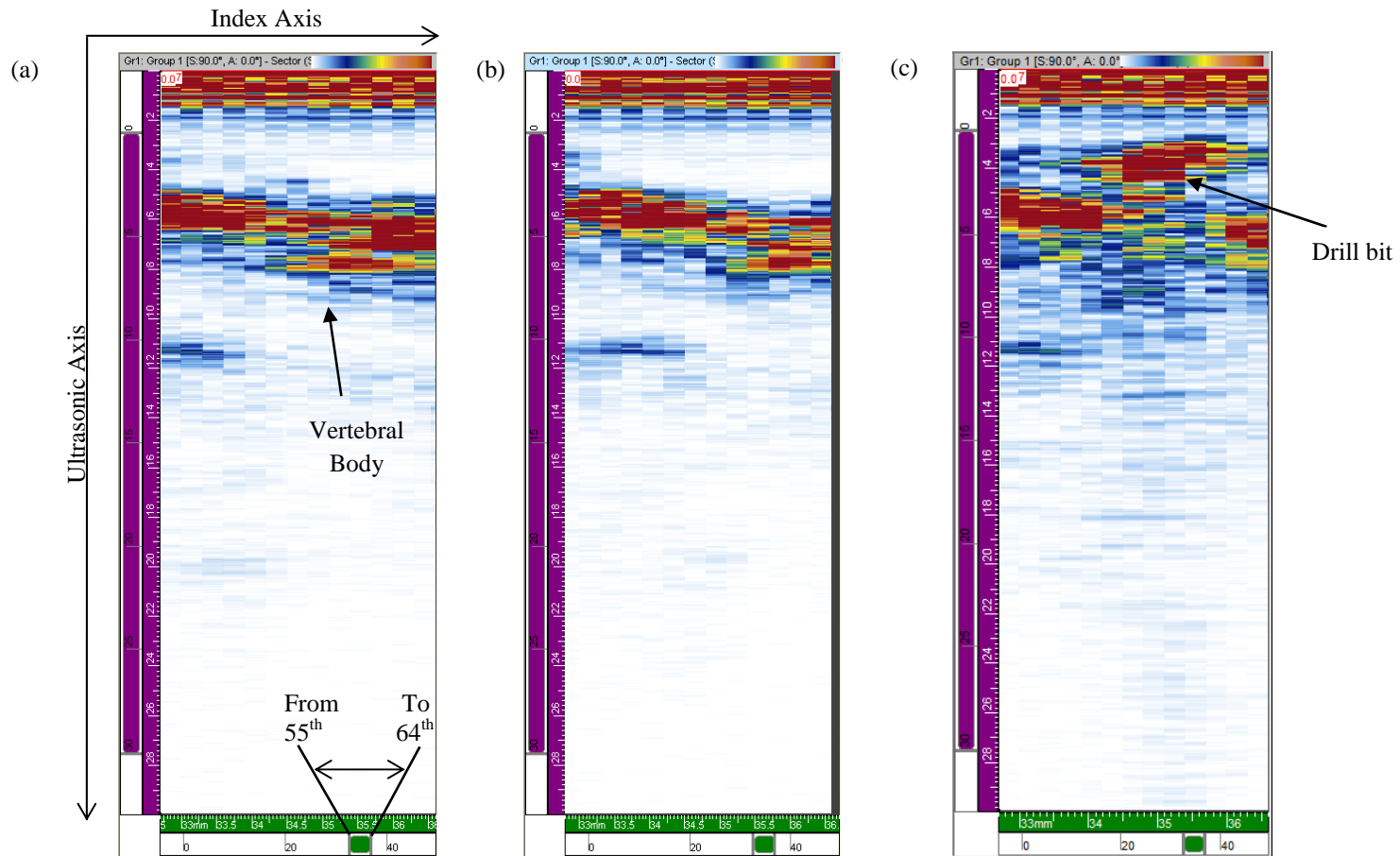
Drill bit

Figure 4-7: B-mode ultrasound images of the vertebral bone for perpendicular orientation: (a) no drill bit, (b) drill bit inside the pedicle, and (c) drill bit contact to the ventral cortex of the pedicle to mimic a medial penetration.
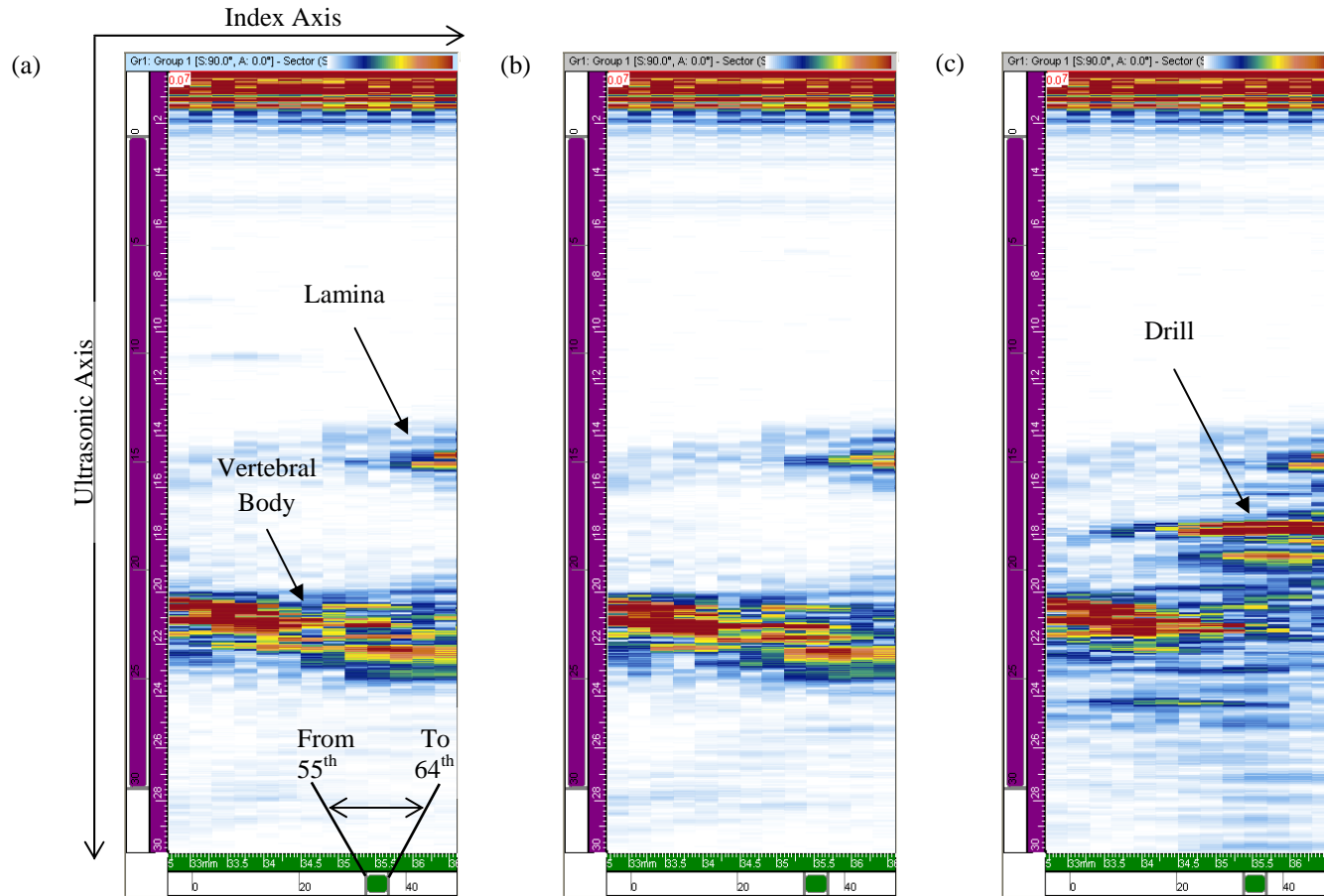
Figure 4-8: B-mode ultrasound images of the vertebral bone for 45^0 orientation: (a) no drill bit, (b) drill bit inside the pedicle, and (c) drill bit contact to the ventral cortex of the pedicle to mimic medial penetration.

the same elements array would decrease the number of scan lines which in turn would reduce the coverage. By using the electronic caliper, the index lengths of the 2-, 4-, and 8-element-aperture-images were measured as 28.5 mm, 27 mm, and 25 mm respectively. The scanning length loss is up to 3.5 mm when increasing the aperture elements from 2 to 8 elements. Therefore, considering the trade-off between the scan length and signal intensity, a 4-element aperture would be an optimal choice for vertebral bone imaging.

4.2.3 The Effect of Total Element Numbers

As before, Configuration I was used with a 4-element aperture size. Figure 4-11 (a)-(c) displays the bone images without the drill bit using a total element number of 50, 40 and 20, and Figure 4-12 (a)-(c) are the corresponding bone images with the drill bit inside the pedicle bone. The US images show the pedicle bone and inserting steel bit. The signal intensities remain the same and were not affected by the modifications of the total element number. However, the total element number is directly related to the number of scan lines when keeping the aperture size unchanged. Hence, an observable effect of the total element number on the US images is the change of scanning coverage. Since the scanned area is mapped to a fixed display size, the smaller coverage will provide blocky and stretched images. The lengths of the index axes were measured using the electronic caliper as 27 mm for element number of 50, 22 mm for element number of 40, and 12 mm for element number of 20. When the total number of array element is under 8, the index length of the generated image is expected less than 4 mm which is lower
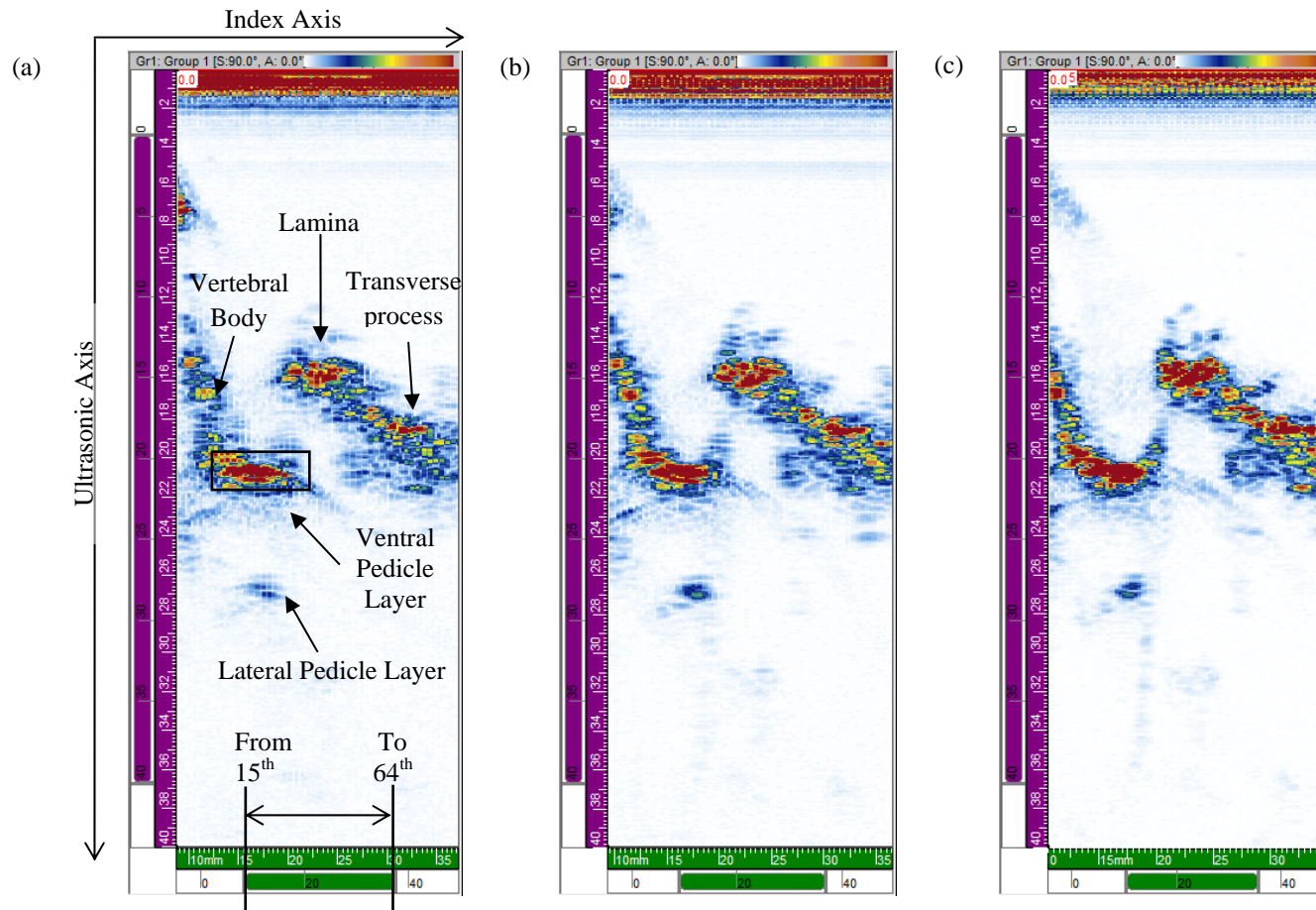
Figure 4-9: Effect of aperture sizes: B-mode color ultrasound images of vertebral bone without drill bit using an active group of (a) 2 elements, (b) 4 elements, and (c) 8 elements. The acquisitions were performed for the parallel orientation.
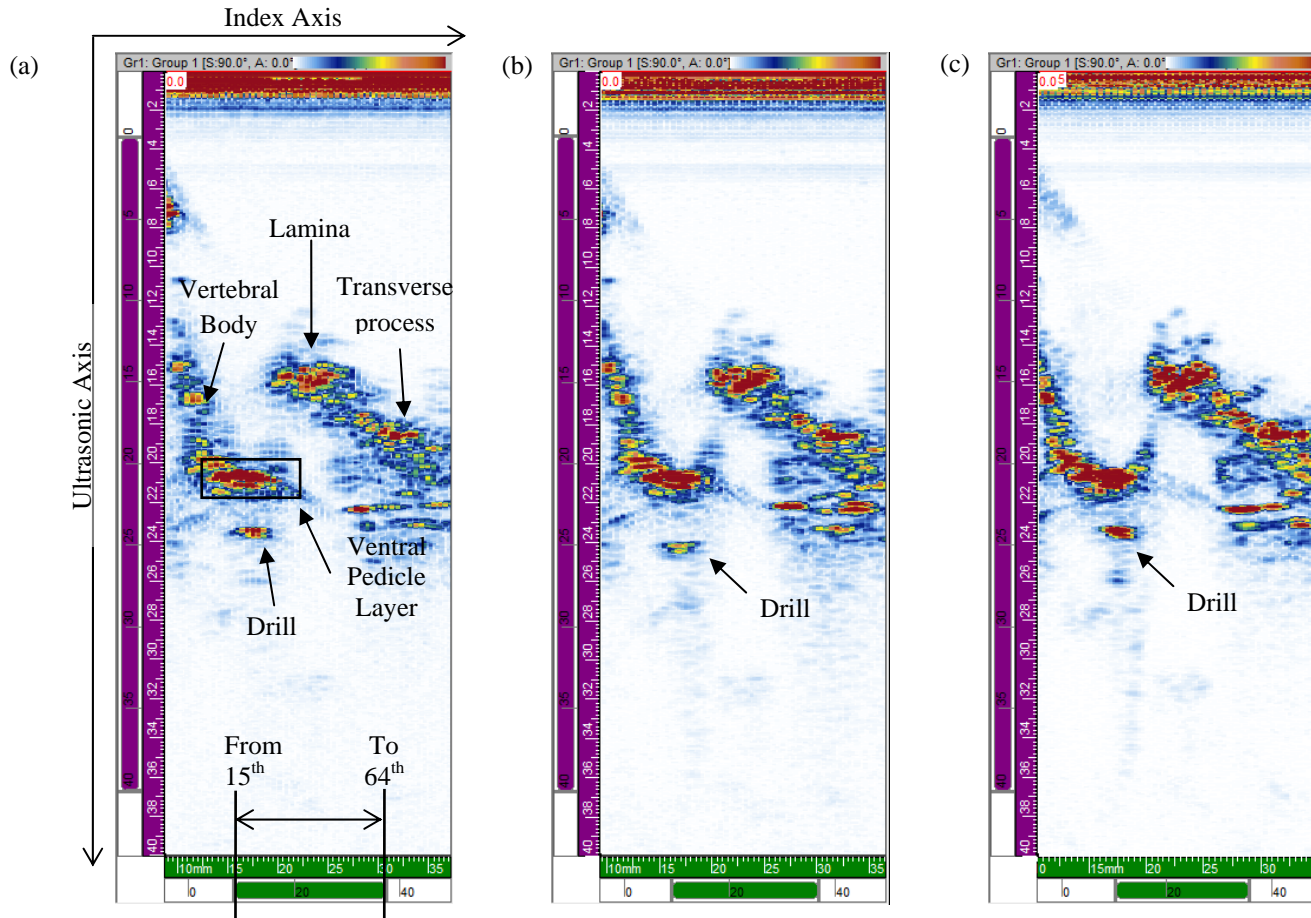
Figure 4-10: Effect of aperture sizes: B-mode color ultrasound images of vertebral bone with drill bit inside the pedicle using an active group of (a) 2 elements, (b) 4 elements, and (c) 8 elements. The acquisitions were performed for the parallel orientation.

than the average height of the pedicle bone. The image can't provide sufficient bone information for the surgeons because of the limited physical coverage and would be under satisfaction. Therefore, a total element number of at least 8 would have a potential to image vertebral bone structure.

4.2.4 The Effect of Steering Beam Angles

To test the effects of steering beam angles on the ultrasound images, all three Configuration I-III were considered.

Figure 4-13 (a)-(e) display the US images with the drill bit inside the pedicle using steering angles of 0^0, 30^0, 60^0, -30^0, and -60^0 for the parallel orientation with a 4-element apertures size and 50 elements used. As discussed in Section 4.3.1, the beam angle of 0^0 in the parallel position setting forms a normal incidence configuration with the pedicle bone. As a result, both the bone signals and the drill bit signal are clearly observable with great intensity, as Figure 4-13 (a) shows. When the ultrasonic beams were steered with an angle of 30^0 towards the direction of lamina bone, the signal from the ventral pedicle bone and drill bit are still detectable (Figure 4-13b), while the signals are distorted. The distortion gets intensified with the increase of steering angle of 60^0 and the intensity of drill bit signal weakens (Figure 4-13c). Similar observations are found with steering angles of -30^0 and -60^0 towards to the vertebral body (Figure 4-13c & d). The leading cause of intensity decrease for the drill bit signals is the ray path reflecting off the bone surface and extra energy loss as a response to the non-normal
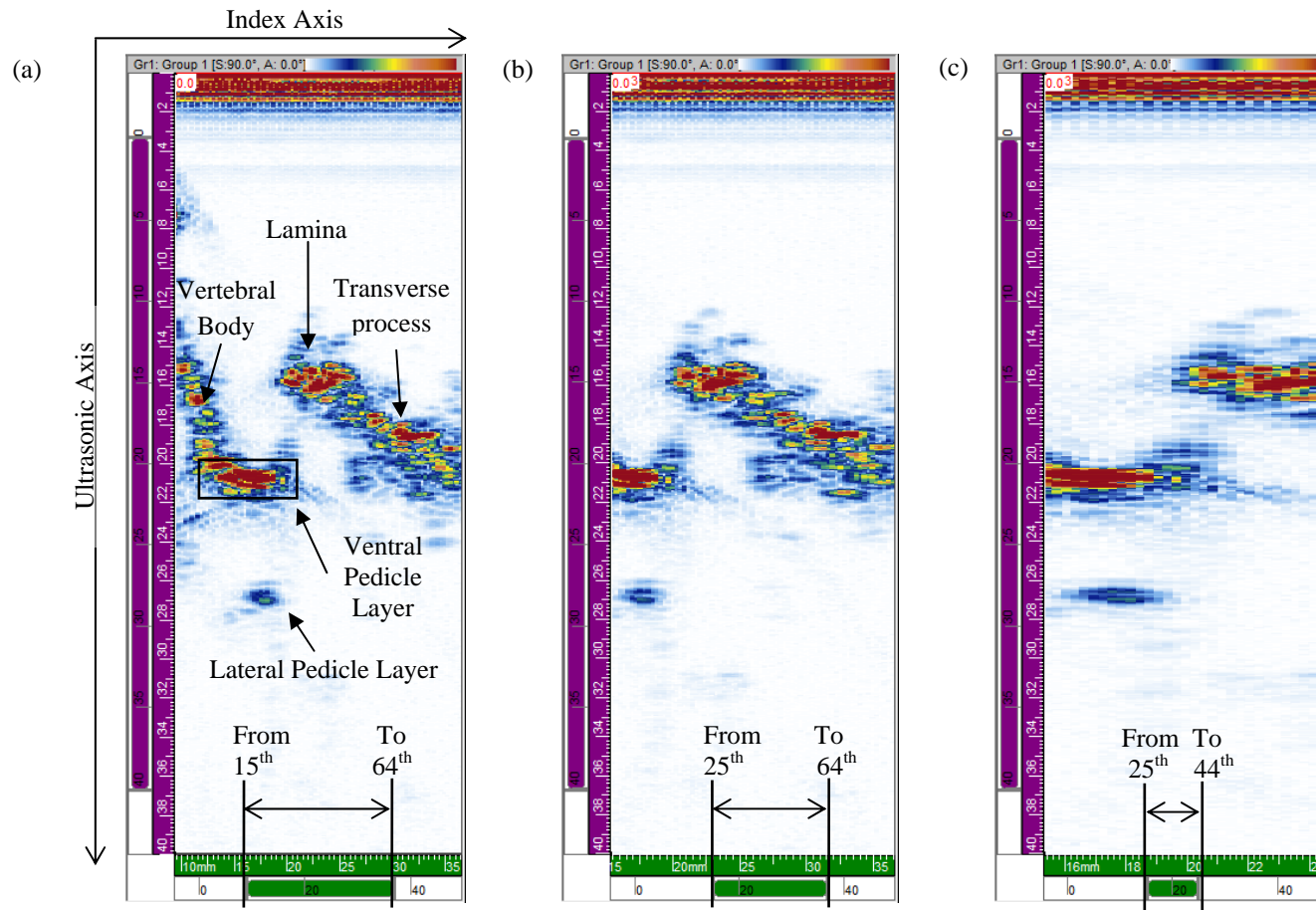
Figure 4-11: Effect of total element used: B-mode color ultrasound images of vertebral bone without drill bit using a total element number of (a) 50, (b) 40, and (c) 20. The acquisitions were performed for the parallel orientation.
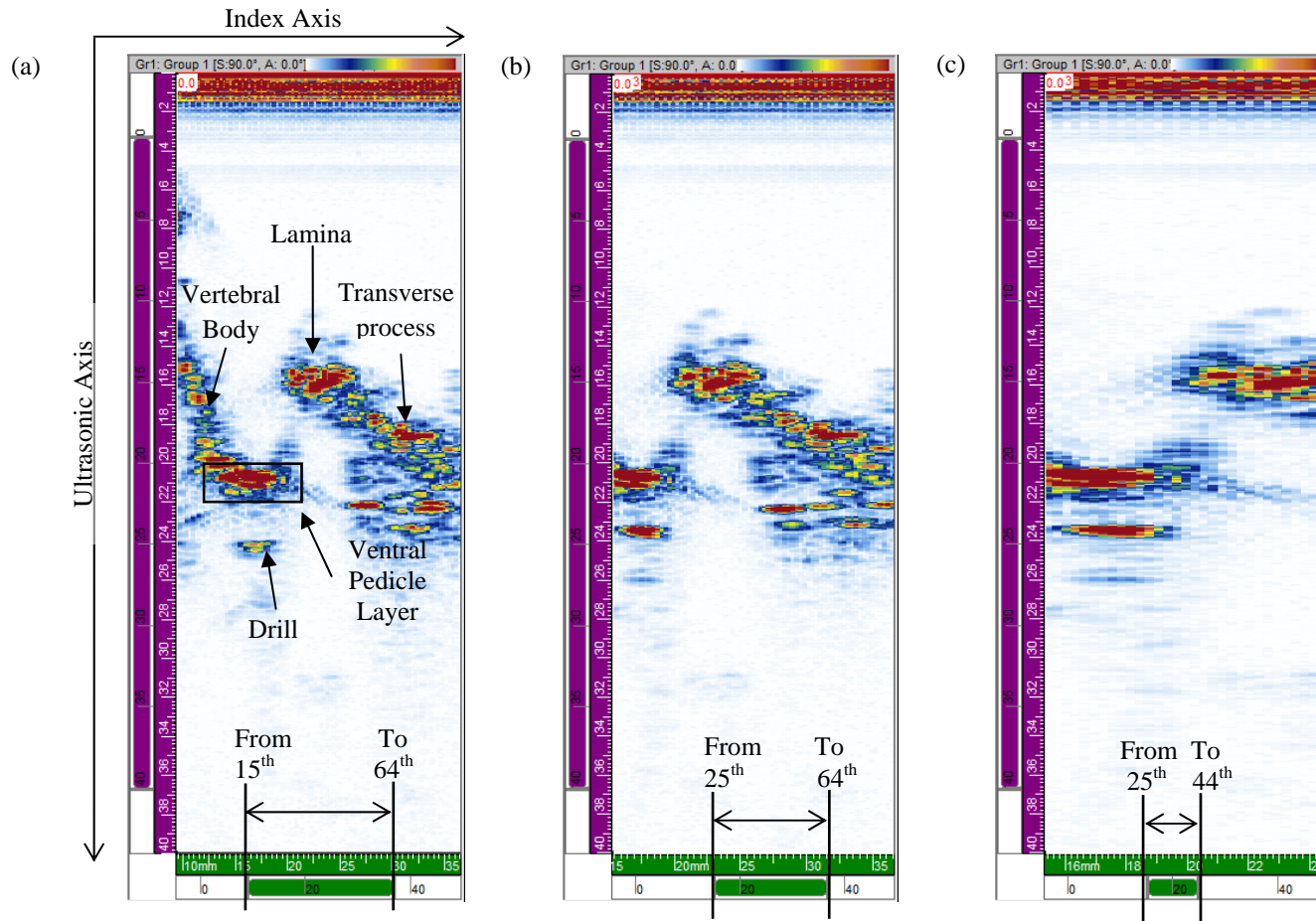
Figure 4-12: Effect of total element used: B-mode color ultrasound images of vertebral bone with drill bit inside the pedicle using a total element number of (a) 50, (b) 40, and (c) 20. The acquisitions were performed for the parallel orientation.

incidence configurations of the ultrasonic beams with the pedicle surface. In addition, another concern that should be noted is the locations of the pedicle bone and drill bit signals in the Figure 4-13 (b)-(e) shifting from the actual position in Figure 4-13 (a). The maximum difference of the pedicle bone signals was measured on Figure 4-13 (a) and (c) and it is up to 11 mm. An alternative method to correct discrepancies caused by non-normal incidence imaging is to attach the transducer with an angled wedge to change the incident angle of the sound beam independently of electronic steering.

Figure 4-14 (a)-(c) displays the bone images with the drill bit inside the pedicle with steering angles of 0^0, 30^0, and 60^0 towards to the left-sided pedicle bone when the transducer was perpendicular to the pedicle bone. Only distorted signals from the vertebral body are detected in Figure 4-14. The pedicle bone and inserting metal drill bit fail to be imaged. Besides, the medial-penetration-mimicking testing was conducted following the prior experiments by positioning the drill bit contact to the ventral pedicle bone. The same steering beam configurations were applied to produce the images. Unfortunately, the drill bit signals are not detected. The attempt to reach the objects of interest by steering beam angles ends unsuccessfully. This conclusion implies that a perpendicular position of the transducer's surface with pedicle bone might not be applicable for the drill bit insertion guidance since.

Figure 4-15 (a)-(c) display the bone images with the drill bit inside the pedicle with steering angles of 0^0, 30^0, 60^0, -30^0, and -60^0 when the transducer was aligned 45^0 toward the pedicle bone. Like the observations in the perpendicular

position testing, the pedicle bone and drill bit signals are not identifiable. Nevertheless, when the drill bit was put contact to the ventral pedicle layer, the reflections from the signal are detected at the steering angles of 0^0 and $30^{0,}$ as Figure 4-16 (a) and (b) show. When the beam angles are greater than 30^0 or less than 0^0, the drill bit signals can't be captured (Figure 4-16 c–e).

4.3   Conclusions

This chapter presents some preliminary results of imaging an inserted steel bit within the pedicle bone using a phased array TomoScan scanner with a 64-element transducer array. Only one sample was investigated in the experiment. We considered three orientations of the array with respect to the bone sample and also studied the effect of aperture size, total element number, and the beam steering on the US images. Among the three orientations, the parallel orientation provided the best B-mode US images with better coverage and resolution to visualize the bone structure and the inserted bit. Both the perpendicular and 45^0 orientations failed to image the pedicle bone and the steel bit even when the beam was steered.   However, the 45^0 orientation was able to capture the steel bit signal when it was located outside the ventral pedicle bone, indicating a potential application to monitor and avoid medial drill bit penetration into the spinal cord. The aperture experiment showed that the aperture size would enhance the signal intensity but decrease the lateral resolution of the US beam. An aperture composed of not less than 4 elements is able to generate desirable images with sufficient signal intensity. The total element number affects the physical coverage
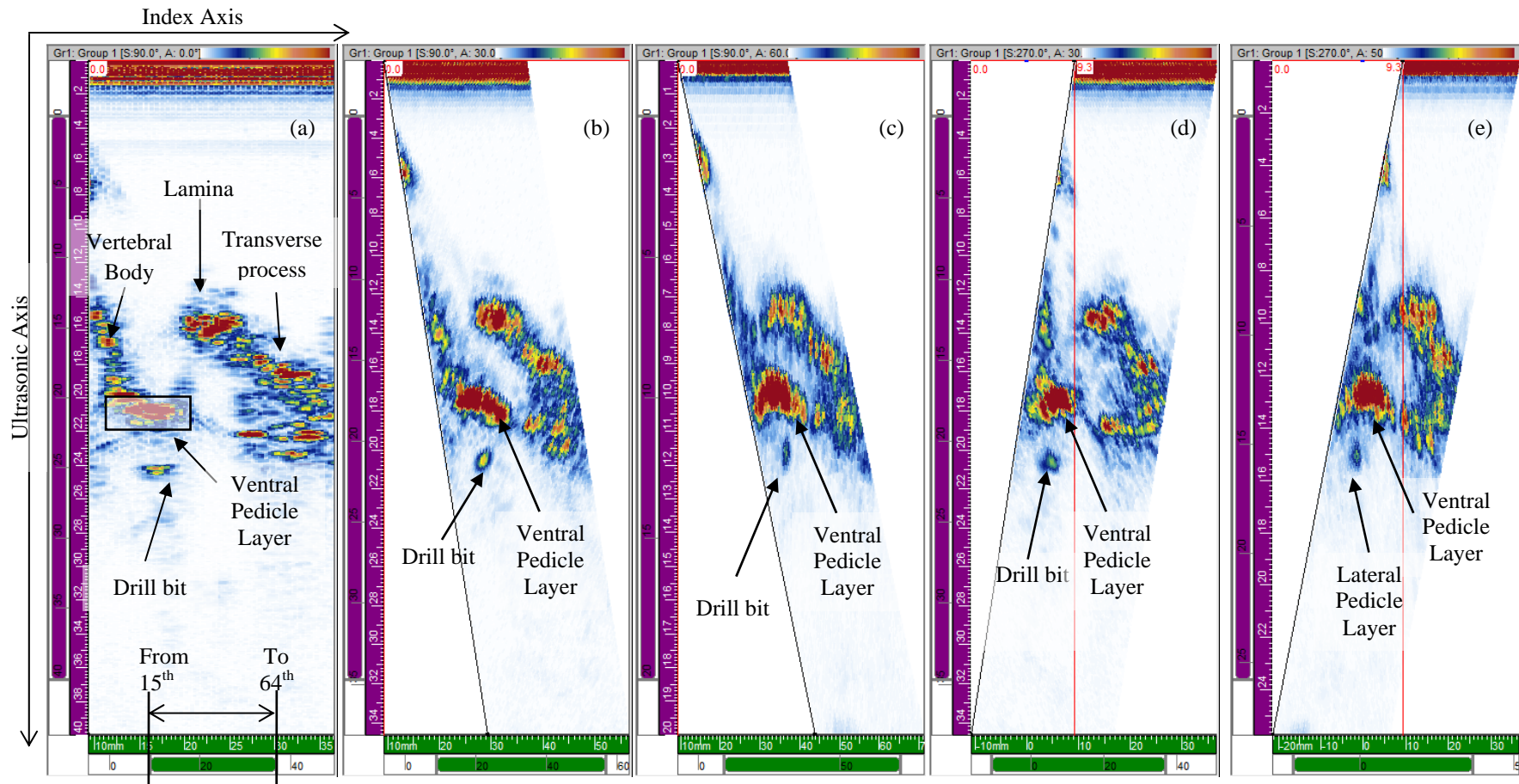
Figure 4-13: Effect of beam steering angle: B-mode color ultrasound images of vertebral bone with drill bit inside the pedicle using beam steering angle of (a)0^0, (b) 30^0, (c) 60^0, (d) -30^0, and (e) -60^0. The acquisitions were performed for the parallel orientation.
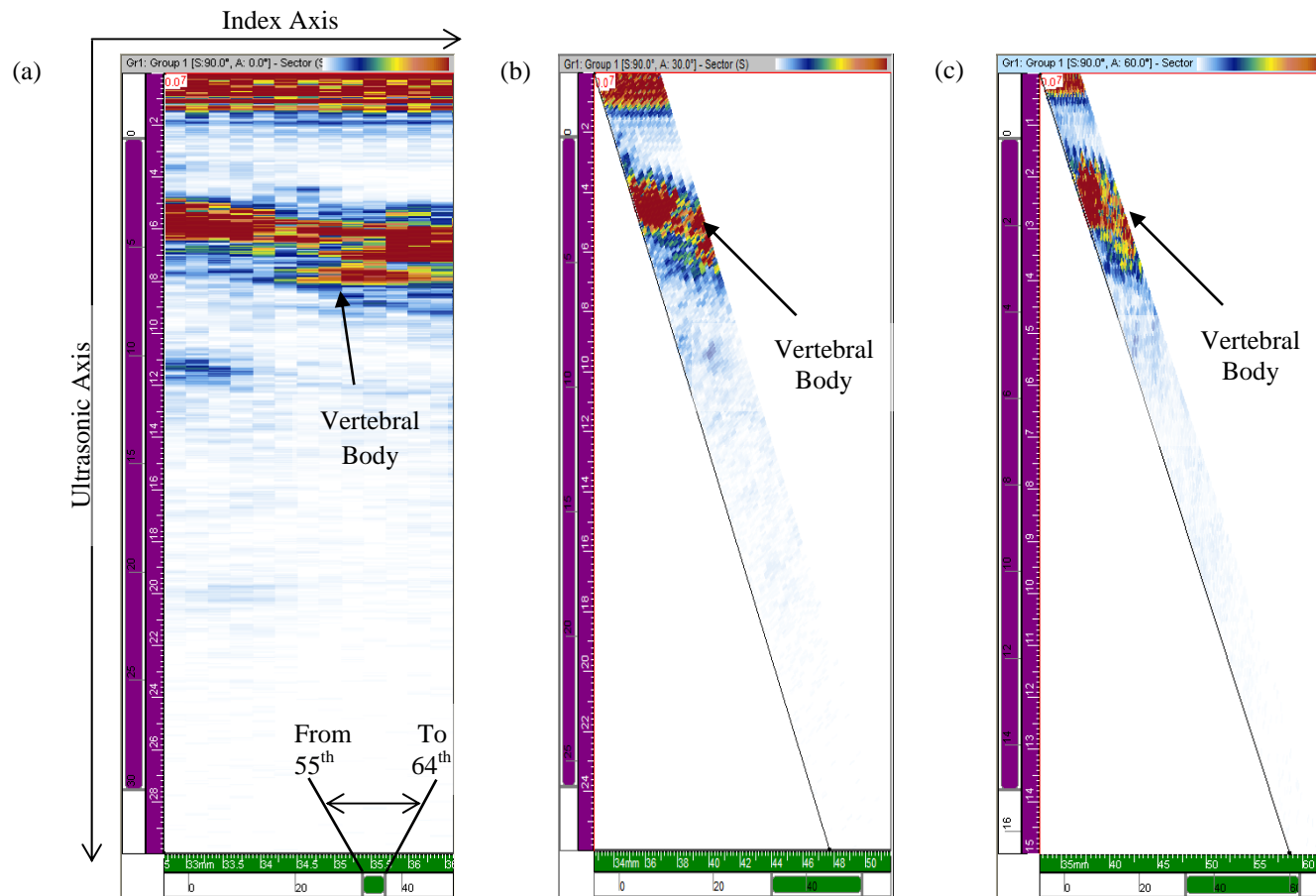
Figure 4-14: Effect of beam steering angle: B-mode color ultrasound images of vertebral bone with drill bit inside the pedicle using beam steering angle of (a) 0^0, (b) 30^0, and (c) 60^0. The acquisitions were performed for the perpendicular orientation.
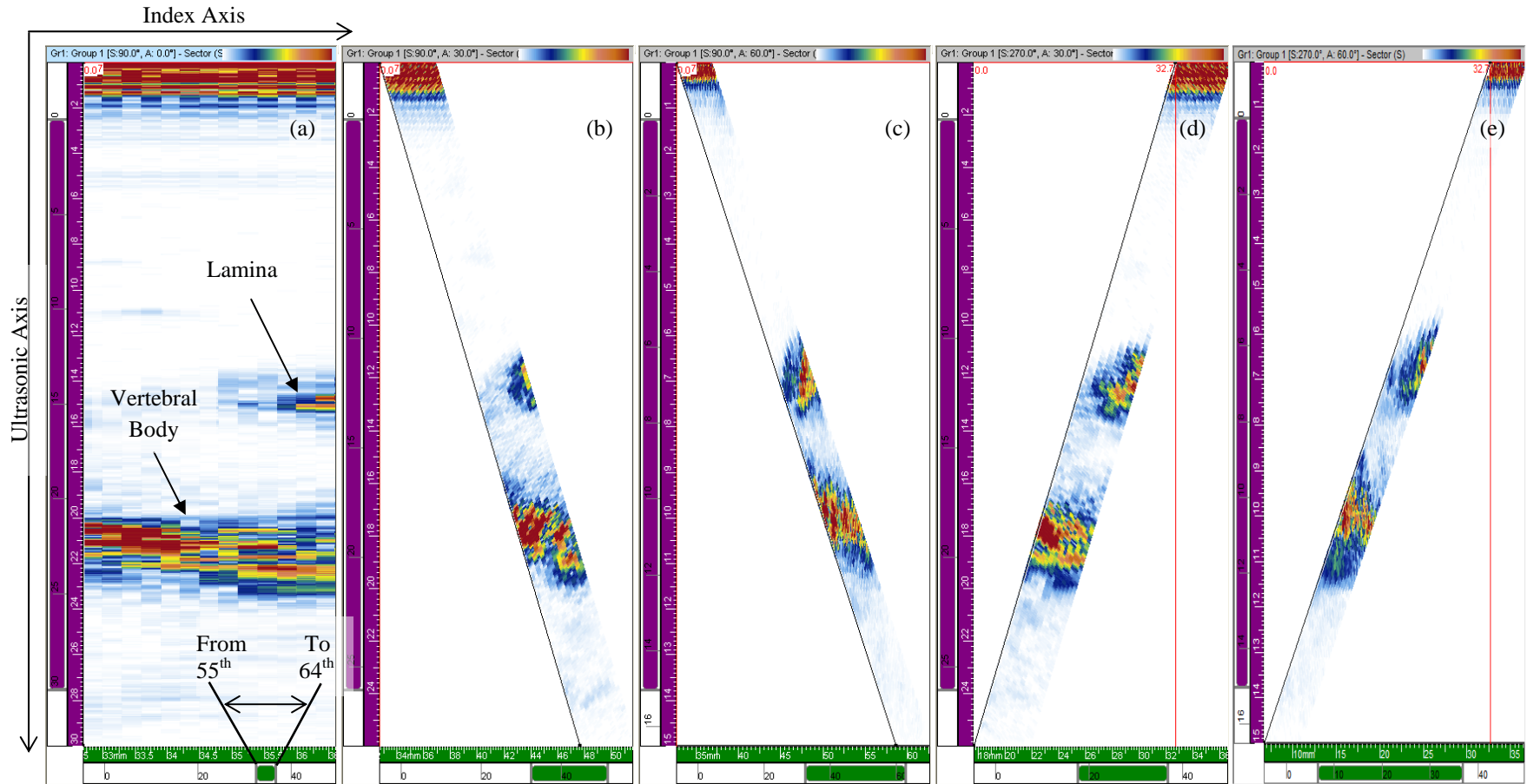
Figure 4-15: Effect of beam steering angle: B-mode color ultrasound images of vertebral bone with drill bit inside the pedicle using beam steering angle of (a) 0^0, (b)30^0, (c) 60^0, (d) -30^0, and (e) -60^0. The acquisitions were performed for the 45^0 orientation.
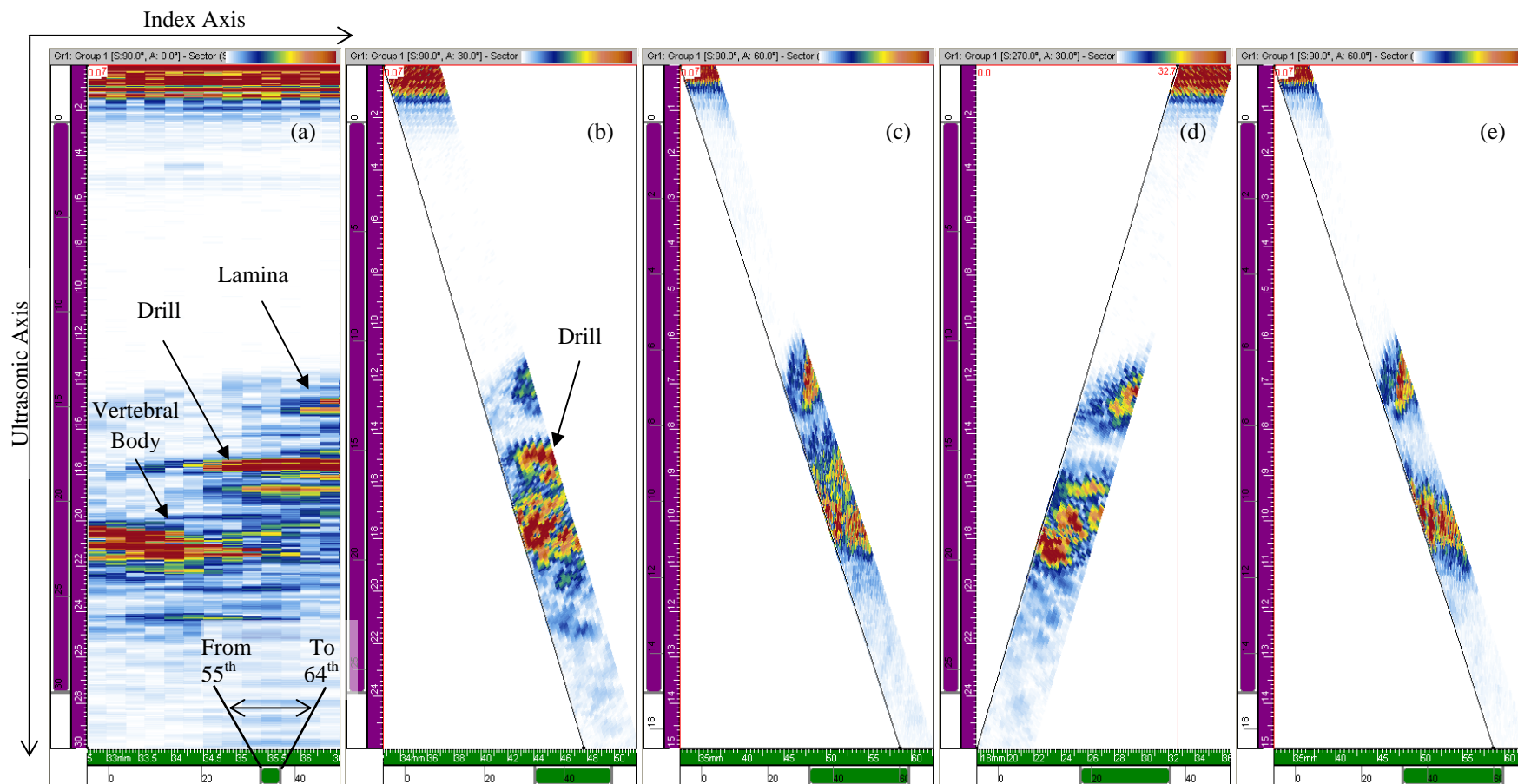
Figure 4-16: Effect of beam steering angle: B-mode color ultrasound images of vertebral bone with drill bit contact to the pedicle using beam steering angle of (a) 0^0, (b) 30^0, (c) 60^0, (d) -30^0, and (e) -60^0. The acquisitions were performed for the 45^0 orientation.

area of the sample. A transducer containing at least 8 elements is suggested for vertebral bone imaging.

Based on the experimental observations, we concluded that the size and placement of the transducer plays a critical role in imaging vertebral pedicle. A miniature transducer composed of at least 8 elements will resolve the placement problem but the resolution remains to be justified. The results here are very preliminary and further experiments with more bone samples are required to provide some affirmative conclusions.

Chapter 5

Conclusion

This thesis describes a feasibility study to investigate an innovative ultrasound imaging guidance method for pedicle screw instrumentation involved in scoliosis surgery based on the principle of ultrasonic pulse-echo theory. The method utilizes an ultrasound linear phased array to emit focused ultrasonic signals to the vertebral pedicle bone, receive reflected echoes from the boundaries of pedicle bone and inserted screw, and then form bone images by detecting the boundaries. The method has the following desirable advantages: (1) radiation free, (2) real-time imaging, (3) portability, and (4) cost effectiveness. The hypothesis that US guided screw insertion for scoliosis surgery is a viable clinical tool has been proven.

This chapter highlights the major contributions of the thesis and suggests future work.

5.1 Overall Achievement

A review of literature (Chapter 2) described the historical background of scoliosis surgery, discussed serious surgical complications, the limitation of current imaging guidance methods, and the requirements to develop a new radiation-free imaging guidance method. This thesis investigated the practical requirements

needed to develop a real-time imaging guidance method using ultrasound pulse echo techniques that is radiation free, cost effective and portable.

First, the acoustic properties (velocity and attenuation) of vertebral cortical and cancellous bones were characterized for use in the quantitative identification of bone signals from B-mode ultrasound images. These preliminary investigations provided the fundamental framework for the application of linear phased array imaging by validating optimal frequencies, estimating the accuracy of the ultrasound method, and effects of cancellous bone (Chapter 3). Secondly, the feasibility of the TomoScan scanner in vertebral bone imaging was investigated. The characterized ultrasonic equipment was used to perform the tests on a vertebral specimen of porcine spine for the validation of transducer locations, and assessment of transducer configurations (active aperture, total element number, and steering beam angles) (Chapter 4).

5.2 Major Contributions

The major objectives that were achieved are:

(1)   Acoustic property characterization of vertebral bone – a framework was developed for ultrasound bone imaging by analyzing the acoustic properties (velocities, attenuations, nBUA) of both cortical bone and cancellous bone together with their response to frequency.

(2)   Preliminary analysis of ultrasound bone/screw image – this work presents a procedure for producing 2D ultrasound bone/screw images using immersion ultrasonic pulse-echo technique. It also provides the measuring accuracy and

(3)   Application of TomoScan scanner in bone imaging – this project applied the characterized equipment to a porcine vertebral model. The transducer locations and effect of transducer configurations (active aperture, total element number and steering beam) were investigated and discussed. The feasibility of the proposed linear phased array method for vertebral pedicle bone/screw imaging was preliminarily verified, which suggests the potential application of the linear phased array method in scoliosis surgery guidance by providing bone/screw images.

5.3 Suggested Future Work

This work presents a feasibility study for use US to image vertebral pedicle bone and inserted screw. Suggested future work based on this our results includes:

(1)   To better appreciate the acoustic properties of vertebral bone presented in this thesis, more animal bone samples (at least six) from various spinal locations should be prepared to repeat acoustic testing. Statistical analysis should be performed.

(2)   Applying a miniature linear phased array on pedicle bone imaging: A miniature linear phased array should be specially designed to fit the dimension of vertebral bone and experiments should be done on at least six vertebral specimens. The vertebral samples should be from various spinal levels with various sizes and the test should be performed before and after

screw insertion. To further study the feasibility of the ultrasound imaging guidance method for real-time screw insertion, a simulation of scoliosis surgery should be performed by monitoring the whole insertion process of a pedicle screw into the pedicle bone using the TomoScan scanner. Bone perforation (medial & lateral) tests are strongly suggested. The reproducibility of the ultrasound method should be determined.

(3)   Improving the ultrasound image quality. Appendix C presents the limitations of the commercial system with affiliated software that affect the image quality (such as the TGC and color-coding methods). Improvements can be achieved by exporting the raw data from the TomoScan scanner, and then signal/image processing methods can be applied to enhance the signal intensity and resolution.

(4)   Cadaver and clinical studies: after animal experiments, the method should be applied to cadavers (with the approval of the ethics committee of the University of Alberta). If successful, clinical control trials should be designed and conducted at the Stollery Children's Hospital to prove the guiding efficacy of the ultrasonic imaging system during surgical operations. Several factors to be studied statistically include the ultrasound image quality, the accuracy of screw placement, the training time required to operate the equipment, and the inconvenience and complexity added to the surgery. Based on these preliminary trials, the equipment and methodology would be improved.

REFERENCES

Amiot, L. P., Labelle, H., DeGuise, J. A. P., Sati, M. B., brodeur, P. M., and Rivard, C. H. (1995). "Computer-assisted pedicle screw fixation- A feasibility study," Spine 20, 1208-1212.

Arand, M., Hartwig, E., Kinzl, L., and Gebhard, F. (2001). "Spinal navigation in cervical fractures: Preliminary clinical study on Judet-Osteosynthesis of the axis," Computer Aided Surgery 6, 170 - 175.

Asher, M., Lai, S. M. P., Burton, D., Manna, B. R. N., and Cooper, A. (2004). "Safety and efficacy of Isola instrumentation and arthrodesis for adolescent idiopathic scoliosis: Two- to 12-Year follow-up," Spine 29, 2013-2023.

Axenovich, T. I., Zaidman, A. M., Zorkoltseva, I. V., Tregubova, I. L., and Borodin, P. M. (1999). "Segregation analysis of idiopathic scoliosis: demonstration of a major gene effect," American Journal of Medical Genetics 86:389–394.

Barr, S. J., Schuette, A. M., and Emans, J. B. (1997). "Lumbar pedicle screws versus hooks. Results in double major curves in adolescent idiopathic scoliosis," Spine 22, 1369-1379.

Barratt, D. C., Penney, G. P., Chan, C. S. K., Slomczykowski, M., Carter, T. J., Edwards, P. J., and Hawkes, D. J. (2006). "Self-calibrating 3D-ultrasound-based bone registration for minimally invasive orthopedic surgery," Medical Imaging, IEEE Transactions on 25, 312-323.

Bauer, D. C., Gluer, C. C., Cauley, J. A., Vogt, T. M., Ensrud, K. E., Genant, H. K., and Black, D. M. (1997). "Broadband ultrasound attenuation predicts fractures strongly and independently of densitometry in older women. A prospective study. Study of Osteoporotic Fractures Research Group," Archives of Internal Medicine 157(6):629-634.

Belmont, P. J. J., Klemme, W. R., Dhawan, A., and Polly, D. W. J. (2001). "In vivo accuracy of thoracic pedicle screws," Spine 26, 2340-2346.

Bradford, D. S., Tay, B. K., and Hu, S. S. (1999). "Adult scoliosis: Surgical indications, operative management, complications, and outcomes," Spine 24, 2617-2629.

Chaffai,S., Padilla, F., Berger, G., and Laugier, P. (2000). "In vitro measurement of the frequency-dependent attenuation in cancellous bone between 0.2 and 2 MHz, " The Journal of the Acoustical Society of America 108(3):1281-1289.

Choi, W. W., Green, B. A., and Levi, A. D. O. (2000). "Computer-assisted fluoroscopic targeting system for pedicle screw insertion," Neurosurgery 47, 872-878.

Cobb, J. (1948). "Outline for the study of scoliosis," AOS Instructional Course Lecture 5:261–275.

Cobbold, R. S. C. (2008). *Foundations of Biomedical Ultrasound* (Oxford University Press, New York), Chap. 1, pp. 77.

Dolan, L. A., and Weinstein, S. L. (2007) "Surgical rates after observation and bracing for adolescent idiopathic scoliosis," Spine 32:S91-S100.

Dolan, L. A., Donnelly, M. J., Spratt, K. F., and Weinstein, S. L. (2007). "Professional opinion concerning the effectiveness of bracing relative to observation in adolescent idiopathic scoliosis," Journal of Pediatric Orthopaedics 27, 270-276.

Droin, P., Berger, G., Laugier, P. (1998). "Velocity dispersion of acoustic waves in cancellous bone, " Ultrasonics, Ferroelectrics and Frequency Control, IEEE Transactions on 45(3):581-592.

Foley, K. T., Simon, D. A. P., and Rampersaud, Y. R. (2001). "Virtual fluoroscopy: Computer-assisted fluoroscopic navigation," Spine 26, 347-351.

Gao, X., Gordon, D., Zhang, D., Browne, R., Helms, C., Gillum, J., Weber, S., Devroy, S., Swaney, S., Dobbs, M., Morcuende, J., Sheffield, V., Lovett, M., Bowcock, A., Herring, J., and Wise, C. (2007). "CHD7 Gene polymorphisms are associated with susceptibility to idiopathic scoliosis," American Journal of Human Genetics 80 (5): 957-965.

Geerling, J., Kendoff, D., Citak, M., Gösling, A., Gösling, T., Krettek, C., and Hüfner, T. (2007). "Navigated pedicle screw placement in lumbar spine fusion surgery," in Navigation and MIS in Orthopedic Surgery, pp. 540-546.

Gibson, J. L., and Ashby, F. M. (1999). *Cellular Solids* (Cambridge University Press, London, UK), pp. 429-452.

Goethem, J. W. M., and Campenhout, A. (2007). "Scoliosis," *in Spinal Imaging* (Springer Berlin Heidelberg), Chap. 4, pp. 95-108.

Goldberg, C., Moore, D., Fogarty, E., and Dowling, F. (2008). "Scoliosis: a review," Pediatric Surgery International 24, 129-144.

Goodsitt, M. M., Carson, P. L., Witt, S., Hykes, D. L., James, M., and Kofler, J. (1998). "Real-time B-mode ultrasound quality control test procedures. A report of AAPM ultrasound task group No. 1. ," Medical Physics 125(8):22.

Guo, X., Chau, W.W., Chan, Y. L., and Cheng, J. C. (2003). "Relative anterior spinal overgrowth in adolescent idiopathic scoliosis. Results of disproportionate endochondral-membranous bone growth," Journal of Bone and Joint Surgery, British Volume 85:1026–1031.

Haefeli, M., and Min, K. (2008). "Idiopathic scoliosis," *in Spinal Disorders and Malformations* (Springer Berlin Heidelberg), Chap. 23, pp. 623-662.

Hans, D., Schott, A. M., Meunier, P. J. (1993). "Ultrasonic assessment of bone: a review, " European Journal of Medicine 2(3):157-163.

Harrington, P. R. (1962). "Treatment of scoliosis. Correction and internal fixation by spine instrumentation," The Journal of Bone and Joint Surgery 44-A, 591-610.

Holly, L. T., and Foley, K. T. (2003). "Three-dimensional fluoroscopy-guided percutaneous thoracolumbar pedicle screw placement," Journal of Neurosurgery 99, 324-329.

Hott, J. S., Deshmukh, V. R., Klopfenstein, J. D., Sonntag, V. K., Dickman, C. A., Spetzler, R. F., and Papadopoulos, S. M. (2004). "Intraoperative Iso-C C-arm

navigation in craniospinal surgery: the first 60 cases," Neurosurgery 54, 1131-1137.

Ito, Y., Sugimoto, Y., Tomioka, M., Hasegawa, Y., Nakago, K., and Yagata, Y. (2008). "Clinical accuracy of 3D fluoroscopy-assisted cervical pedicle screw insertion," Journal of Neurosurgery: Spine 9, 450-453.

Karatoprak, O., Unay, K., Tezer, M., Ozturk, C., Aydogan, M., and Mirzanli, C. (2008). "Comparative analysis of pedicle screw versus hybrid instrumentation in adolescent idiopathic scoliosis surgery," International Orthopaedics 32, 523- 529.

Kantelhardt, S. R., Bock, C. H., Larsen, J., Bockermann, V., Schillinger, W., Rohde, V., and Giese, A. (2009). "Intraosseous ultrasound in the placement of pedicle screws in the lumbar spine," Spine 34, 400-407.

Kaye, G. W. C., and Laby, W. C. (1973). *Table of Physical and Chemical Constants* (Longman, London, UK).

Kim, Y. J., Lenke, L. G., Bridwell, K. H., Cho, Y. S. S., and Riew, K. D. (2004). "Free hand pedicle screw placement in the thoracic spine: Is it safe?, " Spine 29:333-42.

Kim, Y. J., Lenke, L. G., Bridwell, K. H., Kim, K. L., and Steger-May, K. (2005). "Pulmonary function in adolescent idiopathic scoliosis relative to the surgical procedure," The Journal of Bone and Joint Surgery 87, 1534-1541.

King, H. A., Moe, J. H., Bradford, D. S., and Winter, R. B. (1983). "The selection of fusion levels in thoracic idiopathic scoliosis," The Journal of Bone and Joint Surgery 65:1302–1313.

Kuklo, T. R., Potter, B. K., and Lenke, L.G. (2005). "Vertebral rotation and thoracic torsion in adolescent idiopathic scoliosis: What is the best radiographic correlate?," Journal of Spinal Disorders and Techniques 18(2):139–147.

Laine, T., Lund, T., Ylikoski, M., Lohikoski, J., and Schlenzka, D. (2000). "Accuracy of pedicle screw insertion with and without computer assistance: a randomised controlled clinical study in 100 consecutive patients," European Spine Journal 9, 235-240.

Lam, G., Hill, D., Le, L., Raso, J., and Lou, E. (2008). "Vertebral rotation measurement: a summary and comparison of common radiographic and CT methods," Scoliosis 3, 16.

Langton, C. M., Palmer, S. B., Porter, R. W. (1984). "The measurement of broadband ultrasonic attenuation in cancellous bone," ARCHIVE: Engineering in Medicine 13(2):89-91.

Langton, C. M., Njeh, C. F., Hodgskinson, R., and Carrey J. D. (1996). "Prediction of mechanical properties of the human calcaneus by broadband ultrasonic attenuation," Bone 18:495-503.

Laporte, S., Mitton, D., Ismael, B., de Fouchecour, M., Lasseau, J., Lavaste, F., and Skalli, W. (2000). "Quantitative morphometric study of thoracic spine

A preliminary parameters statistical analysis," European Journal of Orthopaedic Surgery & Traumatology 10, 85-91.

Lasaygues, P., Lefebvre, J. P., Mensah, S. (1997). "High resolution low frequency ultrasonic tomography, " Ultrasound Imaging 19(4):278-293.

Lasaygues, P., Ouedraogo, E., Lefebvre, J. P., Gindre, M., Talmant, M., Laugier, P. (2005). "Progress towards in vitro quantitative imaging of human femur using compound quantitative ultrasonic tomography," Physics in Medicine and Biology 50(11):2633-2649.

Lasaygues, P. (2006). "Assessing the cortical thickness of long bone shafts in children, using two-dimensional ultrasonic diffraction tomography," Ultrasound Medicine and Biology 32(8):1215-1227.

Laugier, P., Giat, P., and Berger G. (1994). "Broadband ultrasonic attenuation imaging: A new imaging technique of the os calcis, " Calcified Tissue International, 54 (2): 83-86.

Laugier, P., Wear, K. A., and Waters, K. R. (2008). "Introduction to the special issue on diagnostic and therapeutic applications of ultrasound in bone - Part I," Ultrasonics, Ferroelectrics and Frequency Control, IEEE Transactions on 55, 1177-1178.

Laugier, P. (2008). "Instrumentation for in vivo ultrasonic characterization of bone strength," Ultrasonics, Ferroelectrics and Frequency Control, IEEE Transactions on; 55: 1179-96.

Le, L. H. (1998). "An investigation of pulse-timing techniques for broadband ultrasonic velocity determination in cancellous bone: a simulation study," Physics in Medicine and Biology 43: 2295-2308.

Le, L. H., Zhang, C., Ta, D., and Lou, E. (2010a). "Measurement of tortuosity in aluminum foams using airborne ultrasound," Ultrasonics 50(1):1-5.

Le, L. H., Gu, Y.J., Li, Y., and Zhang, C. (2010b). "Probing long bones with ultrasonic body waves," Applied Physics Letters 96(11):114102-114103.

Lenke, L. G., Bridwell, K. H., Baldus, C., Blanke, K., and Schoenecker, P. L. (1993). "Ability of Cotrel-Dubousset instrumentation to preserve distal lumbar motion segments in adolescent idiopathic scoliosis," Journal of Spinal Disorders 6, 339-350.

Lenke, L. G., Betz, R. R., Harms, J., Bridwell, K. H., Clements, D. H., Lowe, T. G., and Blanke, K. (2001). "Adolescent Idiopathic Scoliosis," Journal of Bone and Joint Surgery, 83, 1169-1181.

Lenssinck, M. L., Frijlink, A. C., Berger, M. Y., Bierman-Zeinstra, S. M., Verkerk, K., and Verhagen, A. P. (2005). "Effect of bracing and other conservative interventions in the treatment of idiopathic scoliosis in adolescents: a systematic review of clinical trials," Physical Therapy 85, 1329-1339.

Liljenqvist, U. R., Halm, H. F. H., and Link, T. M. (1997). "Pedicle Screw Instrumentation of the Thoracic Spine in Idiopathic Scoliosis," Spine 22, 2239-2245.

Lonstein, J. E. (1994) "Adolescent idiopathic scoliosis," The Lancet 344:1407-12.

Lonstein, J. E. (2006). "Scoliosis: surgical versus nonsurgical treatment," Clinical Orthopaedics and Related Research 443, 248-259.

Maruyama, T., and Takeshita, K. (2008). "Surgical treatment of scoliosis: a review of techniques currently applied," Scoliosis 3, 6.

Merloz, P., Tonetti, J., Pittet, L., Coulomb, M., Lavallee, S., Troccaz, J., Cinquin, P., and Sautot, P. (1998). "Computer-assisted spine surgery," Computer Aided Surgery 3, 297-305.

Mirza, S. K., Wiggins, G. C., Kuntz, C. I. V., York, J. E., Bellabarba, C., Knonodi, M. A., Chapman, J. R., and Shaffrey, C. I. (2003). "Accuracy of thoracic vertebral body screw placement using standard fluoroscopy, fluoroscopic image guidance, and computed tomographic image guidance: A cadaver study," Spine 28, 402-413.

Mujagic, M., Ginsberg, H. J., and Cobbold, R. S. C. (2008). "Development of a method for ultrasound-guided placement of pedicle screws," Ultrasonics, Ferroelectrics and Frequency Control, IEEE Transactions on 55, 1267-1276.

Nash, C. L., Jr., and Moe, J. H. (1969). "A study of vertebral rotation," The Journal of Bone and Joint Surgery 51, 223-229.

Newton, P. O., Upasani, V. V., Lhamby, J., Ugrinow, V. L., Pawelek, J. B., and Bastrom, T. P. (2008). "Surgical treatment of main thoracic scoliosis with thoracoscopic anterior instrumentation. a five-year follow-up study," The Journal of Bone and Joint Surgery 90, 2077-2089.

Niemeyer, T., Bovingloh, A. S., Grieb, S., Schaefer, J., Halm, H., and Kluba, T. (2005). "Low back pain after spinal fusion and Harrington instrumentation for idiopathic scoliosis," International Orthopaedics 29, 47-50.

Nicholson, P. H., Lowet, G., Langton, C. M., Dequeker, J., and Van der Perre, G. (1996). "A comparison of time-domain and frequency-domain approaches to ultrasonic velocity measurement in trabecular bone," Physics in Medicine and Biology 41, 2421-2435.

Njeh, C. F. , Kuo, C. W., Langton, C. M., Atrah, H. I., Boivin, C. M. (1997). "Prediction of human femoral bone strength using ultrasound velocity and BMD: an in vitro study, " Osteoporosis International 7(5):471-477.

Njeh, C.F., Hans, D., Fuerst, T., Gluer, C.C, and Genant, H.K. (1999). *Quantitative Ultrasound: Assessment of Osteoporosis and Bone Status* (Martin Dunitz Ltd, London), Section 1, pp: 1-76.

Noonan, K. J., Weinstein, S. L., Jacobson, W. C., and Dolan, L. A. (1996). "Use of the Milwaukee brace for progressive idiopathic scoliosis," The Journal of Bone and Joint Surgery 78, 557-567.

Olympus NDT. (2004). *Introduction to phased array ultrasonic technology applications: R/D Tech guideline* (Olumpus NDT, USA).

Ortmaier, T., Weiss, H., Dobele, S., and Schreiber, U. (2006). "Experiments on robot-assisted navigated drilling and milling of bones for pedicle screw placement," The International Journal of Medical Robotics + Computer Assisted Surgery: MRCAS 2, 350-363.

Ouedraogo, E., Lasaygues, P., Lefebvre, J. P., Gindre, M., Talmant, M., Laugier, P. (2002). "Contrast and velocity ultrasonic tomography of long bones," Ultrasound Imaging 24(3):139-160.

Perdriolle, R., and Vidal, J. (1981). "A study of scoliotic curve. The importance of extension and vertebral rotation," Revue de chirurgie orthopédique et réparatrice de l'appareil moteur 67, 25-34.

Potter, B. K., Kuklo, T. R., and Lenke, L. G. (2005). "Radiographic outcomes of anterior spinal fusion versus posterior spinal fusion with thoracic pedicle screws for treatment of Lenke Type I adolescent idiopathic scoliosis curves," Spine 30, 859-1866.

Raphael, D. T., Chang, J. H., Zhang, Y. P., Kudija, D., Chen, T. C., and Shung, K. K. (2010). "A-Mode ultrasound guidance for pedicle screw advancement in ovine vertebral bodies," Spine 10 (5):422-432.

Rossman, P., Zagzebski, J., Mesina, C., Sorenson, J., and Mazess, R. (1989). "Comparison of speed of sound and ultrasound attenuation in the os calcis to bone density of radius, femur and lumbar spine," Clinical Physics and Physiological Measurement 10, 353-360.

Roux, C., Fournier, B., Laugier, P., Chappard, C., Kolta, S., Dougados, M., and Berger, G. (1996). "Broadband ultrasound attenuation imaging: a new imaging method in osteoporosis, " Journal of Bone Mineral Research 11(8):1112-1118.

Roy-Camille, R., Saillant, G., and Mazel, C. (1986). "Internal fixation of the lumbar spine with pedicle screw plating," Clinical Orthopaedics and Related Research, 7-17.

Sachse, W., and Pao, Y. H. (1977). "On the determination of phase and group velocities of dispersive waves in solids," Journal of Applied Physics 49, 4320-4327.

Scanlon, V.C., and Sanders, T. (2007). *Essentials of Anatomy and Physiology* (F.A. Davis Company, USA). Chap. 6, PP.106.

Stirling, A. J., Howel, D., Millner, P. A., Sadiq, S., Sharples, D., and Dickson, R. A. (1996). "Late-onset idiopathic scoliosis in children six to fourteen years old - A cross-sectional prevalence study," The Journal of Bone and Joint Surgery, 78A: 1330-1336.

Suk, S. I., Lee, S. M., Chung, E. R., Kim, J. H., and Kim, S. S. (2005). "Selective thoracic fusion with segmental pedicle screw fixation in the treatment of thoracic idiopathic scoliosis: more than 5-year follow-up," Spine 30, 1602-1609.

Suzuki, S., Yamamuro, T., Shikata, J., Shimizu, K., and Iida, H. (1989). "Ultrasound measurement of vertebral rotation in idiopathic scoliosis," Journal of Bone Joint and Surgery 71-B(2):252-255.

Tavakoli, M. B., and Evans, J. A. (1991). "Dependence of the velocity and attenuation of ultrasound in bone on the mineral content," Physics in Medicine and Biology 36, 1529-1537.

Tortora, G.J., and Grabowski, S.T. (2003). *Principles of Anatomy and Physiology (Harper Collins College Publishers, New York). Chap. 6, PP. 147-151.

Vaccaro, A. R., Rizzolo, S. J., Allardyce, T. J., Ramsey, M., Salvo, J., Balderston, R. A., and Cotler, J. M. (1995). "Placement of pedicle screws in the thoracic spine. Part I: Morphometric analysis of the thoracic vertebrae," The Journal of Bone and Joint Surgery 77, 1193-1199.

Vaccaro, A. R., Rizzolo, S. J., Balderston, R. A., Allardyce, T. J., Garfin, S. R., Dolinskas, C., and An, H. S. (1995). "Placement of pedicle screws in the thoracic spine. Part II: An anatomical and radiographic assessment," The Journal of Bone and Joint Surgery 77, 1200-1206.

Verhoef, W. A., Cloostermans, M. J. T. M., and Thijssen, J. M. (1985). "Diffraction and Dispersion Effects on the Estimation of Ultrasound Attenuation and Velocity in Biological Tissues," Biomedical Engineering, IEEE Transaction on BME-32, 521-529.

Wear, K.A. (2001). "Ultrasonic attenuation in human calcaneus from 0.2 to 1.7 MHz," IEEE Transaction on Ultrasound, Ferroelectrical, Frequency Control. 48(2):602-608.

Wear, K. A., Laib, A., Stuber, A. P., and Reynolds, J. C. (2005). "Comparison of measurements of phase velocity in human calcaneus to Biot theory," The Journal of Acoustic Society of America 117, 3319-3324.

Wear, K. A. (2007). "Group velocity, phase velocity, and dispersion in human calcaneus in vivo," The Journal of Acoustic Society of America 121, 2431-2437.

Wear, K. A. (2008). "Mechanisms for attenuation in cancellous-bone-mimicking phantoms," Ultrasonics, Ferroelectrics and Frequency Control, IEEE Transactions on 55, 2418-2425.

Wear, K. A. (2009). "The dependencies of phase velocity and dispersion on volume fraction in cancellous-bone-mimicking phantoms," The Journal of the Acoustical Society of America 125, 1197-1201.

Weber, P. K., Schlegel, J. C., Meiche, J., Peter, L., and Harland, U. (2001). "A system for ultrasound based intraoperative navigation in spine surgery," in Ultrasonics Symposium, 2001 IEEE, pp. 1361-1364 vol.1362.

Weinstein, S. L., Dolan, L. A., Spratt, K. F., Peterson, K. K., Spoonamore, M. J., and Ponseti, I. V. (2003). "Health and function of patients with untreated idiopathic scoliosis - A 50-year natural history study," Journal of the American Medical Association 289:559-67.

Winter, S., Brendel, B., Pechlivanis, I., Schmieder, K., and Igel, C. (2008). "Registration of CT and Intraoperative 3-D Ultrasound Images of the Spine Using Evolutionary and Gradient-Based Methods," Evolutionary Computation, IEEE Transactions on 12, 284-296.

Working Group Classification, Terminology Committee. (2000). "SRS Terminology Committee and Working Group on Spinal Classification Revised Glossary of Terms".

Xu, R., Ebraheim, N. A., Ou, Y., and Yeasting, R. A. P. (1998). "Anatomic Considerations of Pedicle Screw Placement in the Thoracic Spine: Roy-Camille Technique versus Open-Lamina Technique," Spine 23, 1065-1068.

Zheng, R., Sacchi, M. D., Le, L. H. and Lou, E. (2009). "Ultrasounic Imaging of Long Bone," *European Symposium of Ultrasonic* Characterization of Bone (ESUCB).

Zielke, K., and Berthet, A. (1978). "VDS--ventral derotation spondylodesis--preliminary report on 58 cases," Beiträge zur Orthopädie und Traumatologie 25, 85-103.

APPENDIX A

Calculating Uncertainty

A.1 Uncertainty of a Sum or Difference

For two sets of measurements, y_i and z_i with N data points each, the sum or difference of their averages is given by

$$x = \overline{y} \pm \overline{z} \tag{A-1}$$

where $\overline{y}$ and $\overline{z}$ are the average of the corresponding measurements, i.e.

$$\overline{y} = \frac{\sum_i y_i}{N} \text{ and } \overline{x} = \frac{\sum_i x_i}{N} \tag{A-2}$$

The uncertainty δx of x is determined as:

$$\delta x = \delta y \pm \delta z \tag{A-3}$$

where δy and δz are the corresponding uncertainties of y_i and z_i, respectively.

A.2 Uncertainty of a Product or Quotient

If $x = \overline{y} \times \overline{z}$, the uncertainty is given by:

$$\delta x = x \left[\frac{\delta y}{\overline{y}} + \frac{\delta z}{\overline{z}} \right] \tag{A-4}$$

Similarly if $x = \overline{y} \div \overline{z}$, the uncertainty is the same as (A-4).

A.3 Uncertainty of a Log

For a set of N measurement $\log y_i$, the uncertainty is calculated:

$$\delta x = \frac{(\delta y / \overline{y})}{\log(\overline{y})} \tag{A-5}$$

APPENDIX B

Estimating Transmission Loss at the

Cancellous Bone/Water Interface

Consider an interface separated by two media characterized by acoustic impedances Z_1 and Z_2, an ultrasound beam of amplitude A_o is incident in medium 1 upon the interface and is reflected as A_r. The amplitude reflection coefficient R indicating the fraction of the incident wave amplitude that is reflected is

$$R = \frac{A_r}{A_0} = \frac{Z_2 - Z_1}{Z_2 + Z_1} \tag{B-1}$$

In order to derive the reflection coefficient of water/bone interface, we do the following. Firstly, assume an ultrasound beam be incident in water upon a solid aluminum plate. The reflection coefficient $R_{w/al}$ is

$$R_{w/Al} = \frac{A_r}{A_0} = \frac{Z_{Al} - Z_w}{Z_{Al} + Z_w} \tag{B-2}$$

where Z_{Al} and Z_w are the acoustic impedances of aluminum and water, respectively. Secondly, in case the aluminum is replaced by a piece of cancellous bone sample, Equation (B-2) can be written as

$$R_{w/cb} = \frac{\widehat{A}_r}{A_0} = \frac{Z_{cb} - Z_w}{Z_{cb} + Z_w} \tag{B-3}$$

where $\widehat{A}_r$ is the reflected amplitude of the ultrasound beam by the bone/water interface and Z_{cb} is the acoustic impedance of the cancellous bone. Thirdly, eliminating A_o by combining the Equations (B-2) and (B-3), we obtain

$$R_{w/cb} = R_{w/Al} \times \frac{\widehat{A}_r}{A_r} \quad . \tag{B-4}$$

Aluminum and water have acoustic impedances of 17.06 MRayl and 1.48 MRayl respectively, and thus $R_{w/Al}$ is 0.838 according to Equation (B-2). Equation (B-4) can then be written as

$$R_{w/cb} = 0.838 \times \frac{\widehat{A}_r}{A_r} \quad . \tag{B-5}$$

In order to measure $R_{w/cb}$, we set up an experiment to measure A_r and $\widehat{A}_r$. Figure B-1 shows the experimental setup for an immersion pulse-echo experiment. An aluminum plate and the cancellous bone sample were positioned and their faces were parallel to the transducer surface. A focused 3.5 MHz immersion transducer with an active diameter of 6.4 mm was considered (C382, Panametrics-NDT, Waltham, MA). The distance between the transducer and the samples was kept at near field distance of 23.2 mm. One measurement was made for the aluminum plate and ten measurements for the cancellous bone sample by translating the sample discretely 0.5 mm parallel to the transducers' faces while keeping the main ultrasound beam within the sample's boundaries.
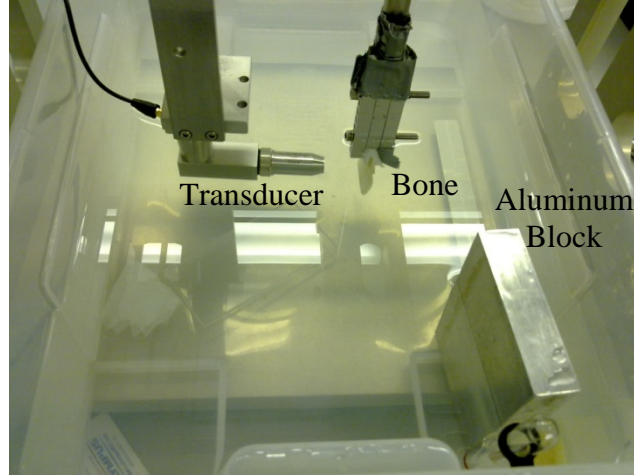
Figure B-1: The setup for immersion pulse-echo experiments.

Figure B-2 displays examples of the ultrasonic reflected signals from the aluminum plate and cancellous bone, respectively. The dash lines indicate the signal envelop which was obtained by means of Hilbert transform (Le, 1998). $\hat{A}_r$ and $\hat{A}_r$ were chosen to be the envelope peaks of the reflected signals from the aluminum plate and cancellous bone, and they are 0.3 volts and 0.0508± 0.0133 volts respectively. According to Equation (B-5), the reflection coefficient $R_{w/cb}$ was estimated to be 14.19% ±3.72%.

The transmission loss for water/ bone interface $T_{w/cb}$ is given by definition,

$$T_{w/cb} = \sqrt{1 - R_{w/cb}^2} \qquad (\text{B-6})$$

Similarly, the transmission loss for bone/water interface $T_{cb/w}$ is

$$T_{cb/w} = \sqrt{1 - R_{cb/w}^2} = \sqrt{1 - R_{w/cb}^2} \qquad (\text{B-7})$$

where

$$R_{w/cb} = -R_{cb/w} \qquad (\text{B-8})$$

according to equation (B-3). Thus the transmitted amplitude through the bone sample due to the partition of energy at the interfaces only can be approximated by

$$
\begin{aligned}
T_{w/cb}T_{cb/w} &\approx 1 - R_{w/cb}^2 \\
&\approx \frac{4Z_{cb}Z_w}{(Z_{cb} + Z_w)^2}
\end{aligned}
\tag{B-9}
$$

which is about 97.99 %±7.44%.

The transmission loss is quantified in *dB/cm* by

$$
T_{loss}(dB/cm) = 20 \times \frac{1}{L} \log_{10}\left(T_{w/cb}T_{cb/w}\right)
\tag{B-10}
$$

which is about -0.4±0.17 dB/cm.
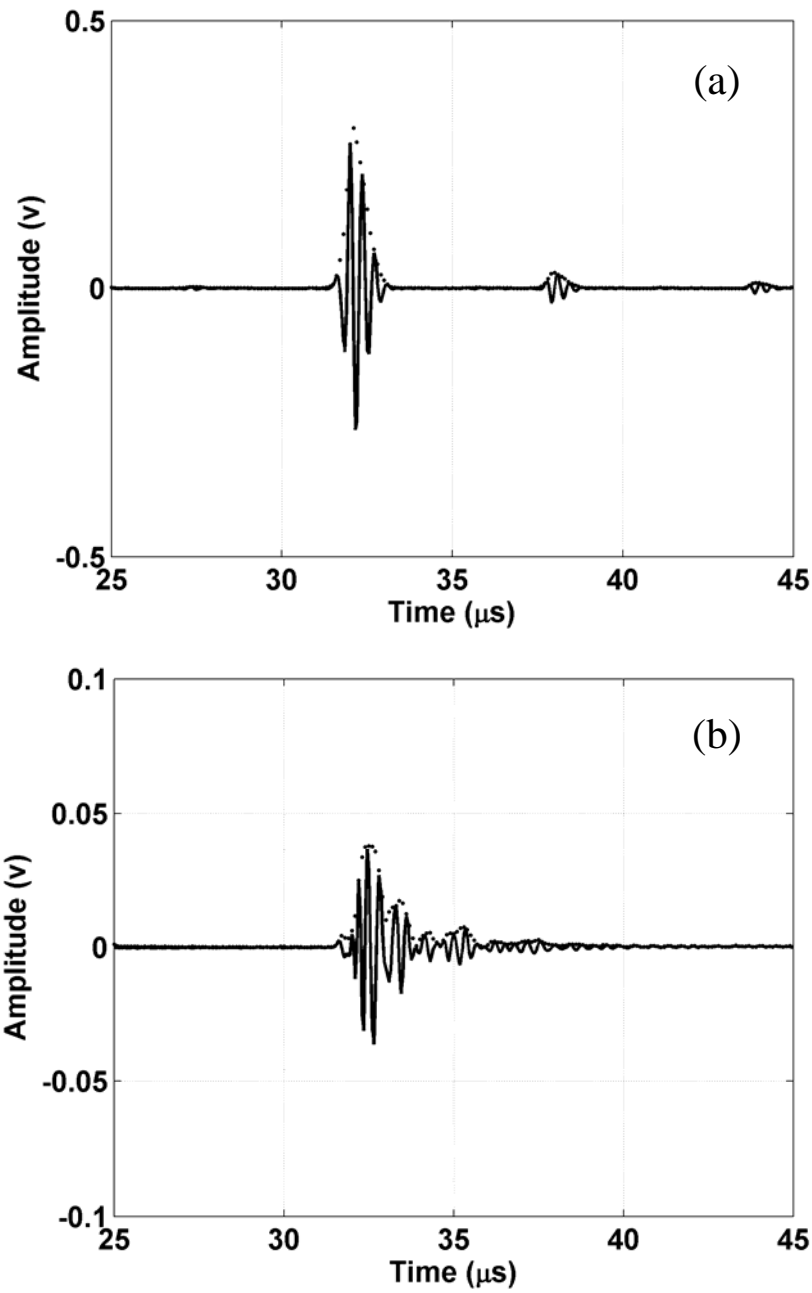
Figure B-2: Examples of the ultrasonic reflection signals of (a) the aluminum plate, and (b) cancellous bone. The dash lines represent signal envelops.

APPENDIX C

Performance Evaluation of the TomoScan Ultrasound Scanner

Most of the current bone studies obtain series of raw data from a digital oscilloscope by moving a single-element transducer excited by a pulser/receiver (Le *et al.*, 2010a, b; Mujagic *et al.*, 2008; Wear 2005, 2006, 2007, 2008, 2009). To advance the bone imaging investigation, several studies were carried out with the aid of commercially available medical ultrasound equipments because this equipment is capable of providing multiple acquisition channels and can visualize two dimensional (2D) images in real time (Suzuki *et al.,* 1989; Barratt *et al.,* 2006; Winter *et al.,* 2008; Kantelhardt *et al.,* 2009). However, the signal acquisition and processing modules of these medical devices are specially designed for soft tissue imaging, and therefore are not suitable for bone imaging due to their significant acoustic contrast with surrounding soft tissue. Besides, the access to raw data is not usually permitted by the manufacturer. Therefore, using a device where various features such as acquisition, signal processing, and raw data can be accessed and manipulated is beneficial to the development of future clinical applications.

Ultrasonic NDT instruments have been developed and used in industrial applications to detect cracks, voids, porosity, and other internal discontinuities in

metals and to analyze material properties since 1940. A new portable ultrasonic phased array instrument - TomoScan FOCUS LT NDT (Olympus Corp., Canada) was commercially developed to provide outstanding performance for both conventional UT and ultrasound phased array and we intend to apply it to study vertebral imaging (refer to Chapter 3). In this Appendix, we aim to evaluate its performances and limitations.

C.1 the TomoScan Phased Array System

Figure C-1 illustrates the device and a transducer array. A computer is connected to the equipment through an Ethernet port connection. The Tomoview software (version 2.9R1) was preinstalled on the computer and used to configure the probe parameters (e.g. aperture size, scanning patterns, focal length and etc).

There are two major computer-controlled beam scanning patterns: linear and sectorial scanning. The linear scanning is accomplished by firing a group of active elements with a specific focal depth and then moving to the next group electronically (Figure C-2a). The sectorial scanning (also called angular scanning) is performed by sweeping the beam through an angular range at a specific focal depth (Figure C-2b).

This PC-based software is also able to acquire and visualize ultrasonic signals from the ultrasound unit. A variety of real-time graphical views are provided: A-scan, B-scan (side view), C-scan (top view), D-scan (end view), and S scan. An A-scan provides raw waveform data showing the time and amplitude, similar to waveforms provided by conventional single-element ultrasonic probe. B, C, D and

S scans are color-coded images (5-bit maximum) from successive A-scans projected on different planes defined by the three axes (ultrasonic, scan, and index), as shown in Figure C-3. An S-scan represents a 2D cross-sectional view as a function of the time delay and refracted angle. The horizontal axis corresponds to the index axis and the vertical axis to ultrasonic depth. Furthermore, the software allows real-time signal averaging and various choices of filters to improve the signal-noise-ratio (SNR).

(a)   (b)
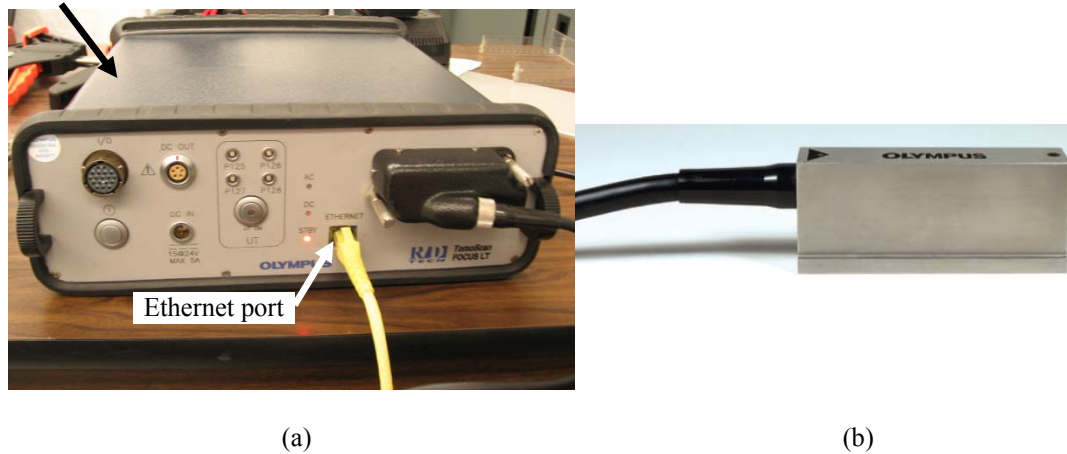
Figure C-1: The TomoScan equipment and the 5.0 MHz linear phased array transducer. A computer is used to connect with the equipment through the Ethernet port to control the beam generation and formation.

C.2 Performance Assessment

The performance test can help gain a better understanding of the performance and limitation of the ultrasound equipment. The tests are commonly performed on image uniformity, sensitivity, focal zone, vertical and horizontal distances, axial and lateral resolution, gray scale/dynamic range, and dead zone.

(a)
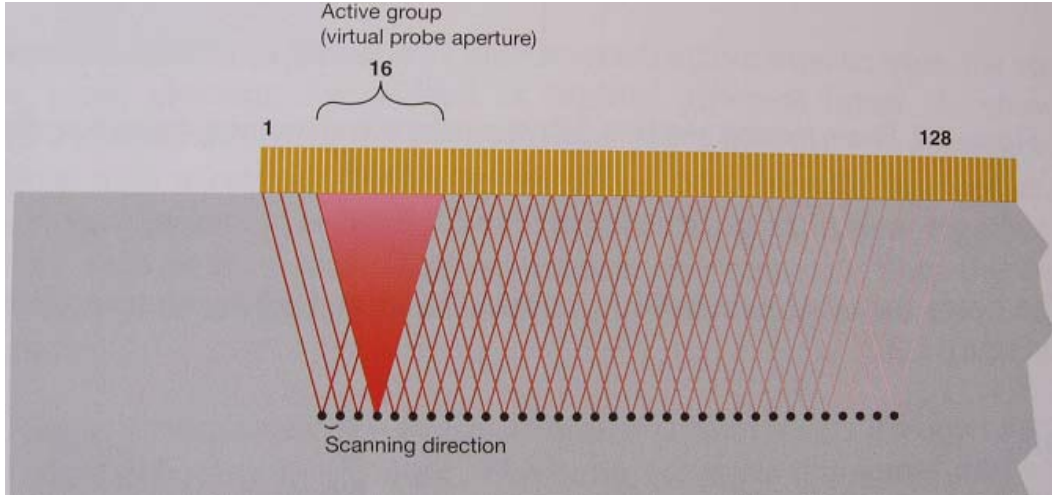
(b)
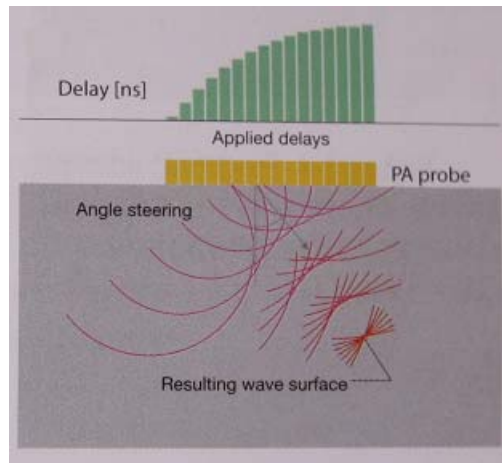
Figure C-2: Illustration of scanning modes. (a) The linear electronic scanning with normal beam and (b) sectorial scanning patterns (Olympus NDT, 2004).
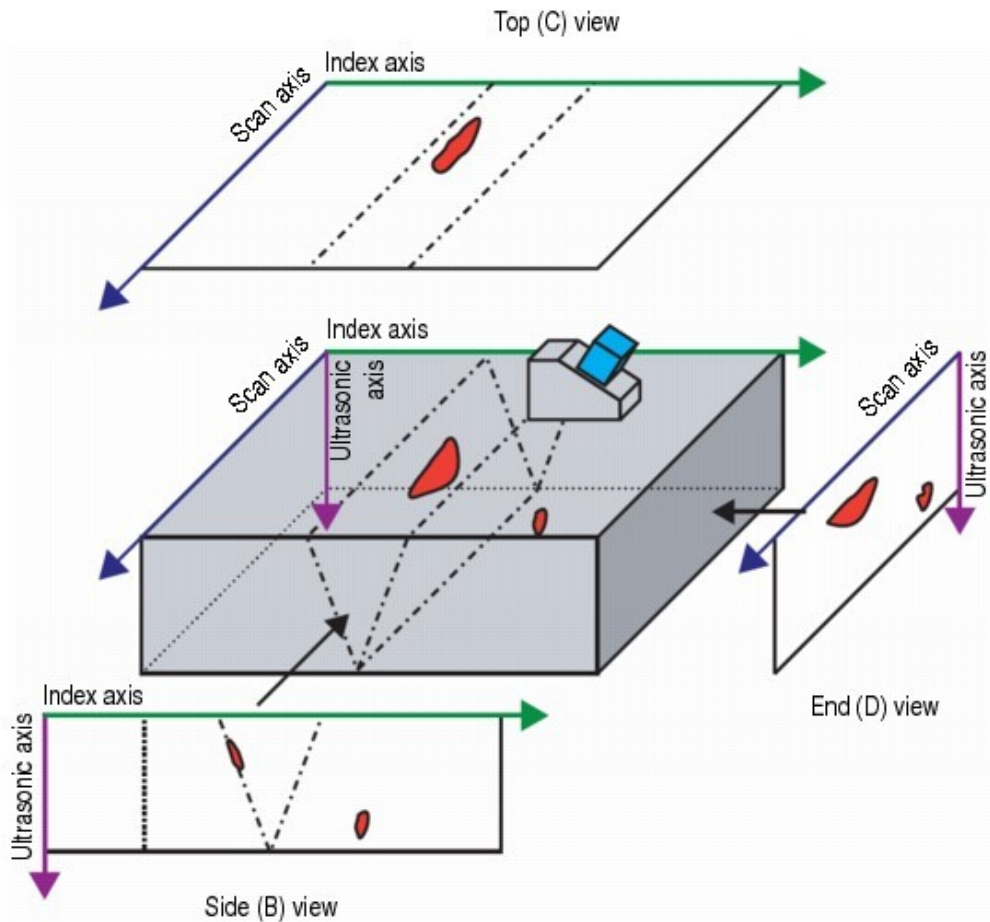
Figure C-3: Demonstration of the ultrasonic views (C, B, and D) (Olympus NDT, 2004).

C.2.1 Image Uniformity

An ultrasound imaging system can produce various non-uniformities, including observable shades within homogeneous tissue texture, and distorted geometric shape. These image artifacts can be due to system hardware malfunction, image processing software bugs, and reverberations from poor acoustic coupling between the interface of transducer and test object (Goodsitt *et al.*, 1998). As a result of these image non-uniformities, the risk of false diagnosis can be increased. Therefore, image uniformity test on an ultrasound system is recommended to be

127

performed periodically so that the defects of a potential large problem can be corrected immediately.

C.2.2 Sensitivity

The sensitivity of an ultrasound system is referred to as the depth of penetration/visualization and it determines the weakest echo level that can be identified and clearly displayed by the system. Notwithstanding, the maximum depth is constrained by the transducer frequency, output power, gain, focal length, number of scan lines and electric noise.

C.2.3 Focal Zone

The focal zone is the region having the strongest intensity and best lateral resolution. The length of the focal zone is indicative of the beam width. For a variable focused transducer, the test should be performed with several different focal zone settings. The focal zone can be affected by the malfunction of the transducer.

C.2.4 Vertical and Horizontal Distance

The vertical and horizontal distance measurements determine the accuracy of distances along and perpendicular to the axis of the ultrasound beam. The vertical distance error always reflects a failure of the system's timing circuits and the horizontal error can arise from flaws of transducer scan modes. The vertical measurement error is usually less than 1.5 mm or 1.5% of the actual distance and

the horizontal error smaller than 2 mm or 2% of actual distance (Goodsitt *et al.*, 1998).

C.2.5 Axial and Lateral Resolution

Axial resolution indicates the ultrasound system's ability to detect closely-spaced objects along the beam axis, while lateral resolution describes the ability to display the objects perpendicular to the beam axis. As Goodsitt *et al.*(1998) reported, it is generally suggested that the axial resolution should be 1 mm or less for transducers with center frequencies greater than 4 MHz and 2 mm or less for transducers with center frequencies less than 4 MHz, depending on the pulse duration of the transducer which in turn depends on the transducer's center frequency. For targets located within 100 mm in depth, the lateral resolution for frequency $\geq$ 5 MHz is normally less than 1.5 mm and is highly dependent upon the machine settings (beam width, focusing, and number of scan lines). To acquire better axial resolution, it is generally recommended to use a higher frequency as well as a shorter pulse length.

C.2.6 Gray Scale/Dynamic Range

Gray scale/dynamic range (DR) refers to a range from a noticeable echo (lowest gray scale level) to the maximum echo brightness. The DR demonstrates the range of echo amplitudes to be displayed in the US image.

C.2.7 Dead Zone

Dead zone is the distance from the front face of the transducer to the first identifiable echo. No useful data are collected within this region. The existence of the dead zone is due to the ringing and reverberations of the transducer from the interface with the phantom. The suggested dead zone for frequencies ranging from 3 to 7 MHz should be less than 5 mm (Goodsitt *et al.*, 1998).

C.3   Test Object

A tissue-mimicking phantom (Model 549, ATS Labs Inc., Bridgeport, CT, USA) made of urethane rubber-based material was used in this study. Figure C-4 shows a photo of this phantom. According to the information provided by the manufacturer, the rubber material has a sound velocity (SOS) of 1450 m/s at 0.5 dB/cm/MHz measured at room temperature which is 6% lower than the normal human soft tissue (1540 m/s). In order to assure the accuracy of measurements, the manufacturer has physically adapted the positions of main objects inside the phantom to compensate for the differences. This phantom is designed to accommodate four ultrasonic scanning surfaces. It consists of a combination of monofilament nylon line targets and cylindrical objects of varying sizes with different contrasts with respect to the base material. Figure C-5 illustrates a diagram of the phantom showing the four scanning surfaces with various embedded targets. The nylon line objects are imaged to evaluate the sensitivity, distance accuracy, resolution, focal zone, and dead zone. The group of targets for the vertical measurement has an interval spacing of 5 mm between the depth of 10 mm and 60 mm, and 10 mm between 60 mm and 300 mm. The group of targets for the horizontal measurement (the nylon lines) has a constant spacing of 10 mm.

For the axial-lateral resolution group, the line targets are spaced at 0.5, 1, 2, 3, 4 mm intervals both axially and laterally. The group of dead zone is composed of 9 line targets. The first target is located 2 mm below the scanning surface #1 and the subsequent targets are spaced 1 mm apart to a depth of 10 mm. The horizontal distance between the 9 targets is 5 mm. One hundred and twenty cystic-like anechoic target structures of assorted diameters (2, 3, 4, 6, 8 mm) are positioned in-line vertically for image uniformity and sensitivity tests. Six gray-scale targets are provided to evaluate the dynamic range with contrast relative to the background material of +15, +6, +3, -3, -6, -15 dB.
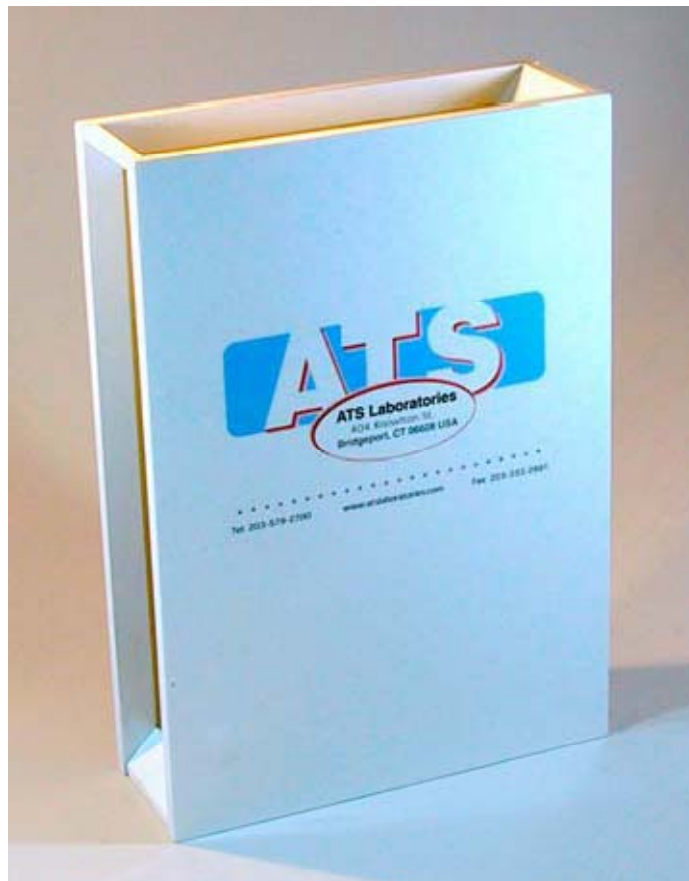
Figure C-4: A photo of the tissue-mimicking phantom model 549.
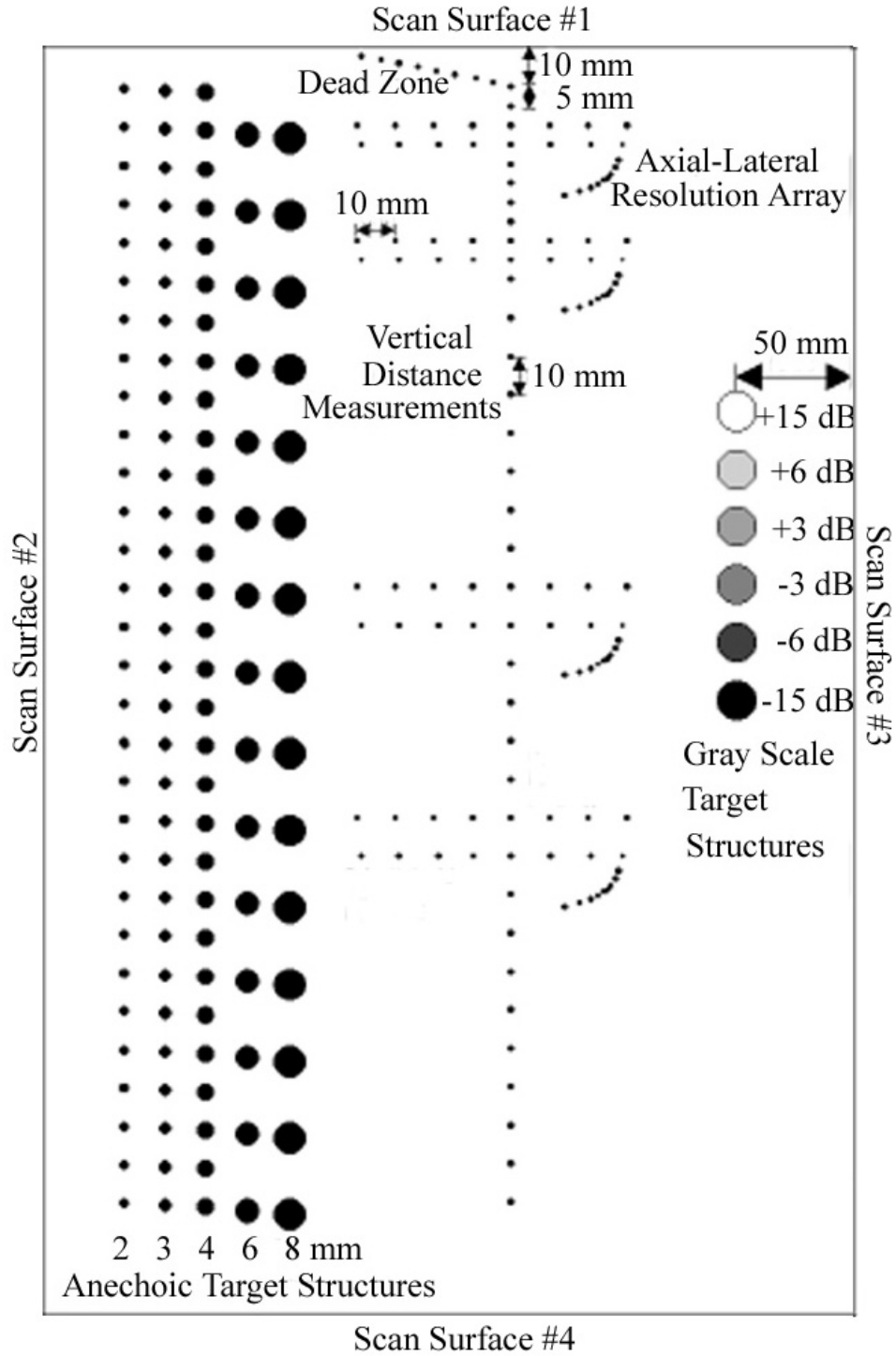
Figure C-5: The diagram of the tissue-mimicking phantom model 549 showing the four scanning surfaces with various embedded targets.

C.4 Equipment Set-Up

A 5.0 MHz 64-element transducer array (5L64-I1) was attached to the TomoScan system. The Tomoview software was preinstalled on a desktop workstation with an Intel Pentium Quad 2.4 GHz CPU, 2 GB RAM, and 32-bit Microsoft Windows XP Professional Service Pack 3 to control the beam generation and formation. A linear scan was accomplished by moving an active group of 16 elements electronically. The scanning surface #1 was used to test the image uniformity, sensitivity, dead zone, vertical and horizontal distance, axial and lateral resolution, and focal zone, and the scanning surface #3 for dynamic range testing. Before the test, the scanning well was filled with water to ensure a good coupling of the transducer with the phantom surface. The transducer was then positioned over the targets on the phantom. A standard weight of 200 g was put over the transducer to fix its position. The data was acquired and all the digitized waveforms were continuously averaged 16 times and passed through a low-pass filter (7.0 MHz) and a high-pass filter (2.25 MHz).

To evaluate the performance and investigate the limitations of the system, nine settings were applied to all the targets (please refer to Table C-1). The choices of the focal lengths in setting 1 to 6 and 9 were determined based on the target positions; the focal settings in 7 and 8 were used to test the limitations of focal length of the instrument. A dynamic depth focusing (DDF) technique was applied to the receiving focus. The maximum range of the received focus allowed by the current software is 20 mm. The allowed maximum soft gain and pulse

133

voltage are 74 dB and 115 V, respectively. Minor modifications (gain, pulse voltage, and pulse width) were then made to acquire desired ultrasound images. Once a clear image was obtained, the image was captured and exported for further examination. Quantitative distance measurements were calculated using the electronic calipers provided by the software.

Table C-1: The nine major instrument settings.

Setting	Emission Focus (mm)	Receive Focus (mm)	Soft Gain (dB)	Pulse Voltage (V)	Pulse Width (ns)
#1	50	40-60	74	115	100
#2	40	30-50	74	115	100
#3	60	50-70	74	115	100
#4	20	10- 30	74	115	100
#5	20	10- 30	74	115	30
#6	20	10- 30	74	40	30
#7	50	80-100	74	115	100
#8	80	80-100	74	115	100
#9	5	2-10	35	115	30

C.5   Results

C.5.1   Image Uniformity and Sensitivity

To examine the uniformity and sensitivity, the first 4 settings with the maximum output levels were initially used. Figure C-6 and C-7 show the images. The left panel indicates the small targets of size 2, 3 and 4 mm and the right panel shows

the large targets of 6 and 8 mm. The small targets (2, 3, and 4 mm) in the near distance (≤20 mm) can't be seen and bright artifacts are observed at the top and bottom of the large targets (6 and 8 mm) because they are out of focus. The targets within the focal length have a well defined circular shape (as delineated by arrows in figures). There are no observable shades of gray within these targets. Figure C-7 (b) shows the ultrasound images using the settings #4 with a receive focus of 10-30 mm. The first small targets can be seen with bright artifacts around them and the first large target is identified with a circular shape without geometric distortions. However, the deeper targets were out of focus in this case. Figure C-8 (a) and (b) show the images after adjusting the pulse width and lowering down the voltage respectively. The images of the near targets are greatly improved with clear edges. Figure C-9 (a) is the image using setting #7 with a focal length of 80-100 mm. Compared with Figure C-6 (a), the shapes of the targets near the emission focus (50 mm) is slightly deteriorated and there is no observable improvement of the images within adjusted receiving focus length (80-100 mm). To be consistent with the receiving focus, the emission length was then adjusted from 50 mm to 80 mm and the generated target image is displayed in Figure C-9 (b). Consequently, the shapes of targets located around 50 mm are further degraded and there is no improvement on the far-distance targets. The target located at the focal zone has a barely satisfactory shape and intensity.

Quantitative measurements of target sizes and sensitivity were made using Figure C-6 (a). The target located at the focal point was used, as indicated by the arrow. The choices of the edge positions for the target are very subjective. In

order to get a reliable data, three measurements were conducted using the electronic caliper over 3 consecutive days (1 measurement/per day). The sensitivity was determined by measuring the bottom position of the last target at 8 mm. Table C-2 presents the descriptive statistics of these measurements.

C.5.2   Vertical and Horizontal Distance, and Focal zone

Vertical and horizontal groups of the targets within the phantom were scanned and imaged for the distance and focal zone measurement respectively. The transducer was aligned parallel along the filaments to avoid distortion.

Figure C-10 presents the images of the line targets using setting #1. Different pulse width, voltage and gain were applied in order to obtain desirable images (Figure C-10 b-d). Setting #1 has an output power set at the highest level. As a result, normal bright artifacts are observed at the top (Figure C-10a) and thus will affect the distance measurement. Reducing the pulse width helps decrease the appearance of bright artifacts (Figure C-10b). A desirable image was generated with reasonable intensity and fewer artifacts by reducing the pulse width and voltage, as shown in Figure C-10 (c). Figure C-10 (d) has a low contrast of the targets with background material. Therefore, the settings of the pulse width and voltage used to produce Figure C-10 (c) were applied to modify the settings of #1, #2, #3, #4 and #8, as shown in Figure C-11 and Figure C-12. In Figure C-11 (a), a smooth line was drawn connecting the ends of echoes from the line targets of both sides to illustrate the shape. The narrowest region is the focal zone. Several arrows were placed individually in Figure C-11 as indicators of the focal zones.

136
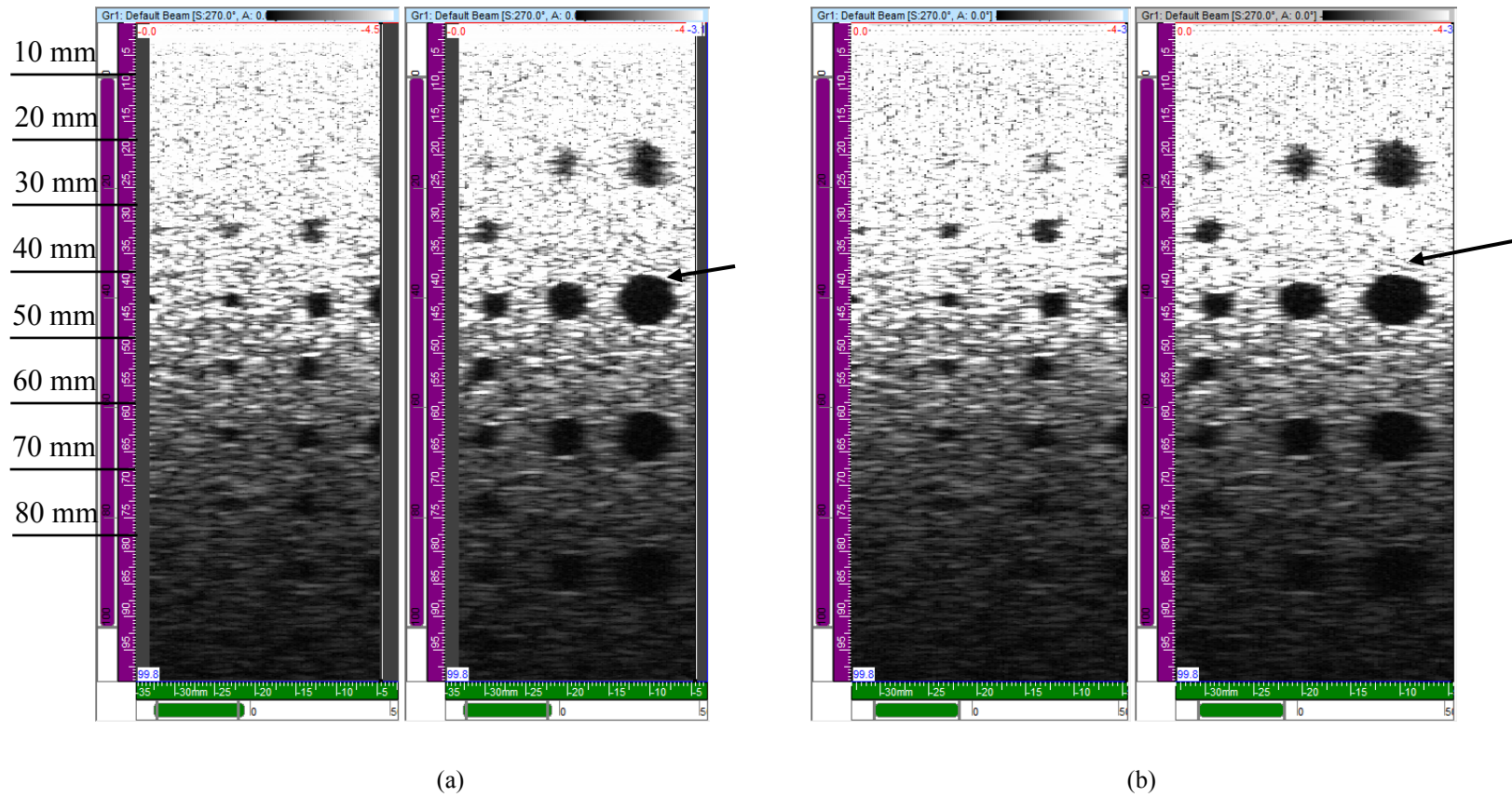
Figure C-6: Image uniformity and sensitivity tests by imaging the anechoic targets of various sizes for (a) setting #1 and (b) #2. The left panels of (a) and (b) indicate the small targets; the right panels are for the large targets. The arrows indicate the targets with the best-defined circular shape.

(a)   (b)
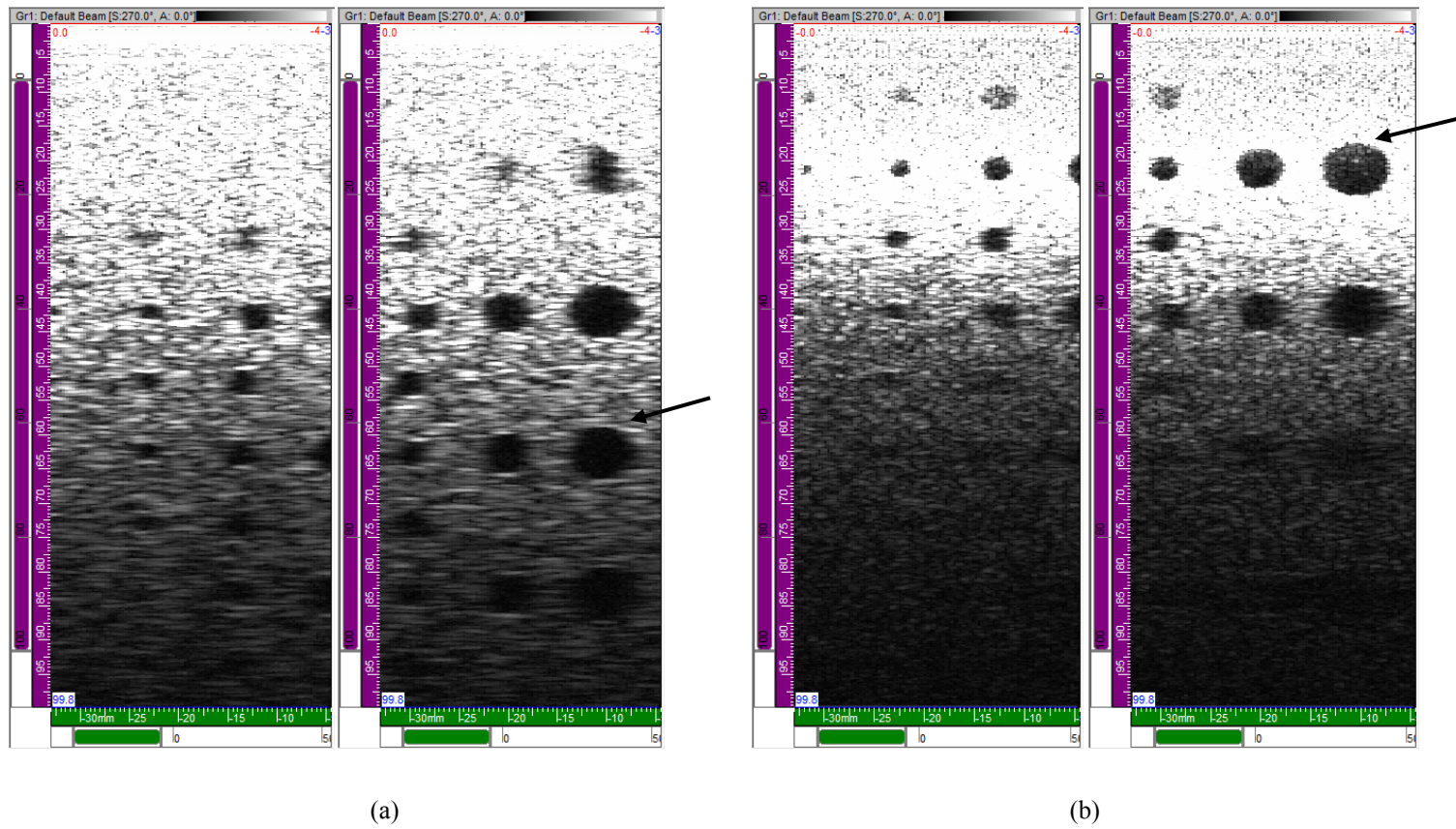
Figure C-7: Image uniformity and sensitivity tests by imaging the anechoic targets of various sizes for (a) setting #3 and (b) setting #4. The left panels of (a) and (b) indicate the small targets; the right panels are for the large targets. The arrows indicate the targets with the best-defined circular shape.
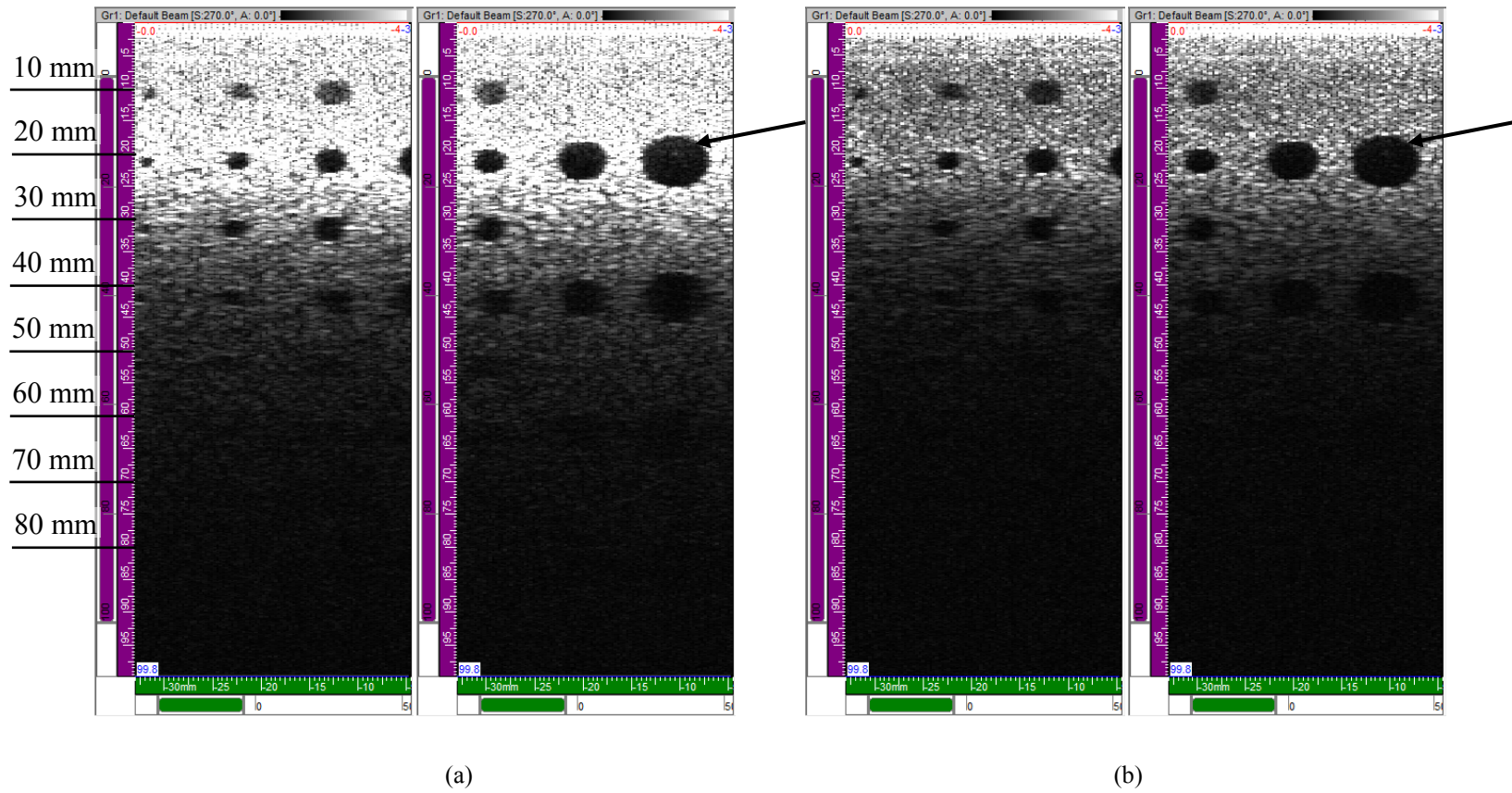
Figure C-8: Image uniformity and sensitivity tests by imaging the anechoic targets of various sizes for (a) setting #5 and (b) setting #6. The left panels of (a) and (b) indicate the small targets; the right panels are for the large targets. The arrows indicate the targets with the best-defined circular shape.

(a)   (b)
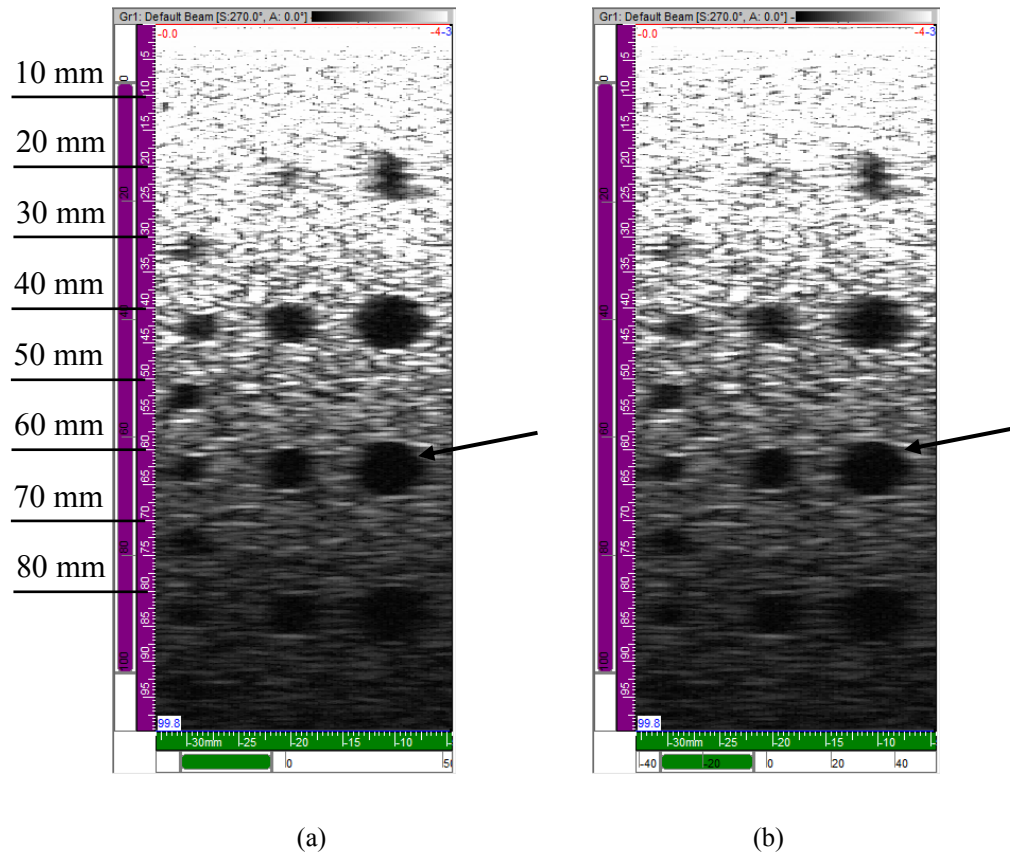
Figure C-9: Image uniformity and sensitivity tests by imaging the 6- and 8-mm anechoic targets for (a) setting #7 and (b) setting #8. The arrows indicate the targets with the best-defined circular shape.

Table C-2: Test performed on the image uniformity and sensitivity.

	Anechoic Target Groups	Number of Displayed Targets	Height/Width (mm)	Shades within Target	Target Edges
	2 mm	5	2.3±0.2/2.1±0.2	No	Distorted
Image Uniformity	3 mm	5	3.9±0.2/2.9±0.4	No	Mild distorted
	4 mm	7	4.0±0.2/3.1±0.5	No	Mild distorted
	6 mm	4	6.2±0.2/4.8±0.3	No	Mild clear
	8 mm	4	8.2±0.3/7.2±0.2	No	Clear

	Anechoic Target Groups (mm)	Actual Depth (mm)	Measured Depth (mm)
Sensitivity	8	88	87.5±0.0

The position of the narrowest region is affected by the focal law setting of the transducer. Except for the setting #8 (Figure C-12), the locations of the focal zones follow the rules of the focal settings. Figure C-13 displays the horizontal tests and Figure C-13 (d) produces the most desirable images for the horizontal targets.

The vertical distance and focal zone measurements were made for all the visible line targets (along the vertical direction) in Figure C-11 (a), and the horizontal distances were measured on Figure C-13 (d). The vertical interval spacing distances were assessed from center to center of the displayed 13 line targets and the horizontal spacing of the displayed 6 targets were also measured. The width of the beam and depth of the focal point were measured 3 times. The statistical values were recorded in Table C-3. The maximum errors among the measured vertical/horizontal distances and their corresponding known distances are under the tolerance of 1.5 mm and 2 mm, respectively.

C.5.3 Axial and Lateral Resolution

The transducer was positioned over the axial and lateral target group using various settings and the generated images are displayed in Figure C-14, C-15 and C-16, respectively. Figure C-14 presents the axial and lateral images using different pulse width and voltages in setting #1. For the same reasons demonstrated in section C.5.2, a smaller pulse width (30 ns) and voltage (40 V) produced desirable images (Figure C-14d) and thus were applied to the remaining
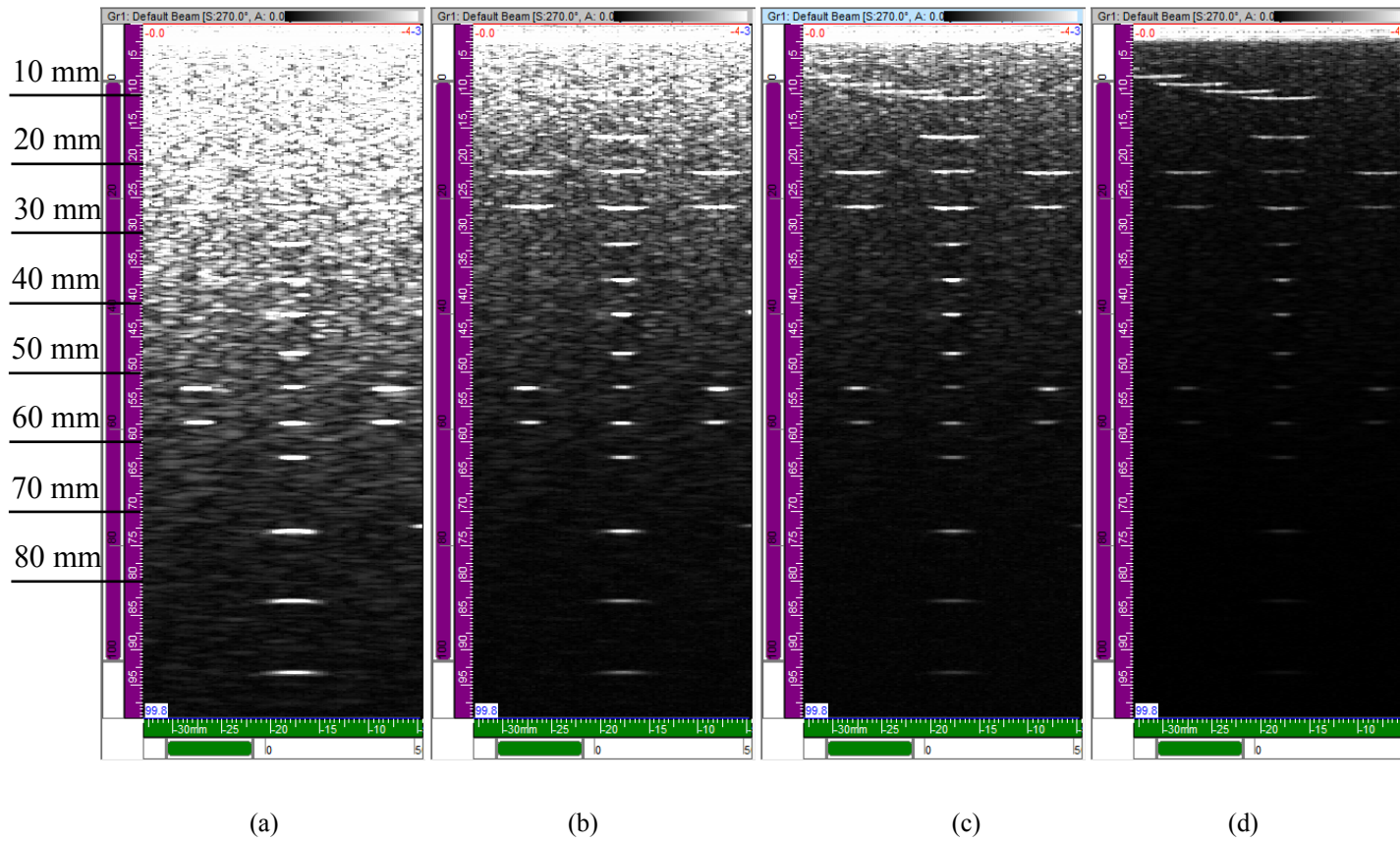
Figure C-10: Focal zone and vertical distance tests by imaging the group of targets along the vertical direction under setting #1 (a) no changes, (b) the pulse width was modified to 30 ns, (c) the pulse width and voltage were changed to 30 ns and 40 V respectively, and (d) a smaller gain 60 dB was applied on (c).

10 mm
20 mm
30 mm
40 mm
50 mm
60 mm
70 mm
80 mm

(a) Setting #1   (b) Setting #2   (c) Setting #3   (d) Setting #4
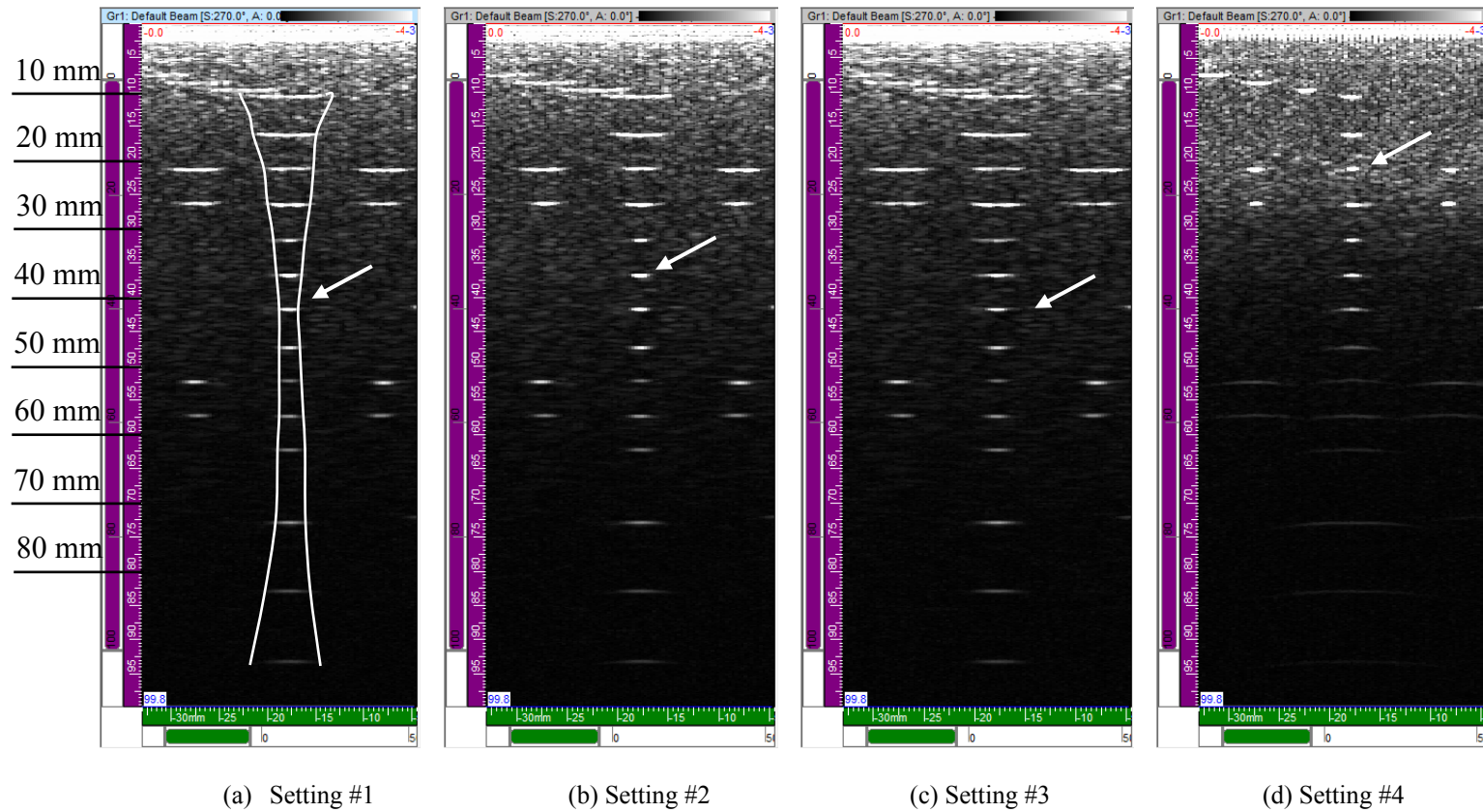
Figure C-11: Focal zone and vertical distance tests by imaging the group of line targets along the vertical direction under settings 1–4 while the pulse width and voltage were changed to 30 ns and 40 V respectively. The arrow indicates the focal point.
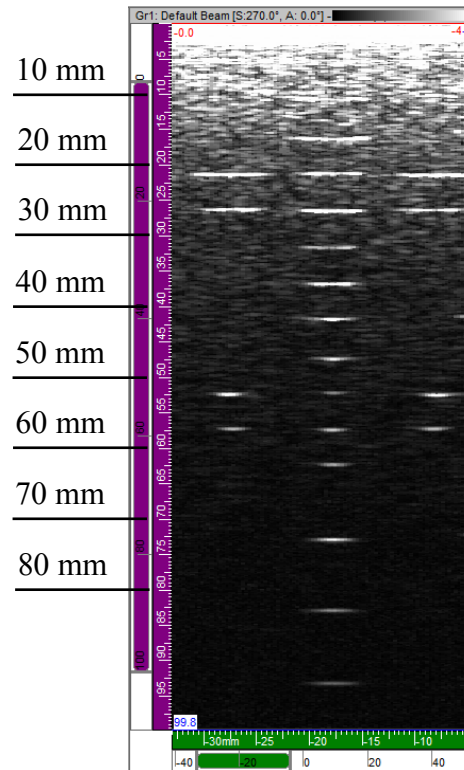
Figure C-12: Focal zone and vertical distance tests by imaging the group of line targets along the vertical direction under setting #8 while the pulse width and voltage were changed to 30 ns and 40 V respectively. The arrow indicates the focal point.

5 mm

10 mm

(a) Setting #1   (b) Setting #2   (c) Setting #3   (d) Setting #4
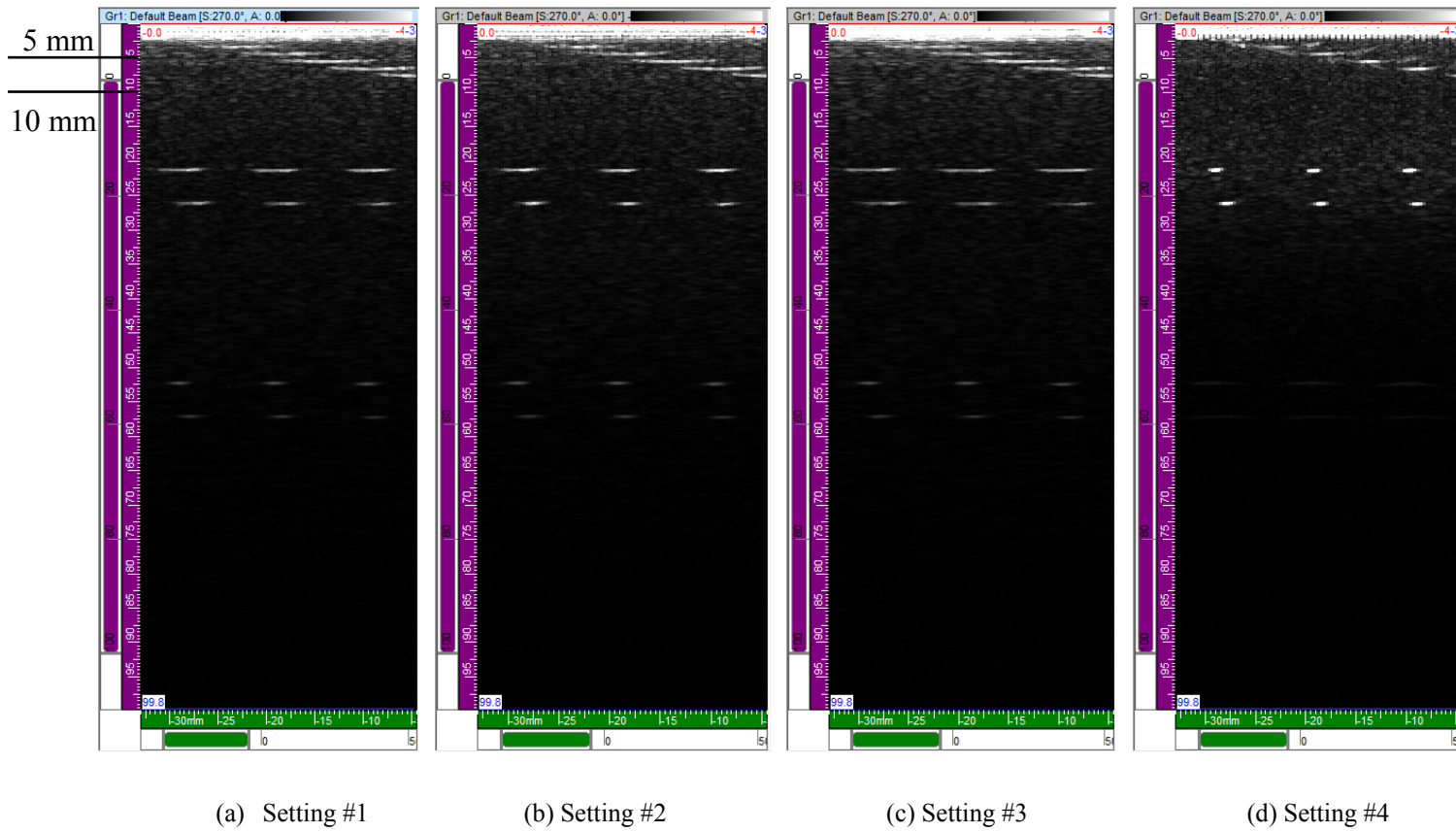
Figure C-13: Horizontal tests of line targets under settings #1-#4: the gain and pulse voltage were changed to 60 dB and 40 V, respectively.

Table C-3: Test performed on the measurements of vertical and horizontal distance, and focal zone.

	Actual Depth Range (mm)	Number of Displayed Targets	Actual Interval Spacing (mm)	Measured Depth of Each Displayed Target* (mm)	Mean ± Std
Vertical Measurement	10-60	11	5	10.8, 16.4, 21.2, 26.6, 31.7, 36.8, 41.8, 47.4, 52.4, 57.5, 62.3	5.2±0.3
	60-300	3	10	73, 83.1, 93.2	10.1±0.0
Horizontal Measurement	20	3	10	29,19.2, 9.6	9.7±0.1
	25	3	10	27.8,18.4, 8.9	9.5±0.1

*For horizontal measurement, the depth values are negative but the absolute values are shown.

	Measured Depth (mm)	Measured Width (mm)
Focal zone	41.8±0.1	2.3±0.3

major settings to produce the images, as shown in Figure C-15. These settings have different focal zones which were chosen at the depth of the axial-lateral group of targets. As Figure C-15 and C-16 displays, the system is able to resolve both the axial and lateral array group at the given depth and the line targets located within the focal zone settings have the narrowest length. The separations (center to center) between two closely spaced objects of the top axial and lateral target group were measured. The center positions of each ligament were measured following the direction shown in Figure C-17. Three measurements were made on Figure C-15 (b) and the statistical values were tabulated together with the actual spacing in Table C-4. The axial resolution is about 0.7 mm satisfying the requirements for transducers of frequency over 4 MHz. The lateral resolution is about 1 mm which is slightly larger than the axial direction but less than the criteria of 1.5 mm.

C.5.4   Gray Scale/Dynamic Range

The transducer was placed on the surface #3 over the gray scale target group. Figure C-18 displays the desirable gray scale images using setting #1. When the absolute value of gray level is greater than 3 dB, the targets are clearly observed with circular shapes and edges. However, the targets with gray scale of +3 and -3 dB fail to be clearly distinguished and have obscure structures. The edges of the observable targets were measured three times, and the corresponding dimensions were calculated and shown in Table C-5.

(a)   (b)   (c)   (d)
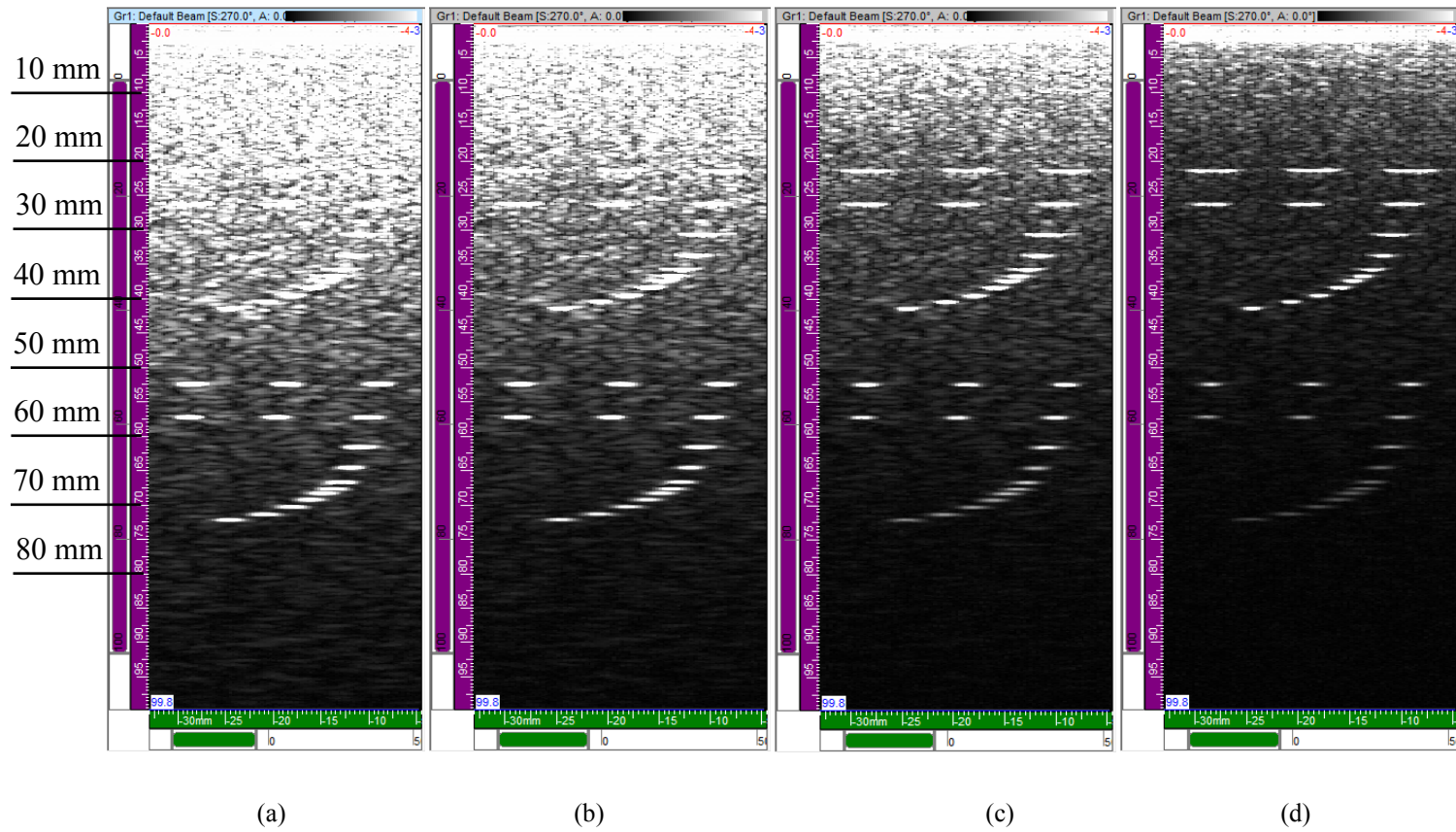
Figure C-14: Axial and lateral resolution tests by imaging the group of axial line targets under setting #1 (a) no changes, (b) the pulse width was modified to 50 ns, (c) the pulse width was changed to 30 ns, (d) a smaller pulse voltage 40 V was applied on (c).

(a) Setting #1 (b) Setting #2 (c) Setting #3 (d) Setting #4
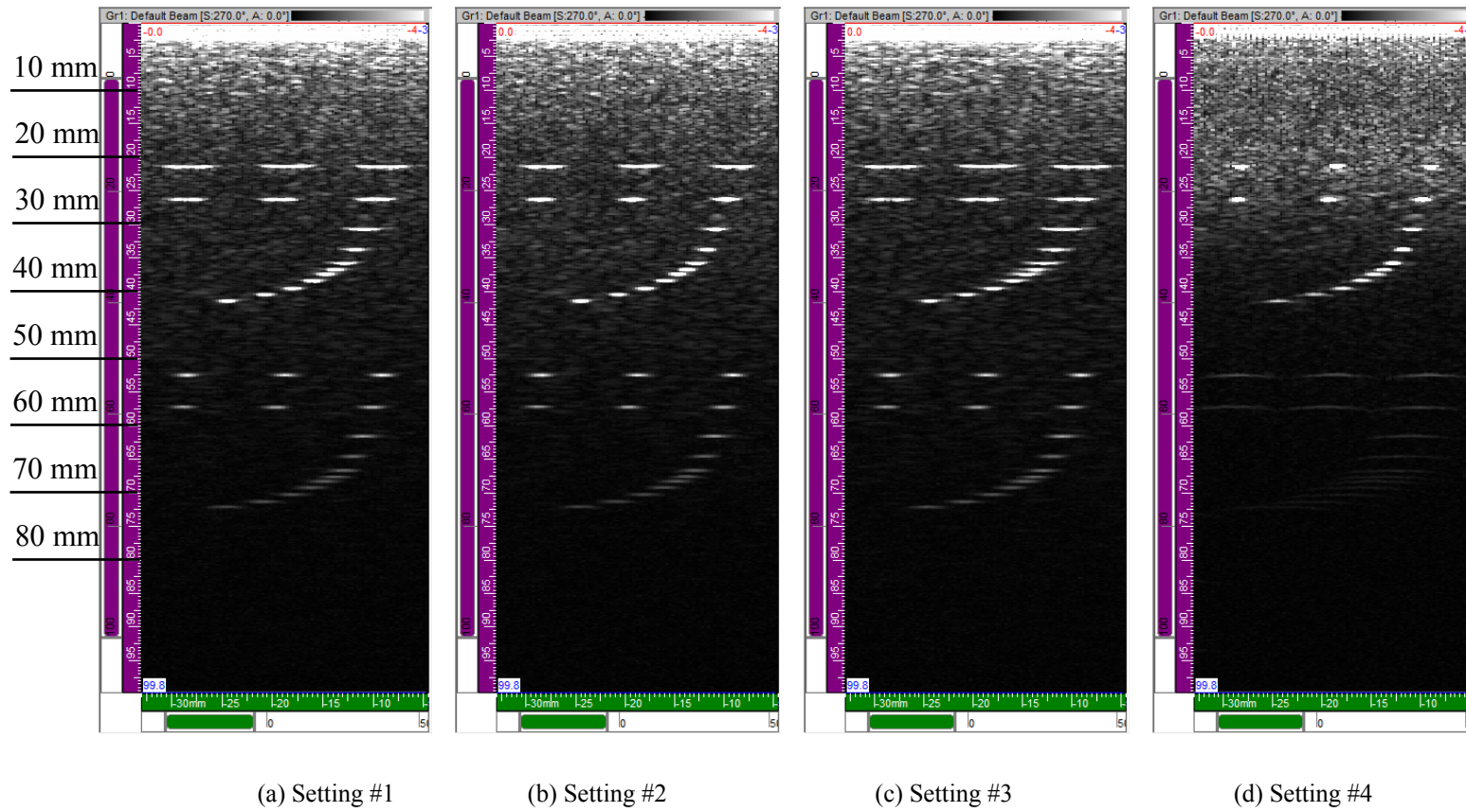
Figure C-15: Axial and lateral resolution tests by imaging the group of axial line targets under settings #1-#4 while the pulse width and voltage were changed to 30 ns and 40 V respectively.
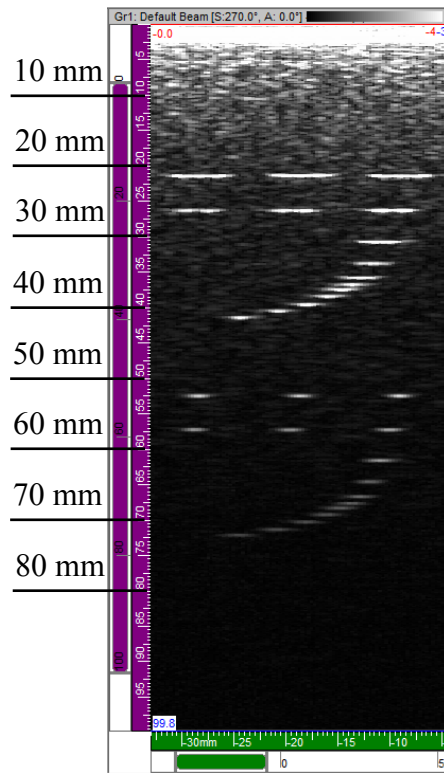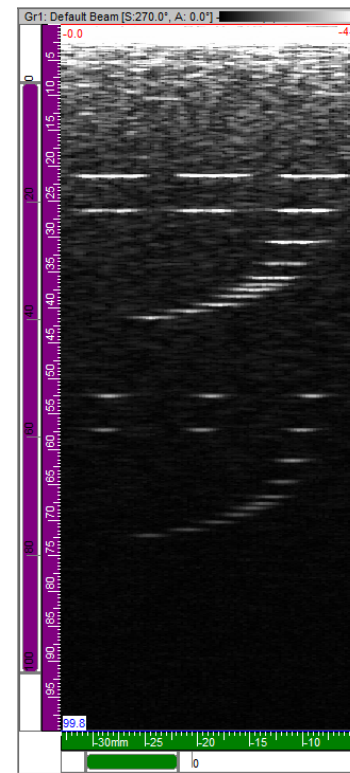
(a) Setting #7   (b) Setting #8

Figure C-16: Axial and lateral resolution tests by imaging the group of axial line targets under setting #7 & #8 while the pulse width and voltage were changed to 30 ns and 40 V respectively.

<div align="center">(a)   (b)</div>
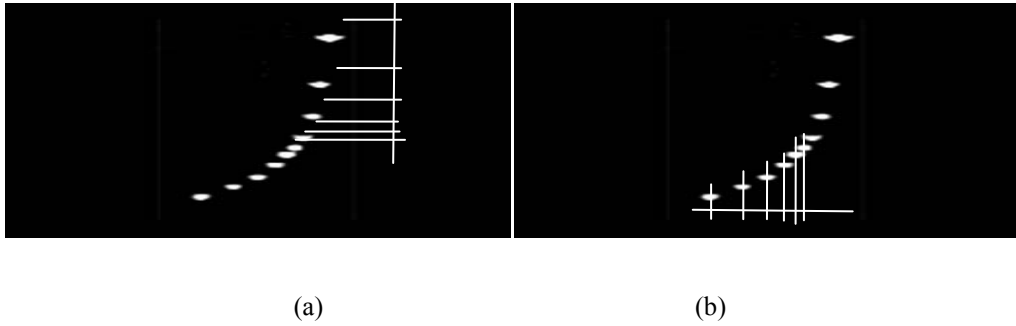
Figure C-17: Illustration of resolution measurement: (a) axial resolution array, and (b) lateral resolution array.

Table C-4: Test performed on the measurements of axial and lateral resolution.

	Actual Depth Range (mm)	Number of Displayed Targets	Actual Spacing (mm)	Measured Spacing (mm)
Axial Array Group	25-35.5	6	4	4.5±0.1
			3	3.0±0.1
			2	2.0±0.1
			1	0.9±0.1
			0.5	0.7±0.1
Lateral Array Group	35.5-46	6	0.5	1.0±0.1
			1	1.3±0.1
			2	1.9±0.1
			3	2.8±0.0
			4	3.5±0.1
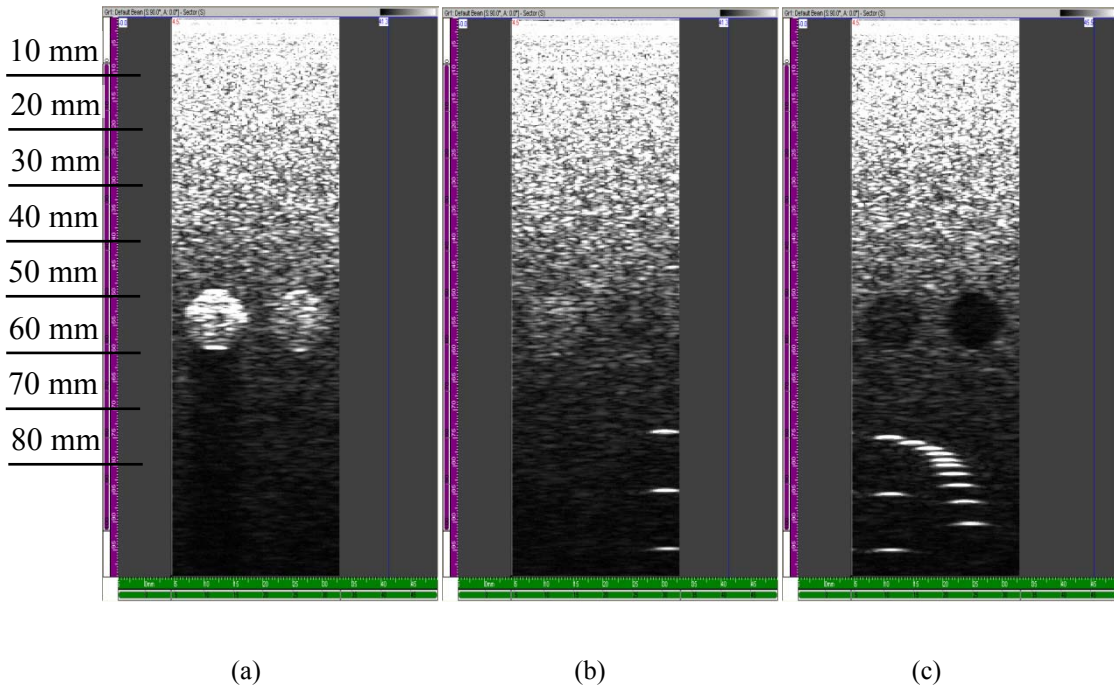
Figure C-18: Gray scale/dynamic range tests by imaging the group of gray scale targets under the setting #1.

Table C-5: Test performed on the measurements of gray scale.

Gray Levels (dB)	Target Edges	Size (mm)	
		Actual	Measured Height/Width
-15	Clear		10.3±0.2/9.5±0.2
-6	Mildly clear		9.8±0.3/9.6±0.5
-3	Obscure	10	NA
3	Obscure		NA
6	Mildly clear		10.9±0.2/10.6±0.1
15	clear		11.1±0.0/11.2±0.6

C.5.5 Dead Zone

The transducer was placed over the group of 9 line targets positioned 2 mm to 10 mm below the phantom surface #1 to test the depth of dead zone. As displayed in Figures C-10 (c) and (d), C-11 and C-13 in the section C.5.2 of vertical and horizontal distance, the nine line targets of dead zone depth can be seen but with wide-spreading lengths since they are located within the parabolic interference range of waves originating from the array elements. Nevertheless, the first line target of 2 mm deep can be identified when setting the focal zone to a comparatively nearer distance of 10-30 mm (Figures C-13d). The dead zone meets the required criteria of less than 5 mm. To acquire an accurate measurement of dead zone, the focal zone was set closest to the depth of these targets, and appropriate gain, pulse width and voltage were applied to image these targets. As Figure C-19 presents, an increase of gain from 35 dB to 50 dB greatly increase the intensity of the echoes while length spreading is observable in the first 5 line targets even after reducing the pulse voltage from 115 V to 40 V. This indicates that the gain more strongly affects the signal intensity enhancement than does pulse voltage. The measurements of center-to-center distances were also performed three times over 3 consecutive days using the caliper and the averaged values are listed in the Table C-6. Nevertheless, the echoes from the background are barely visible. Clear signals from the dead zone were obtained at the sacrifice of losing sensitivity and focal length.

5 mm

10 mm
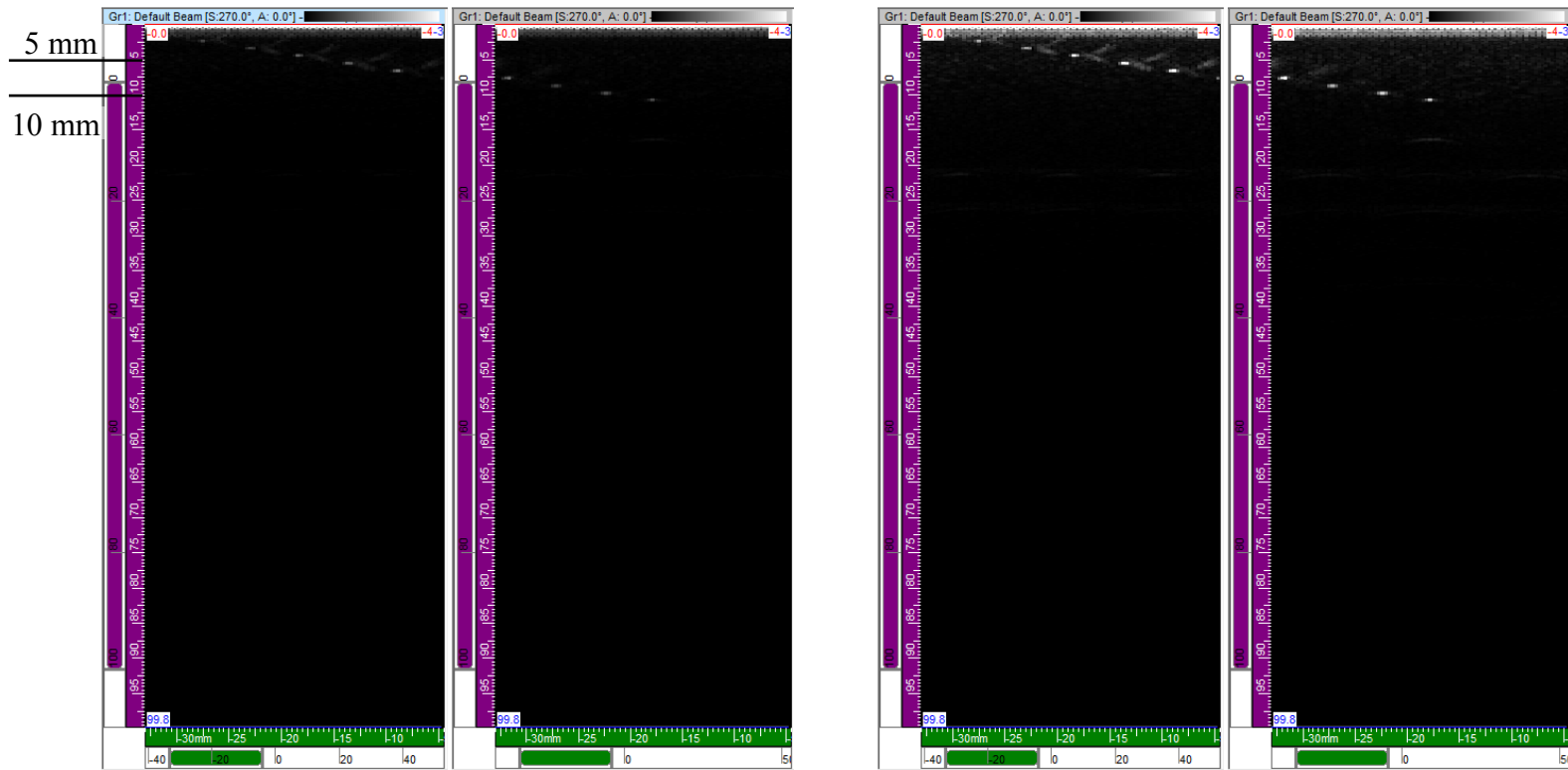
(a)

(b)

Figure C-19: Dead zone tests under setting #9: (a) no changes, (b) the gain and pulse voltage were changed to 50 dB and 40 V, respectively. The left panel of the subfigures indicates the first 5 line targets and the right one shows the last 4 targets.

Table C-6: Test performed on the measurements of dead zone.

Actual Distance (mm)	Measured Distance (mm)	Mean ± Std
2	2.4,2.4,2.3	2.4±0.1
3	3.4,3.3,3.4	3.4±0.1
4	4.4,4.4,4.4	4.4±0.0
5	5.4,5.5,5.5	5.5±0.1
6	6.6,6.6,6.5	6.6±0.1
7	7.7,7.6,7.6	7.6±0.1
8	8.7,8.8,8.7	8.7±0.1
9	9.8,9.7,9.8	9.7±0.1
10	10.8,10.7,10.7	10.7±0.1

C.6 Conclusions

The common quality control parameters of a phase array ultrasound system were tested and recorded in this Appendix. Various settings were applied and adjusted to acquire desirable images. The effects of each parameter were discussed. The focal zone determines the intensity and width of the focal point. However, the system has a limitation for a 5.0 MHz transducer when the emission focal length over 80 mm. The maximum range of DDF setting is restricted to be less than 20 mm. As well, the Tomoview software constructs the cross sectional images with a maximum of 32 colors which affect the resolution of object edges. The gain technique used by the software can only enhance the signal intensity with depth which will in turn decrease the contrast of objects in the near distance, as

discussed in Chapter 3. Adapted gain compensation is strongly recommended. Nevertheless, TomoScan allows the exportation of raw data. Hence, further off-line image processing techniques can be applied to increase the image quality. In summary, the TomoScan with a frequency of 5.0 MHz has a satisfied performance for the targets within 80 mm depth and has great potential in the bone imaging application with right setting.